UNIVERSITY OF OKLAHOMA

GRADUATE COLLEGE

THE INFLUENCE OF URBAN FORM AND VEGETATION ON NEAR-SOURCE

DISPERSION IN A REALISTIC URBAN CANOPY

A THESIS

SUBMITTED TO THE GRADUATE FACULTY

in partial fulfillment of the requirements for the

Degree of

MASTER OF SCIENCE IN METEOROLOGY

By

BRIANA MARIE LYNCH
Norman, Oklahoma
2019

THE INFLUENCE OF URBAN FORM AND VEGETATION ON NEAR-SOURCE
DISPERSION IN A REALISTIC URBAN CANOPY

A THESIS APPROVED FOR THE
SCHOOL OF METEOROLOGY

BY THE COMMITTEE CONSISTING OF

Dr. Scott Salesky, Chair

Dr. Petra Klein

Dr. Bradley Illston

Acknowledgments

Table of Contents

List of Tables

List of Figures

Abstract

The atmospheric boundary layer controls many interactions within the tropo-sphere from larger scale atmospheric features to land-atmospheric interactions. The urban boundary layer is the layer above an urban area that is heavily impacted by what happens below, while the urban canopy layer is impacted by the immediate surroundings within the urban area. Understanding flow within the urban canopy layer is crucial for determining the distribution of particulate matter in urban areas and implications for air quality and human health.

Previous experiments have examined downtown urban domains by releasing tracers to understand dispersion and dissipation of tracer plumes and how turbulence and urban geometry can affect them. Gaussian plume models have been used in the past to model dispersion in urban areas, especially for scalar transport. While multiple studies have been conducted to understand plume characteristics in urban environments, plume behavior close to point sources (< 1 km) and the effects of buildings and foliage on plume characteristics are not well understood.

A field campaign, Tracer Release in an Urban Canopy (TRUC), was conducted in the Sunset Neighborhood of Vancouver, British Columbia in June 2017. This location is well-documented by previous field campaigns. The instrument configuration used during TRUC consisted of fifty spinning impaction traps, a mobile tower with 3-D sonic anemometers at two levels (16.6 m and 1.5 m), and five 2-D sonic anemometers deployed at 1.5 m. A mobile source at 2.4 m released 35 μm yellow/green and violet fluorescent microspheres from 3-D ultrasonic atomizer nozzles. Fourteen successful releases were conducted, each for twenty minutes, at four different locations throughout the neighborhood.

An equation consisting of the Superposition of two Orthogonally-oriented Gaussian plume distributions (SOG) (Miller et al., 2018) was utilized to fit the concentration data collected. The SOG was compared to the TRUC data to determine

suitability for interpolating between collection points. While the SOG did character-
ize the pattern of the concentration behavior well for both the near and far fields, the
magnitude of the concentrations was often misrepresented. Channeling of the plume
was observed during the TRUC campaign, which was characterized by the SOG most
of the time. Comparison of the mean wind angle relative to the street network and
various plume parameters were utilized to visualize the channeling of the plume.

Results from this data and usage of the SOG equation were utilized to de-
termine higher-order plume moment statistics. Turbulence, building, and vegetation
statistics were also calculated to describe the plume characteristics and behaviors.
Evidence of a relationship was seen between the mean wind direction and first order
moment, as well as between the mean wind angle and the second order plume mo-
ment. While turbulence does affect the plume, especially with mean wind direction,
the urban geometry proved to affect the plume characteristics more so in the urban
domain.

Chapter 1

Introduction

1.1 The Atmospheric Boundary Layer

The atmospheric boundary layer is the lowest layer of the troposphere, the first layer of the Earth's atmosphere. A boundary layer, defined initially by Prandtl (1904), is the thin region within a fluid that experiences the frictional effects from the surface. Since the atmosphere is also a fluid, the atmospheric boundary layer (ABL) can also be described. Stull (1988) defines the atmospheric boundary layer as "the part of the troposphere that is directly influenced by the presence of the earth's surface, and responds to surface forcings with a timescale of about an hour or less". The ABL is strongly affected by surface heating and has a clear diurnal cycle (Figure 1.1). While the ABL can vary in space and time depending on the surface heat flux, the daytime convective boundary layer is typically between 1 to 2 kilometers in depth, while the nocturnal stable boundary layer is between 100 to 200 meters (Stull, 2006).

The structure of the ABL is complex and accepted within the community to be similar to a two-dimensional turbulent boundary layer, as they both have two distinct outer and inner regions for neutral conditions (e.g. Monin, 1970; Tennekes, 1973). The outer region is considered to have flow that is nearly independent of the surface and dependent on free-stream velocity. The inner region, also called the Prandtl or surface layer, has flow that is strongly influenced by the surface and its characteristics. The "inertial layer" is the overlap region in between the inner and outer region. Close to the surface is the interfacial sublayer, known also as the roughness, viscous, or canopy sublayer. This layer is considered to have constant wind direction with height, which then neglects the effect of the Earth's rotation on the region. Figure 1.2 (Brutsaert, 1982) shows these several layers of the atmosphere for a neutral ABL. In an unstable
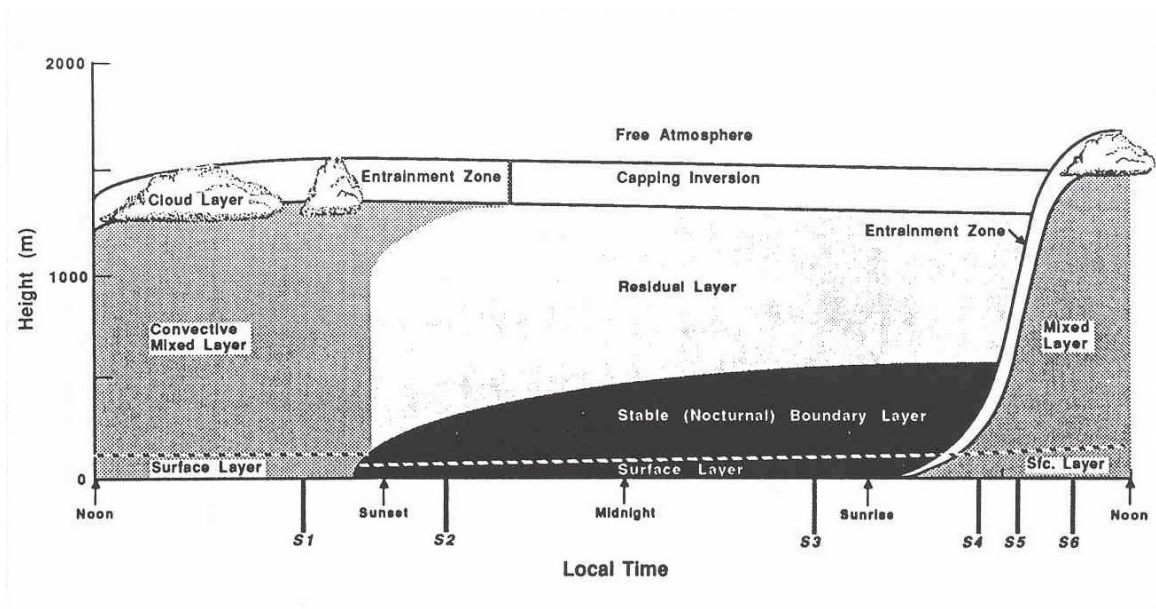
Figure 1.1: Diurnal cycle of the atmospheric boundary layer, figure from Stull (1988)

.

environment, the outer region is also considered to be the convective mixed layer, with a capping inversion, similar to Figure 1.1. For stable conditions, the thickness of the ABL is much smaller than neutral or convective ABLs, which is also evident in Figure 1.1.

It is important to understand how the ABL interacts with the biosphere through land-atmospheric interactions. Sensible and latent heat fluxes can also impact boundary layer development (Rabin et al., 1990), as well as convective initiation (Findell and Eltahir, 2003a; Santanello et al., 2009). Evapotranspiration, a term given for the combined effects of land transpiration from vegetation and evaporation from the soil and other water sources (Brutsaert, 1982), plays a major role in the hydrological cycle. Evapotranspiration from land surfaces heavily controls this cycle, along with precipitation, and can determine how the surrounding atmosphere interacts and behaves (Jacobs and De Bruin, 1992; Dirmeyer et al., 2009). Changes in CO_2 fluxes can also contribute to land-atmosphere interactions through surface temperatures

2
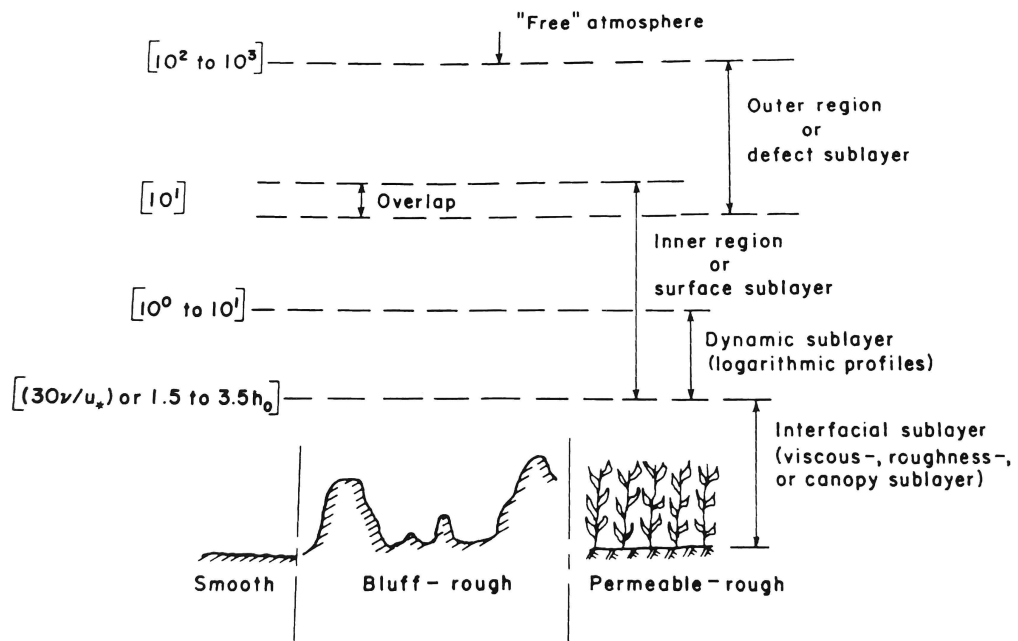
Figure 1.2: Brutsaert (1982) sketch of the vertical structure of the sublayers in the atmospheric boundary layer; h_0 is the roughness obstacle height; The heights of the layers (in meters) are not shown to scale.

(Hansen et al., 1998), ecological and plant functions (Amthor, 1995), and growth seasons (FLUXNET; Baldocchi et al., 2001; Chen et al., 2018).

1.2   The Urban Boundary Layer

Anthropogenic influences can also affect and be affected by atmospheric flows. The development of urban areas has lead to two specific regions of the atmospheric boundary layer that differ from the ABL over a flat, horizontally homogeneous surface: the urban boundary layer (UBL) and the urban canopy layer (UCL). Oke (1976) defines the UCL as "microscale concept, its climate being dominated by the nature of the immediate surroundings". Additionally, he defines the UBL as a "local or mesoscale concept referring to that portion of the planetary boundary layer whose characteristics are affected by the presence of an urban area at its lower boundary" (Figure 1.3).

Urban geometry can interfere with the ABL as flow from beyond the UCL enters the urban area. "Topological dispersion", a term coined by Davidson et al. (1995, 1996), defines the flow where the mean streamlines diverge around obstacles, separating fluid parcels and therefore, dispersing passive scalars. This behavior is important to consider when analyzing flow in the urban boundary layer.

The urban heat island phenomenon (UHI), first documented from meteorological observations in London during the 1810s (Howard, 1833), highlights that urban and metropolitan areas have warmer air temperatures than their surrounding rural environments, due to human activity. This difference in temperature can be by 1-2°C warmer in the daytime and up to 12°C in the nighttime (American Meteorological Society, 2012). This phenomenon has been heavily observed during the 1960's and 1970's (see Oke (1974, 1979b) for technical reviews), throughout the early 2000s (Goldreich, 1992; Tso, 1996; Goh and Chang, 1999; Tereshchenko and Filonov, 2001; Velazquez-Lozada et al., 2006), and in recent years (Peng et al., 2011; Zhao et al.,
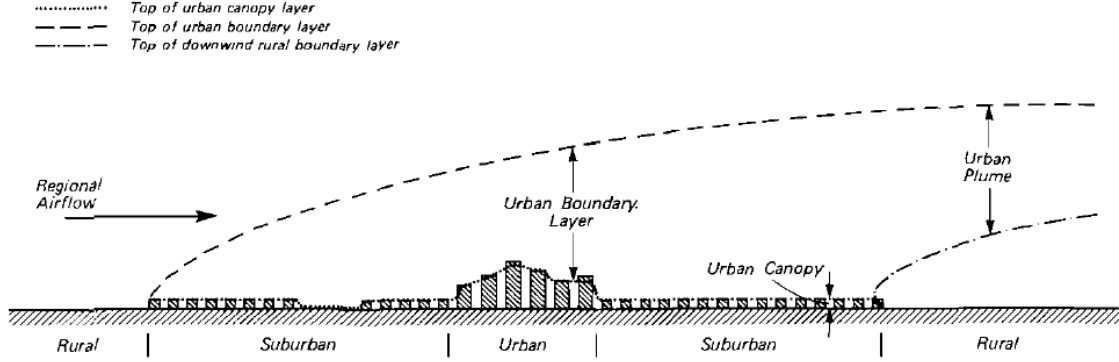
Figure 1.3: Visualization of urban canopy layer (UCL) and urban boundary layer (UBL), compared to the rural surroundings (Oke, 1976)

.

2014; Chakraborty et al., 2017). To explain the phenomenon and potential causes, Oke (1982) proposed a 'surface' energy budget that describes the sources and sinks of heat fluxes at the interface of the UCL and UBL.

$$Q^* + Q_F = Q_E + Q_H + \Delta Q_s \qquad (1.1)$$

where Q^* represents the surface net radiant flux density, Q_F is the anthropogenic heat flux density, Q_E and Q_H represent the latent and sensible heat fluxes, respectively, and ΔQ_s is heat storage, which is empirically determined for varying urban land surfaces.

Proposed causes of the urban heat island effect can be defined by these heat fluxes, as well as for both the UCL and UBL. While Oke (1982) summarized them, Howard (1833) and others have come to similar conclusions from previous studies (e.g. Doll et al., 1985; Anandakumar, 1999; Ichinose et al., 1999; Steinecke, 1999). Potential causes leading to a positive temperature anomaly in the canopy layer include increased long-wave radiation from the sky, decreased long-wave radiation loss, decreased evapotranspiration, increased sensible heat storage, and decreased total turbulent heat transport. For the UBL, causes can be attributed to increased sensible heat input

as entrainment from below and above the layer. Increased absorption of shortwave radiation and anthropogenic heat sources both contribute to warming in the UCL and UBL.

Several features have been identified that can contribute to these energy balance changes. Buildings, traffic, and smoke stack heat losses account for many of the anthropogenic heat sources (e.g. Pigeon et al., 2007; Ma et al., 2017). Street canyon geometry and air pollution affect the increased shortwave radiation absorption (e.g. Givoni, 1989; Steemers et al., 1998). Due to this contribution, air pollution becomes an important and ever-growing problem to address.

Pollution can be found in a variety of shapes and particle sizes, varying by several orders of magnitude. Particulate matter (PM) is a microscopic mixture of solid and liquid matter that can be comprised of both organic and inorganic compounds (Environmental Protection Agency, 2018). While dust and pollen can be constituents of PM, so can harmful pollutants, such as soot and industrial products. PM can range from nanometers to 10 microns. PM_{10} and $PM_{2.5}$, particles that are 10 microns (μm) and 2.5 microns (μm) in diameter, are the particulates that impact human health the most. Exposure to PM_{10} has been shown to lead to increased cardiovascular and respiratory issues (Anderson et al., 2012). Similarly, exposure to $PM_{2.5}$ has been connected to increased cases of cardiovascular, cerebrovascular, and ischemic heart diseases, as well as increased hospitalizations (see Brook et al. (2010) for a comprehensive summary).

According to the 2018 Revision of World Urbanization Prospects, 50% of the world's population lived within urban environments in 2007 (UNDESA, 2018). As of 2018, that percentage has increased to 55%. These urban populations are expected to continue to increase by 2% per year in the next several decades. During 2012, over 7 million premature deaths were attributed to air pollution-related conditions, where

half of these were directly related to outdoor air pollution (World Health Organization, 2016). With growing urban populations, increased urbanization could lead to increasing levels of PM_{10} and $PM_{2.5}$, which could further lead to more human health issues and fatalities. To understand this growth, it is important to understand urban environments, flow characteristics of downtown areas and street networks, and the transport of passive scalars and fine particulate matter in urban canopies.

1.3 Transport Studies in Urban Canopies

One of the earliest urban field campaigns conducted was the Urban Air Pollution Dynamic Research Network in the New York Metropolitan Area (Davidson, 1967). The study focused on pollutant transport and diffusion of SO_2 in a large urban environment across a wide range of spatial and temporal scales. Distinct plumes were observed beneath the lowest temperature inversion throughout the domain, noting that the environmental temperature distribution had an effect on the SO_2 concentrations. Long distance transport of the SO_2 plume was observed across the domain through several street measurements. This experiment paved the way for several other projects in the following years (e.g. Changnon et al., 1971; Schiermeir, 1978; Doran et al., 1998; Menut et al., 2000).

The urban meteorological and tracer (URBAN 2000; Allwine et al., 2002; Clawson et al., 2004) field campaign was one of the first major urban experiments that included multiple areas of the urban environment: individual buildings, a network of buildings, throughout the urban area, and downstream several kilometers from a release location. Conducted throughout October 2000 in Salt Lake City, Utah, the focus of URBAN 2000 was to observe passive tracer behavior in street canyons, rapid vertical mixing, and diurnal thermally-driven flow influence in the nocturnal urban boundary layer. During the Intensive Operating Periods (IOPs), passive tracers, sulfur hexafluoride (SF_6) and perfluorocarbon tracer (PFT), were utilized during multiple releases.

Observations of elevated tracer concentrations at the building tops indicated complete vertical mixing through the urban canopy. Within the downtown domain, the tracer plume was affected by easterly downslope winds from the Wasatch Mountains and southeasterly downvalley winds from the Salt Lake Valley. These observations indicate that the urban geometry and topography can have an effect on passive tracer plumes, which agrees with previous literature (e.g. DePaul and Sheih, 1986; Hoydysh and Dabberdt, 1988; Kastner-Klein et al., 2004).

To determine trends in the urban canopy on a longer temporal scale, the Basel UrBan Boundary Layer Experiment (BUBBLE) was deployed between summer 2001 to summer 2002 in the city of Basel, Switzerland (Rotach et al., 2004, 2005). This long-term experiment used both near-surface observations and remote sensing boundary layer observations to characterize a small urban area. During several IOPs, SF_6 was released at "near-roof level" (1.5 m above roof level) to observe tracer movement and dispersion through urban street canyons. Along with the observational data, laboratory experiments and numerical modelling were included in BUBBLE. Numerical testing included looking at urban surface exchange parameterizations, dispersion modelling, and turbulence structure in the urban roughness sublayer using the Lagrangian Particle Dispersion Model (Rotach et al., 1996).

The resulting plume had higher concentration values observed close to the source and lower values as the plume spread laterally. The interpolated plume was wide in extent, which coincided with variable observed winds, and the crosswind concentration distribution appeared Gaussian in shape. Even with an elevated release and urban geometry, the concentration pattern looked like the source was a near-surface release. One observation taken from inside a street canyon showed an insignificant vertical gradient throughout, demonstrating a well-mixed concentration profile.

Further investigation of the diurnal development in the urban boundary layer led to the collaborative effort in Oklahoma City, Oklahoma (OKC): Joint Urban 2003

(JU03; Clawson et al., 2005; Allwine and Flaherty, 2006a). For this campaign, the focus was to resolve atmospheric dispersion using passive tracers across several spatial scales, from of an individual city block to the blocks in and around the central business district (CBD) to the suburban area of OKC downstream several kilometers. Indoor-outdoor air exchange in several buildings was examined, as well as the human influence on street canyon turbulence. The outdoor experiments released SF_6 in "puffs" or continuous releases near ground level, while the indoor experiments released PFT.

Results from JU03 provided several insights into tracer movement with turbulence and urban geometry. Tracer dissipation occurred more rapidly during the daytime than nighttime at both rooftop and street levels, but concentration dissipation rates did not vary significantly at either location or time of day. Wind speeds at rooftop level did influence dissipation rates at night, but not during the day. This may be due to the presence of steady nocturnal winds and the lack of local convection at the night. Turbulent kinetic energy (TKE) and the standard deviations of along-wind (σ_u) and vertical velocities (σ_w) were greater at the rooftop level than street level. This could have been due to tracer trapping and venting at the street level. Indoor experiments in pedestrian tunnels detected tracer accumulation and dissipation for much longer time scales than those measured outdoors in open air.

Concentrations observed at street level during JU03 exceeded those at roof-top level by a factor of 3 or greater. Roughness elements affected tracer dissipation more so at street level than at rooftop levels. Channeling down street canyons was observed at street level at angles between 60 and 80° from the downwind direction. TKE, σ_u, and σ_v (standard deviation of cross-wind velocity components) were all measured to have 5% statistically significant correlations to the CBD median tracer dissipation coefficients at both the street and roof levels, suggesting that this turbulence may have the capability to predict tracer dissipation throughout the urban canopy.

The New York City Madison Square Garden (MSG05) urban field campaign aimed to expand the understanding of flow and dispersion in urban street canyons by deepening the observation area to very tall buildings in a large urban area (Allwine and Flaherty, 2006b; Hanna et al., 2007; Hanna and Baja, 2009). During the two IOPs in March 2005, the campaign released six different PFT tracers from street level to observe rapid vertical transport and dispersion in recirculating eddies adjacent to the study buildings.

Compared to JU03, the average vertical velocities at the top of the buildings were much larger during MSG05, due to the larger buildings and possibly larger recirculation zones. While quantitative data is not available for MSG05, Allwine and Flaherty (2006b) utilized plume contours and wind data from the experiment to provide initial analysis. The plumes from the five releases during the first IOP show spreading in the southeast direction, with two releases producing a splitting lobe of the highest concentration value to the northeast. This feature is presumed to be due to channeling from a street adjacent to MSG. Two of the other releases show wide plumes spreading in the same direction to the southeast, while the last release plume is very narrow. Higher wind speeds were observed northeast of the MSG building, which could explain the narrow plume shape. IOP2 showed similar channeling for four of the five releases.

For extended observations of an urban boundary layer, the Dispersion of Air Pollution and its Penetration into the Local Environment (DAPPLE) field experiments were conducted in two phases: between 2002 - 2006 and 2006 - 2010 at one particular busy intersection in central London, United Kingdom (Dobre et al., 2005; Wood et al., 2009; Martin et al., 2010a,b). During ten experiments, passive tracers were released from fixed point (at either street level or roof level) or a moving vehicle for

fifteen minute periods. Indoor observations were also collected. Wind tunnel experiments and numerical modelling with direct numerical simulations (DNS) were also conducted during these time periods (Belcher et al., 2015).

From observations during the first phase, changes in wind direction proved to make a large impact on measured concentrations, due to channeling through the street networks. Downwind concentration observations at both the street and rooftop levels were similar in value, suggesting that the plume spread rapidly in the vertical direction. Concentrations indoors proved to be lower than outdoor values, but took longer to become well-mixed. Pedestrian and automobile traffic were documented, noting that instantaneous clouds of pollutants can linger within a street. Simple solutions to avoiding pollution, such as planting trees near roads and building new alleyways to create additional obstacles, were identified from the campaign.

From the previous urban field experiments, the main objectives for each further expanded the scientific understanding of urban canopy layers and their interactions with passive tracers. The experiments were focused within central business districts with minimal foliage coverage. The study areas were large and examined plume behavior at distances > 1 kilometer from the source location. For all campaigns, the tracer released was either SF_6 or PFT and from roof tops or open areas. Both SF_6 and PFT have heavy molecular weights of 146 gmol^{-1} and 300 gmol^{-1}, respectively. Whereas these tracers do illustrate plume behaviors, they are much heavier than PM_{10} and $PM_{2.5}$, so their densities could lead to negative buoyancy effects. While these objectives have provided a plethora of insight on urban areas, there are still many open questions remaining that this thesis hopes to address.

1.4 Gaussian Plume Models and Limitations

Plume dispersion equations were envisioned by Sutton and Simpson (1932) through atmospheric dispersion theory and by Bosanquet and Pearson (1936) through examining the spread of smoke and gases through chimneys. While both did not assume a Gaussian distribution, these were some of the first theoretical analyses to address air pollution dispersion in the atmosphere. The initial study by Bosanquet and Pearson (1936) focused on the space and mass distribution of emissions both from a point and line source, but neglected the reflection of air pollution from the ground surface. Several years later, Sutton (1947a,b) determined several equations to evaluate concentrations from the surface and aloft, as well as peak concentration values within the resulting plume cloud. The equation most relevant to this thesis, adapted from Sutton (1947a), describes the concentration values from a continuous point source at the ground (Equation (1.2)).

$$\chi(x, y, z) = \frac{Q}{\pi C_y C_z \overline{u}(x^{2-n})} \exp \left[-\frac{1}{x^{2-n}} \left(\frac{y^2}{C_x^2} + \frac{z^2}{C_y^2} \right) \right] \tag{1.2}$$

where χ is the concentration (in $\frac{kg}{m^3}$) in x, y, and z coordinates, where x is aligned with the mean wind $\overline{u}$, y is in the lateral direction, and z is in the vertical, Q is the source strength in $\frac{kg}{s}$, $\overline{u}$ is the mean wind speed, C_y and C_z are the generalized diffusion coefficients, and n is the mixing power of the turbulence, which is between 0 and 1.

The result from his calculation of a continuous point source is a normal distribution of concentration values or a Gaussian plume distribution (Figure 1.4). The Gaussian plume distribution was a pivotal derivation because it is a solution to the advection-diffusion equation (defined in Socolofsky and Jirka, 2004), shown in Equation (1.3).

$$\frac{\partial C}{\partial t} + \nabla \cdot (uC) = D\nabla^2 C \tag{1.3}$$
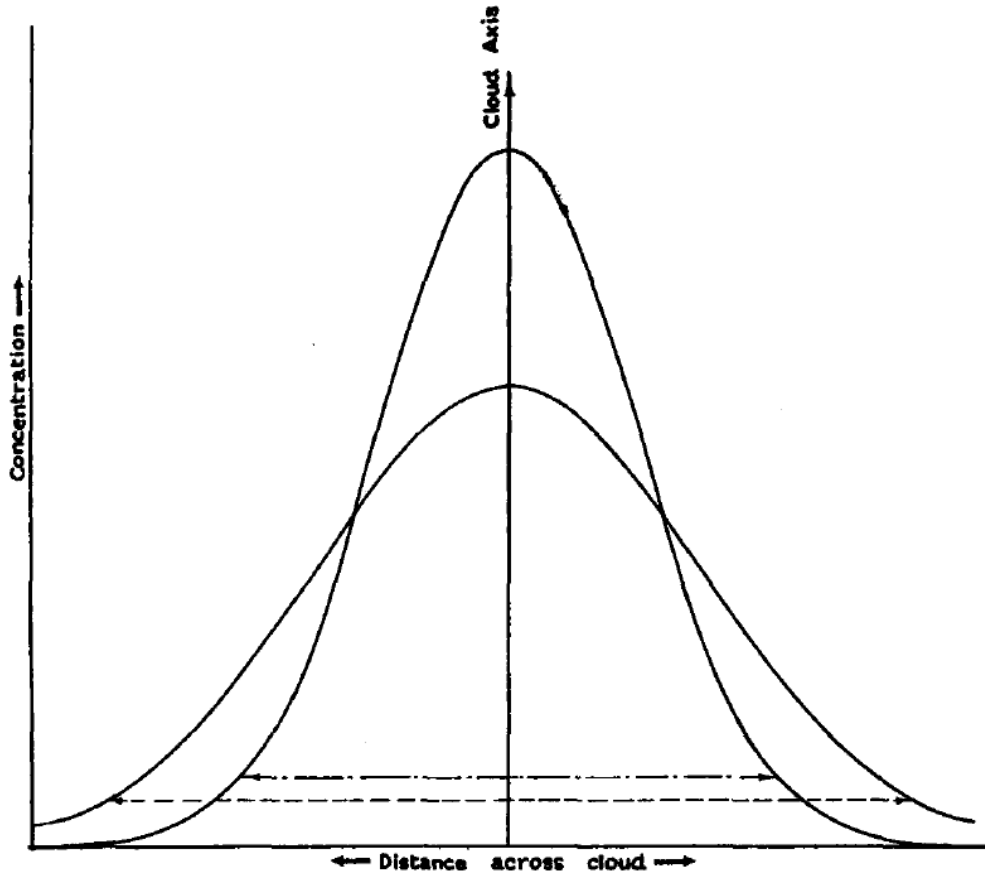
FIG. 1.—Distribution of concentration across wind in the cloud
from a continuous point source.
——·——·——·—— instantaneous width.
—·——·——·—— time-mean width.

Figure 1.4: Gaussian concentration distribution from Sutton (1947a)

.

where C is the concentration and D represents the diffusion coefficient, where $D = k(\partial x)^2$. This coefficient is a property of the turbulence, so it can vary in both space and time.

Cramer (1957) created a diffusion equation that considered Gaussian distribution standard deviations σ_y and σ_z, which account for the horizontal and vertical plume distribution across wind, respectively. While Pasquill (1961) estimated a diffusion equation by defining height and angular spread of a plume by varying weather parameters (and therefore, "stability" classes), Gifford (1961) then defined σ_y and σ_z as

13

standard derivations of the plume from Pasquill's work. From this, a Gaussian plume model was defined for a concentration, χ, from a continuous source with an effective emission height, H. Equation (1.4) is an adapted version of this model from Turner (1969). This equation also agrees with the Seinfeld and Pandis (2006) definition of the Gaussian plume equation.

$$\chi(x, y, z; H) = \frac{Q}{2\pi\sigma_y\sigma_z\overline{u}} \exp\left[-\frac{1}{2}\left(\frac{y}{\sigma_y}\right)^2\right] \exp\left[-\frac{1}{2}\left(\frac{z-H}{\sigma_z}\right)^2\right] + \exp\left[-\frac{1}{2}\left(\frac{z+H}{\sigma_z}\right)^2\right]$$
$$(1.4)$$

where the variables have the same as meaning as Equation (1.2), except for H, σ_y, and σ_z. H is representative of the height of the plume centerline when it becomes level and is equal to the physical stack height plus the plume rise ($H = h + \Delta H$). σ_y and σ_z are defined above. The units for all three variables are in meters.

Stockie (2011) created a diagram that complements this equation (Figure 1.5). The concentration profiles for σ_y and σ_z as the plume moves downwind in the x and y directions are shown, as well as the effective plume height, H.

Gaussian plume models also have been used to model dispersion behavior in the urban canopy. Briggs (1973) and Arya (1999) have used Gaussian plume models to accurately represent dispersion above urban areas farther than 1 km from the source. Previous experiments have also shown Gaussian plume models that are effective below roof top level, but were sufficiently far from the source (x/h > 10, where x/h is the ratio of the distance from the source normalized by the height of the source) (e.g. Davidson et al., 1995, 1996; MacDonald et al., 1997, 1998; Yee and Biltoft, 2004). Large eddy simulations (LES) have been utilized to derive Gaussian plume parameters for an urban canopy (Philips et al., 2013), as well as the use of Gaussian plume-based models to predict dispersion very close to the source (OSPM, Berkowicz, 2000; ADMS, Carruthers et al., 2000). Recently, Belcher et al. (2015) developed a model for predicting dispersion through city street network that converges to a Gaussian
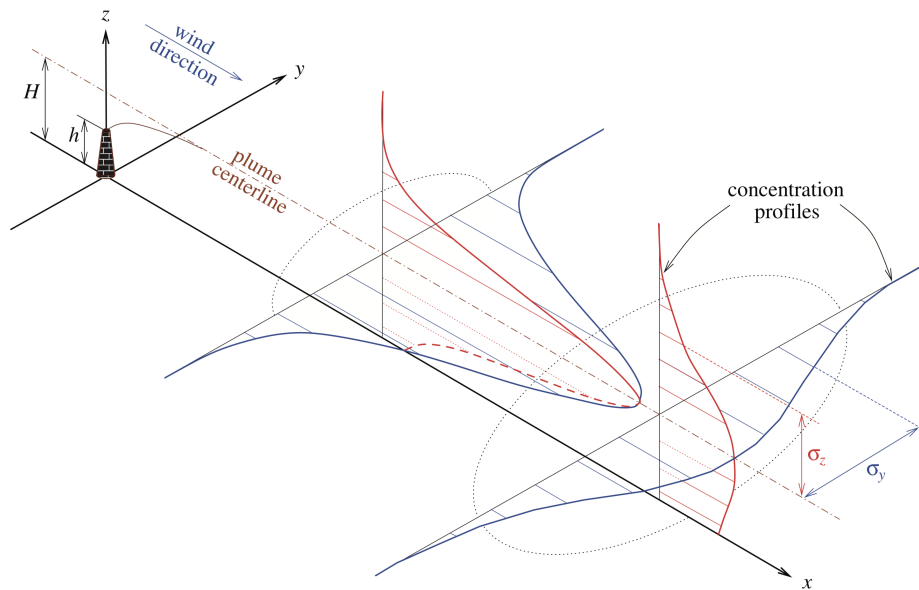
Figure 1.5: Concentration profiles of σ_y (blue) and σ_z (red) for a continuous plume emitted from an elevated point source from Stockie (2011). Plume cross-sections of the the Gaussian shape are shown in the black dotted line, relative to the plume centerline.

plume model and compared their results to the DAPPLE field experiments, DNS, and wind tunnel data. Their model showed encouraging agreement with the DNS and wind tunnel experiments, especially in the near-field. At the same time, model assumptions failed when the wind direction was closely aligned with one set of streets. While this is important to note for future experiments, only 10% of the DAPPLE cases fit this criterion.

Gaussian plume distributions have been used in the past to generalize plume behavior, but there are several questions the remain. For a complex environment (i.e. an urban one), one Gaussian plume may not characterize all of the plume, due to turbulence and urban geometry. A plume could travel in multiple directions through an urban network, a behavior that would not be captured by a Gaussian plume distribution. This limitation is also another problem that this thesis hopes to address.

1.5   Research Questions

To address some of aforementioned limitations in urban field campaigns, a new field experiment was conducted in a suburban neighborhood in Vancouver, British Colombia, Canada. The research objectives of this thesis are to address some of the remaining research with this new dataset. The questions that this thesis will focus on are:

1. Is there a successful way to obtain near source (< 1 km) observations of a plume released at ground level on a neighborhood scale?

2. Can a Gaussian plume model characterize plume behavior within the urban canopy? If not, what can be used?

3. Does the plume eventually behave in a Gaussian manner? At what point downstream of the source does this occur?

16

4. To what extent do turbulence characteristics and urban geometry affect plume behavior in an urban environment?

Chapter 2

Methodology

2.1 Dataset: Sunset Neighborhood

In June 2017, an urban dispersion experiment was conducted in the Sunset neighborhood of Vancouver, British Columbia, Canada. The one of the objectives for this experiment was to develop a new dataset that could be used to examine the impact of urban form (such as trees and buildings) on the near source plume characteristics of urban particulate pollutants. The other objective was to use the dataset to then validate high resolution resolving turbulence simulations (e.g. LES) and obstacle resolving diagnostic dispersion models (e.g. Quick Urban & Industrial Complex (QUIC) Dispersion Modeling System; Pardyjak and Brown, 2001) for dispersion in the UCL.

2.1.1 Layout of Vancouver, British Columbia

Vancouver, British Columbia, Canada is the largest city in the province and the eighth largest municipality in the country (City of Vancouver, 2019). Spanning 44 square miles, Vancouver's population is about 630,000, with a metropolitan area of over 2 million people. This city contains a major downtown area to the north, several suburban neighborhoods to the south, and the University of British Columbia (UBC) to the northwest (Figure 2.1). While several experiments have focused on the downtown urban populations and environments (e.g. Oke, 1976; Nunez and Oke, 1977; Runnalls and Oke, 2000), the Sunset neighborhood, one of the suburban neighborhoods, was where this experiment took place.

Figure 2.1: Map of Greater Vancouver, taken from Google Earth. Several locations are highlighted, with the University of British Columbia in white, downtown Vancouver in green, and the Sunset Neighborhood in red.

2.1.2 Sunset Tower

The Sunset neighborhood is located in south-central Vancouver (49° 13' 33.96", 123° 4' 42.24"). This neighborhood contains the Sunset Tower, a 28 meter (above ground level) urban climate tower that contains a myriad of instruments. The tower is located at the Mainwaring substation BC Hydro and serves as an urban climate research facility. The UBC Geography department and Laboratory for Atmospheric Research on Greenhouse Gas Exchange use the facility to understand the meteorological, hydrological, biogeochemical and climatological processes that modify cities through land-atmosphere exchange and biogeochemical cycling, as well as the role that cities have on climate change. The tower has been semi-operational since it was established in 1978 (Oke, 1979a), but has provided year-round data since 2007 (e.g. Oke and McCaughey, 1983; Grimmond and Oke, 1991; Christen et al., 2011). These continuous measurements include meteorological conditions, radiation, turbulent fluxes, and carbon dioxide concentrations. Instruments on the tower's eddy covariance system include a 3-D sonic anemometer (Campbell Scientific CSAT3),

19
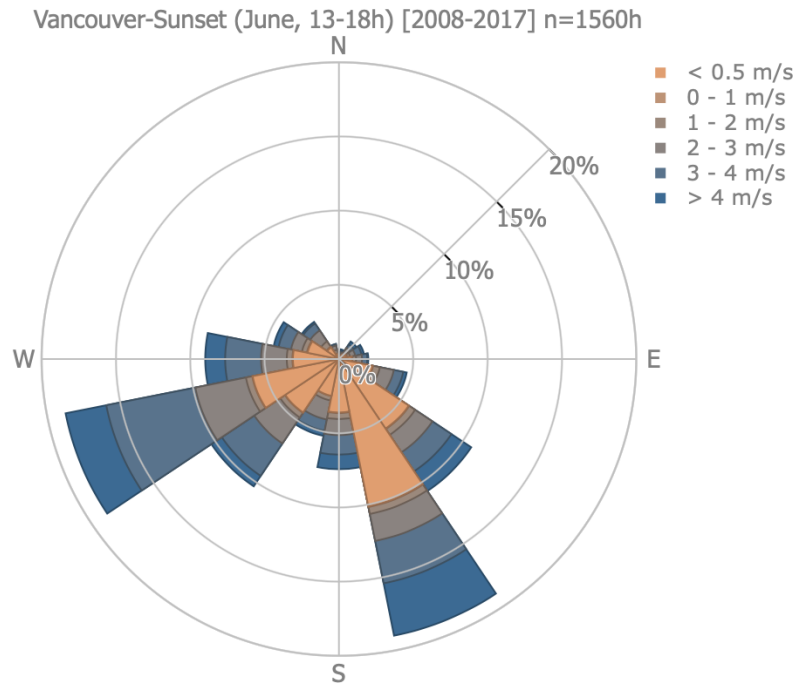
Figure 2.2: Wind rose of dominant wind directions at Sunset Tower during 13h-18h local time in June from 2008-2017 (Christen et al., 2017).

cup anemometer (RM Young 03102 Wind Sentry), temperature and humidity probe (Vaisala HMP), radiometer (Kipp & Zonen CNR1 #000265), methane open-path IR gas analyzer (LI-COR Li-7700), and CO_2/H_2O open-path IR gas analyzer (LI-COR Li-7500). Along with observations on the top of the tower, year-round surface observations are available during the operational time period (accessible at http://ibis.geog.ubc.ca/~achristn/infrastructure/sunset.html). Wind roses for the dataset from 2007-2017 are viewable as well (Figure 2.2). From 2008 to 2010, nearby homes were also monitored for their water usage, soil hydrology on their land, and space heating requirements (Järvi et al., 2011).
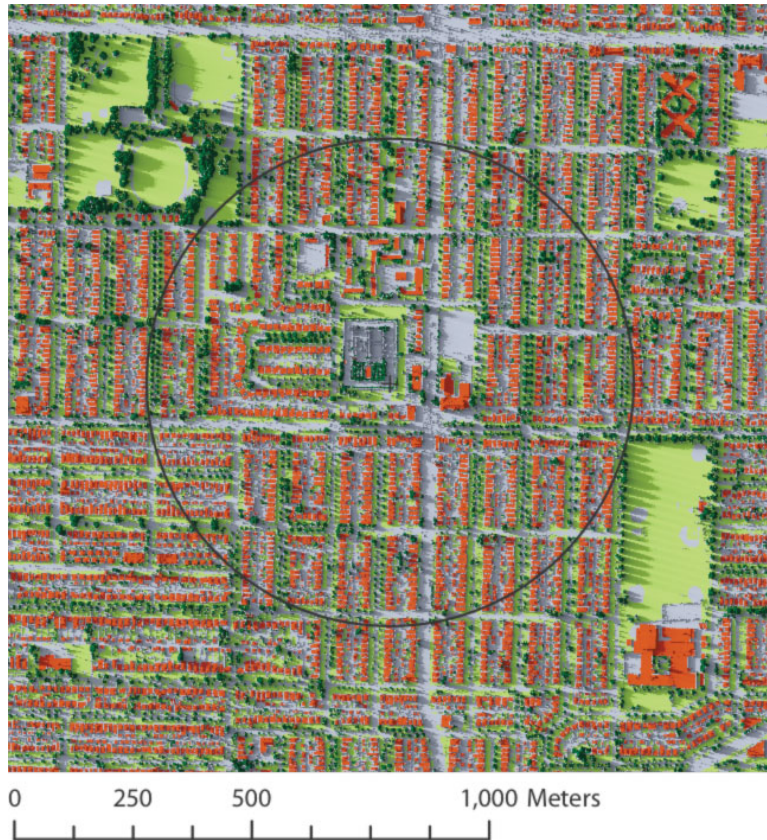
Figure 2.3: This site and the surrounding area within a 1 km radius has its characteristics documented in the form of a 50m raster Geographic Information System based on several high-resolution LiDAR scans at 1 m resolution (Goodwin et al., 2009)

.

Vancouver-Sunset has been utilized for several large field campaigns through its tenure. The tower is a member of the International Association for Urban Climate (IAUC) Urban Flux Network (Fluxnet ID: 'Ca-VSu'), where it was active and operational from 2001-2003 and 2008-2017. The tower is also a member of the Multi-city Urban Hydrometeorological Database (MUHD), where nine other towers are compared internationally. From 2008 to 2010, the tower was part of the Canadian Foundation for Climate and Atmospheric Sciences (CFCAS) network of instruments called the Environmental Prediction in Canadian Cities (EPiCC) (Liss et al., 2010; Crawford et al., 2012; van der Laan et al., 2012; Christen et al., 2013). As a result, the tower location, as well as the surrounding area (up to a 1 km radius), has been well-documented. A high-resolution topographical LiDAR (Light Detection and Ranging) has been utilized to characterize the land around the tower at 1 m resolution (Goodwin et al., 2009; Christen et al., 2010). A 50 m raster visualization of the surrounding area is viewed using Geographical Information Systems (GIS) (Figure 2.3).

While field experiments have defined the environment in and surrounding the Sunset Tower, large eddy simulations (LES) have also been conducted focusing on this area. Giometto et al. (2017) determined the effects that vegetation and buildings can have on atmospheric flow in several neighborhoods nearby. They focused on several different street networks within the neighborhood to provide a wide variety of urban canopies types and their different distributions of buildings and foliage. From these various layouts, Giometto et al. (2017) also examined how flow characteristics altered with changing surface parameters.

2.2 TRUC Campaign

Tracer Release in an Urban Canopy (TRUC) was a field campaign conducted in the Sunset neighborhood during June 2017. Several years of wind climatologies and the micrometeorology of the area, described in subsection 2.1.2, are available from

the Sunset Tower. The month of June was chosen for its availability, but does show consistent wind direction from the south, primarily from the southeast and southwest. Similarly, the time frame for each day was determined by wind climatologies from the Sunset Tower. Start and end times were approximately between 13:00 and 16:00 local time (Table 2.1). Four days were chosen to run the experiments, with an overall of fourteen releases over the entire duration of the field campaign. Experiment days were chosen the day prior, based on forecasted weather conditions. Dry conditions were necessary for the campaign to deploy each day. If precipitation occurred, the releases were delayed until the precipitation stopped.

Date	Release	Start time	End time	Release Location
June 19th	2	14:52	15:09	49° 13' 24.3372", -123° 4' 56.679"
	3	15:52	16:09	
June 22nd	4A	13:30	13:49	49° 13' 24.6246", -123° 4' 59.3718"
	4B	13:55	14:14	
	5A	15:04	15:23	
	5B	15:29	15:48	
June 27th	6A	13:32	13:52	49° 13' 23.4444", -123° 4' 53.3172"
	6B	13:56	14:16	
	7A	15:13	15:33	
	7B	15:38	15:58	
June 29th	8A	13:45	14:05	49° 13' 26.6844", -123° 4' 53.184"
	8B	14:15	14:35	
	9A	15:17	15:36	
	9B	15:46	16:06	

Table 2.1: Release date, start times and end times for each campaign day in local time (PDT), and latitude and longitude of the release location for each day

2.2.1 Configuration and Instruments

The four days chosen for TRUC were June 19th, 22nd, 27th, and 29th. Each configuration was composed of a source (see Section 2.2.2), fifty impaction traps, a mobile 3D sonic anemometer tower with two heights (16 m and 1.5 m), and five 2D sonic anemometers at ground level (1.5 m). For every new experiment day, the configuration of the impaction trap array varied. The first day, June 19th, was configured along East 51st Avenue in the east-west direction and mainly on Ross Street and a parallel alleyway in the north-south direction (Figure 2.4). The source for the 19th was placed near the intersection of 51st and Ross. June 22nd was set up in a similar way, but shifted to the east to include more impaction traps on Sherbrooke Street (Figure 2.5). Similarly, the source location was moved, but kept near the same intersection as June 19th. June 27th was also along East 51st Avenue, but was along Sherbrooke Street and Inverness Street in the north-south direction (Figure 2.6). This source location was placed in the middle of Sherbrooke, south of its intersection with 51st. June 29th focused mainly on Sherbrooke Street, but included Inverness Street and two alleyways, one east-west oriented and the other north-south oriented (Figure 2.7). Like the source location for the 27th, the point source was in the middle of Sherbrooke, but even farther south of its intersection with the side street. While the same instruments were utilized for each day of the campaign, the configuration of the experiment at each location was varied to provide a diverse dataset.

The fifty impaction traps (Thiessen et al., 2016; Miller et al., 2015, 2018) were two vertically oriented rods attached on the bottom to a horizontally oriented rod (Figure 2.8). During the twenty minute duration of each release, the impaction traps were operational, rotating constantly and collecting any particles entering the sampling volume swept out by the rods. The rods were greased on one side to capture the particles released. The traps were located at pedestrian level at 1.5 meters. The mobile 3D sonic anemometer tower was a portable instrument that had two sonic anemometers

Figure 2.4: Configuration of all instruments utilized for June 19th. The yellow/green point represents the source, magenta points represent the fifty impaction traps, and cyan points represent the 2D sonic anemometers. A compass pointing north is shown in the red box, showing the orientation of the street network.
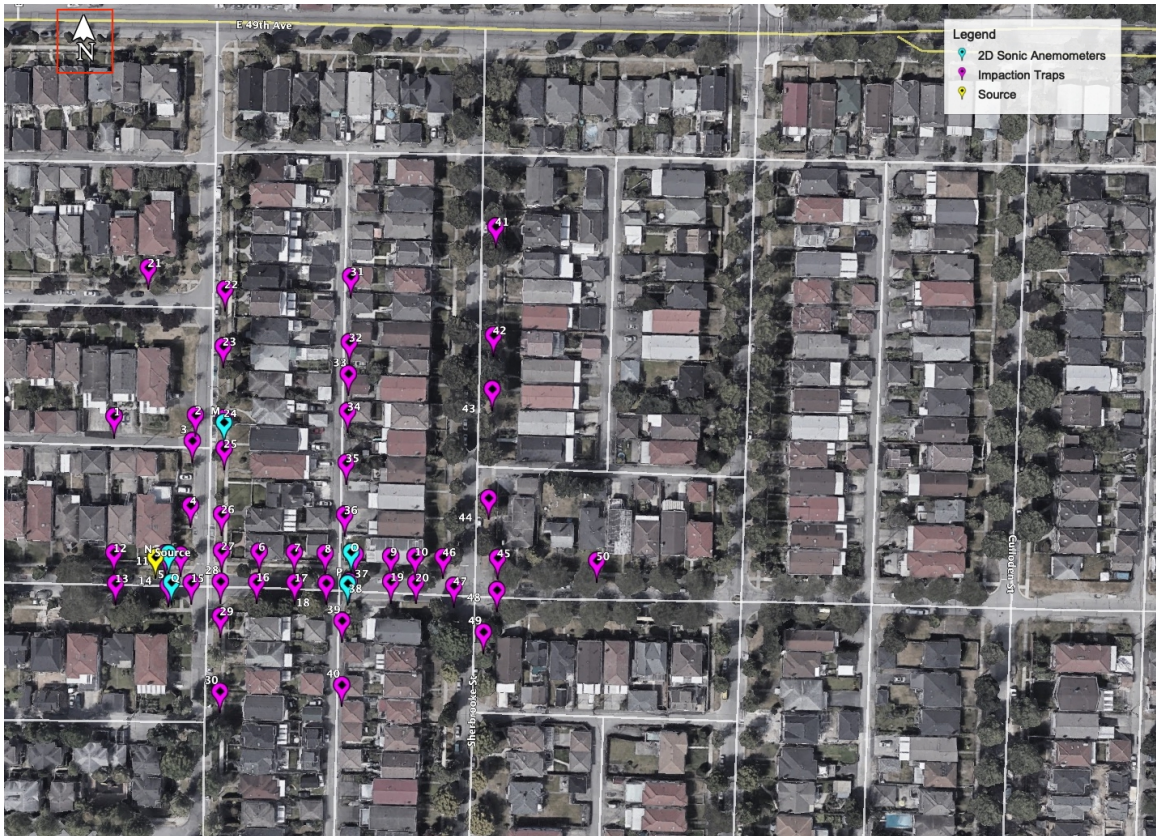
Figure 2.5: Same as figure 2.4, but for June 22nd.
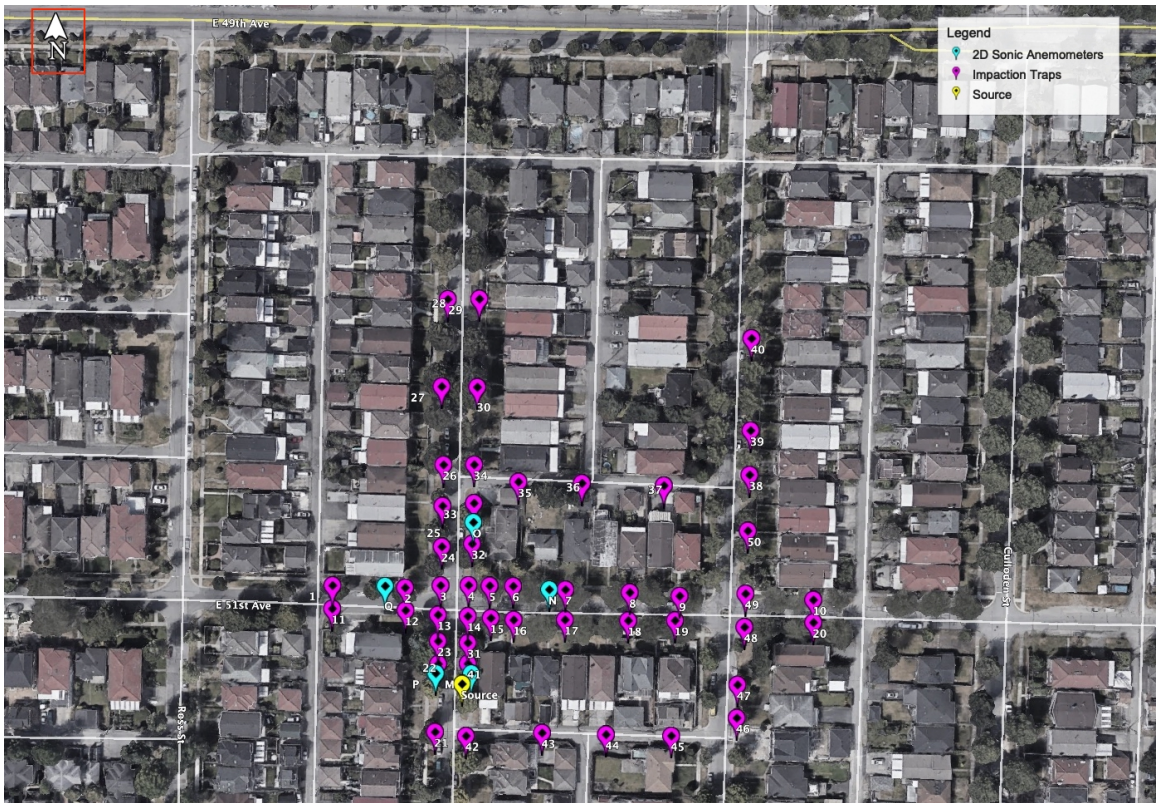
Figure 2.6: Same as figure 2.4, but for June 27th.

Figure 2.7: Same as figure 2.4, but for June 29th.

at 16.6 meters and 1.5 meters (Figure 2.9). The five 2D sonic anemometers (LEMSv2; Gunawardena et al., 2018) deployed each day were also located at pedestrian level (1.5 meters) (Figure 2.10). The sonic anemometers were identified by letters (M, N, O, P, Q), but the last day utilized an additional sonic anemometer "R" for releases 8A, 8B, 9A, and 9B to replace "Q". The time data was not configured for the entirety of TRUC for 2D sonic "N", so the only 2D sonics through all four release days were "O" and "P".

2.2.2   TRUC Source

The source for TRUC was composed of 3 ultrasonic atomizer nozzles (Sonaer Inc.). The source was mounted onto the back of a truck and parked in one location for each of the releases (Figure 2.11). All three nozzles were located at 2.4 meters above ground attached to the truck (Figure 2.12).

Yellow/green (UVPMS-BY2-1.00, Cospheric, LLC) and violet (UVPMS93-BV-1.00, Cospheric, LLC) polyethylene microspheres of varying diameters (> 90% of diameters in range of 10-45 μm) were provided for the campaign (Figure 2.13). The average diameter for the yellow/green and violet microspheres were 32.8 μm and 33.1 μm, respectively, which were released during TRUC. Four 50 milliliter syringes were utilized to suspend the particles in a 90% ethyl alcohol solution and loaded into a syringe pump (Model 22, Harvard Apparatus). The solution was constantly stirred with rotating magnets to prevent clumping in the atomizer nozzles. To expedite the process, the yellow/green and violet microspheres were collected on the same rods, except on June 19th. Releases "A" and "B" were then conducted within 5-10 minutes of each other for all four days. Therefore, the releases labelled "A" are for the violet microspheres, while the "B" are for the yellow/green microspheres. Releases 2 and 3 on June 19th only used the yellow/green microspheres.

Figure 2.8: Close-up of one impaction trap, based off of Thiessen et al. (2016)

Figure 2.9: Mobile 3D sonic anemometer tower with both 3D sonic anemometer heights labelled

Figure 2.10: Example of a 2D sonic anemometer, based off of Gunawardena et al.
(2018)
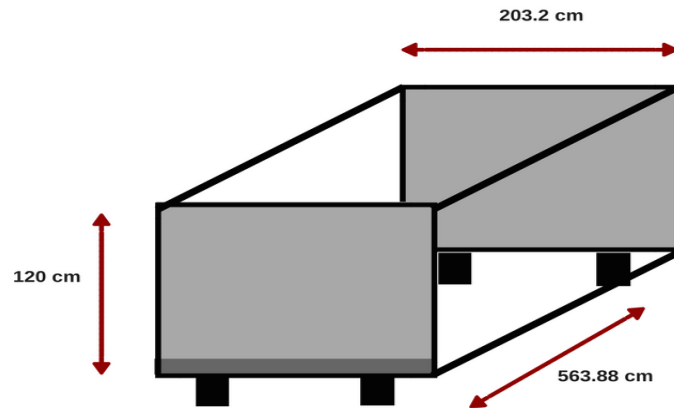
Figure 2.11: Dimensions of source truck
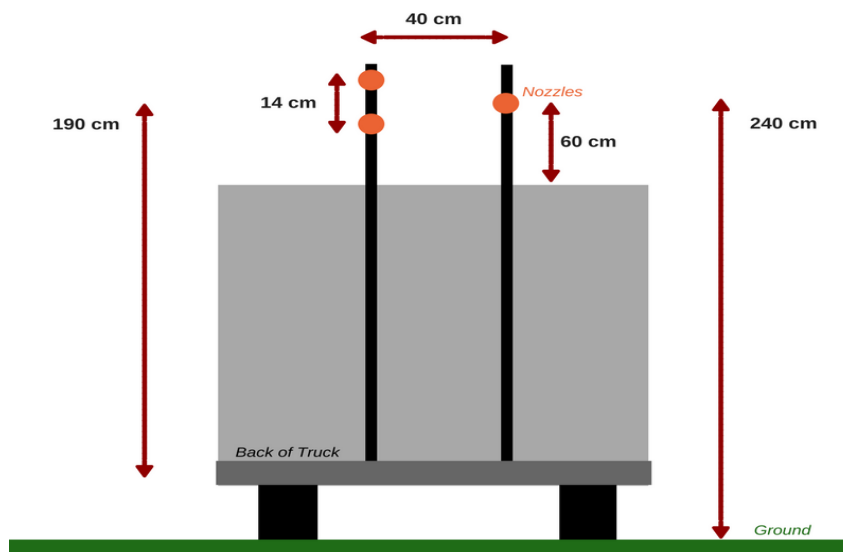
Figure 2.12: Diagram of source and its location on the truck
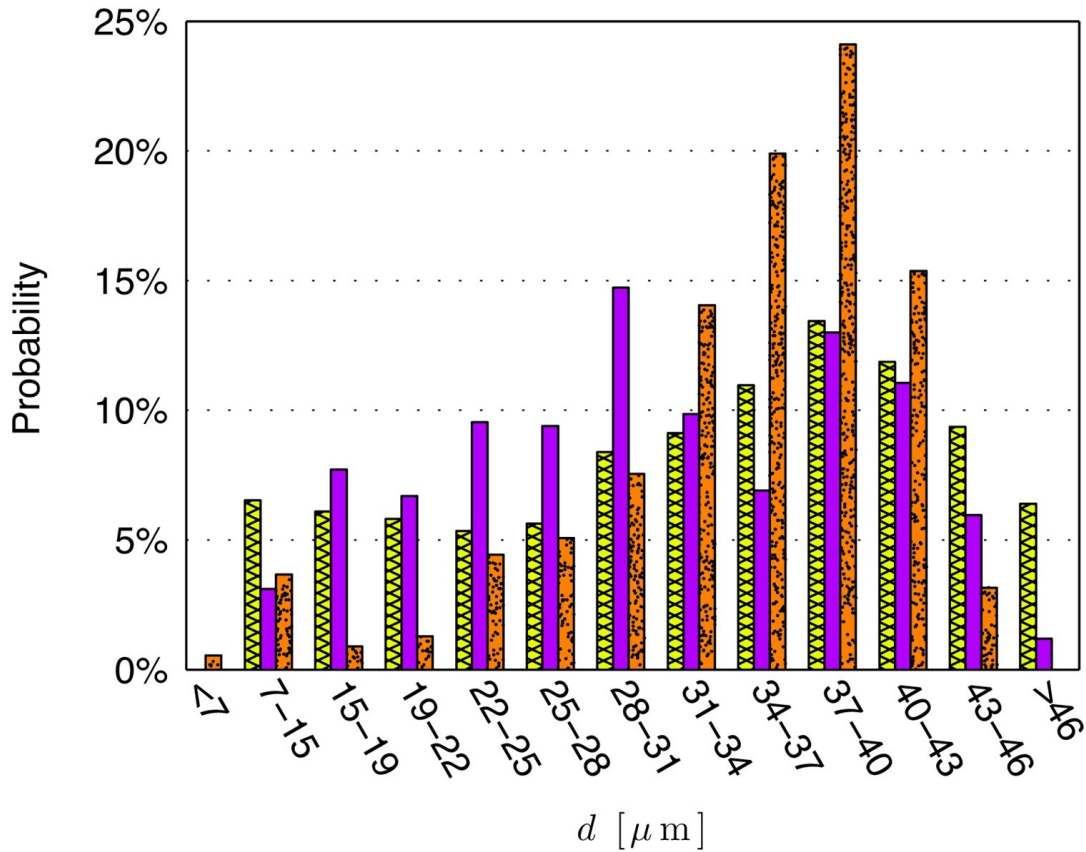
Figure 2.13: Range of diameters of polyethylene microspheres provided during TRUC. Only the yellow/green and violet microspheres were used (Miller et al., 2018).

The impaction trap rods were collected at the end of each release time. Using a fluorescence stereomicroscope (Miller et al., 2015), the particles were manually counted by two separate individuals to confirm the particle count on each rod. Both colors can be distinguished under the microscope by using different filters (365 nm for yellow/green and 584 nm for violet).

2.3   Concentrations

The number of microspheres collected at each impaction trap were counted and converted into a concentration value c with the units of number of particles/m^2. (Eq. 2.1).

$$c = \frac{2 \times \overline{u} \times p \times m}{V \times 0.406 \times 20 \times q \times 0.001} \tag{2.1}$$

where $\overline{u}$ represents the mean wind speed at 1.5 meters for the release time frame, p represents the average particle count between both collection rods per impaction trap, m represents the mass of the particles (either violet or yellow/green), V represents the volume sampled by each impaction trap in L/min, 0.406 represents the sampling length ratio, 20 represents the release time in minutes, and q represents the plume source strength in g/s. The sampling length ratio was determined for each trap by the length of the collection rod that was imaged divided by the total length of the impaction trap, which was $\frac{1.42\ cm}{3.5\ cm}$. The average mass of microspheres for each color was used for these calculations (32.8 μm and 33.1 μm for yellow/green and violet, respectively). The source strength, q, was determined by the volume of the syringes in milliliters used divided by time in seconds: $q = \frac{V}{t} = \frac{4\ \times\ 50\ mL}{20\ minutes\ \times\ 60\ \frac{seconds}{minute}} = 200\ \frac{mL}{s} = 200\ \frac{g}{s}$.

2.4   Uncertainties with concentrations

Complications during some releases may have affected the particle collected and therefore, the concentration calculated for each impaction trap. During Releases 2 and 3, one of the nozzles in the source was clogged, which would mean the source strength, q, may be lower than what was expected.

While the collection process overall was successful, there are several instances were the concentration may be underestimated. The impaction traps either malfunctioned or collection rods flipped over while in use. Some errors were during the removal

process of rods, such as dropping, scratching, or accidentally touching the individual rods. External factors also may have affected the particles collected, such as automobiles, pedestrian interaction, and lingering smoke from a nearby home. While the exact impact of these external factors is unknown, it was understood that the collected rods were still viable.

2.5 The Superposition of two Orthogonally-oriented Gaussian plume distributions (SOG)

Previous experiments have demonstrated that scalar plumes can be a variety of different shapes and sizes and may be influenced by the local topography and urban geometry. A Gaussian plume distribution (equation 1.2) is typically used to describe these plumes over flat, homogeneous terrain, since it is a solution to the advection-diffusion equation. Observed plumes in urban areas are frequently non-Gaussian, due to urban form and vegetation (Drivas and Shair, 1974; Jones, 1983; Mole and Jones, 1994; Yee and Biltoft, 2004; Finn et al., 2010).

To characterize the shape of the plumes that were observed in the TRUC data, the Superposition of two Orthogonally-oriented Gaussian plume distributions (SOG; Miller et al., 2018) was utilized as an interpolant. Instead of only using one Gaussian plume distribution, SOG uses two orthogonal Gaussian distributions to define a plume that may be non-Gaussian either close or far from the source (Figure 2.14). While a single Gaussian distribution forces the skewness to 0 and kurtosis to be 3, the SOG permits non-Gaussian higher order plume moments and behavior while still being a solution to the advection-diffusion equation.

For each point evaluated, SOG determines a concentration (represented by Π) in number of particles per m^2 (Equation 2.2). The SOG was fit to the TRUC data by using a mulitvariable nonlinear least-squared-error optimization. This is done by using the lsqnonlin function of the optimization toolbox in MATLAB. Since the data
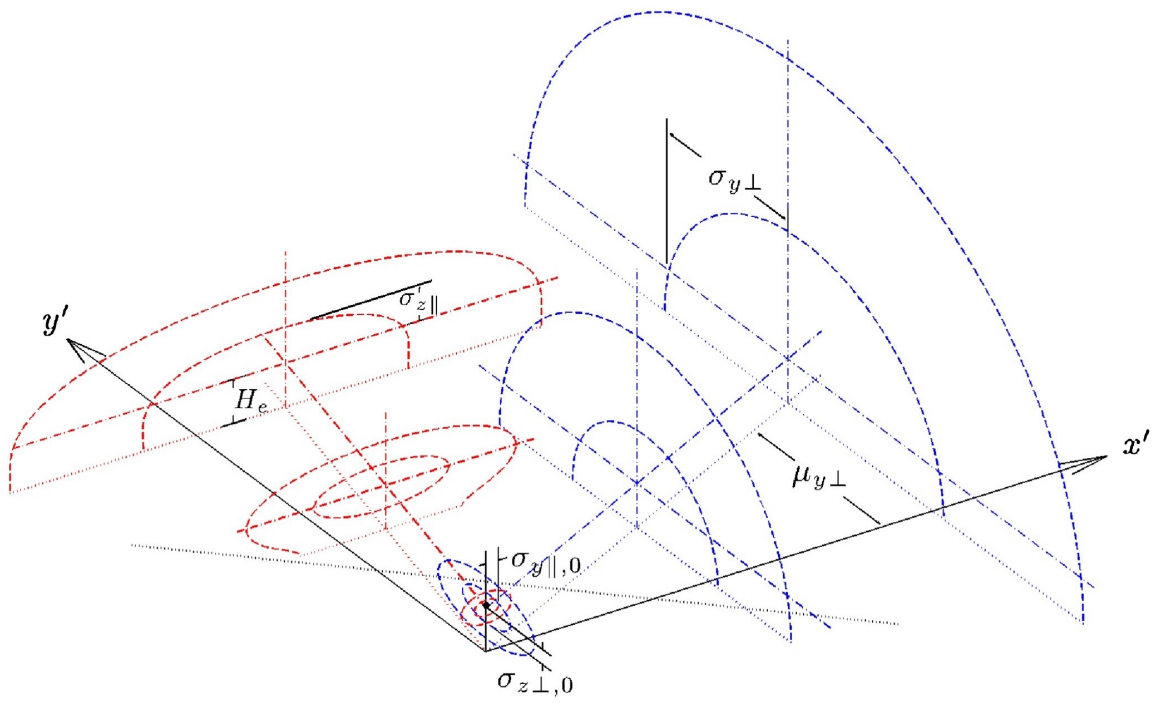
Figure 2.14: Visualization of Superposition of two Orthogonally-oriented Gaussian plume distributions (Miller et al., 2018). Variables labelled here are from Equation (2.2).

is too sparse to directly calculate these values, SOG provides an interpolant between data points so plume moments can be calculated.

$$\Pi(x', y', z) =$$

$$P\left[\frac{A_\perp}{2\pi\sigma_{y_\perp}\sigma_{z_\perp}}\exp\left(\frac{-(y_\perp - \mu_{y_\perp})^2}{2\sigma_{y_\perp}^2}\right)\right.$$

$$\left.\times\left(\exp\left(\frac{-(z - H_e)^2}{2\sigma_{z_\perp}^2}\right) + \exp\left(\frac{-(z + H_e)^2}{2\sigma_{z_\perp}^2}\right)\right)\right] +$$

$$(1 - P)\left[\frac{A_\parallel}{2\pi\sigma_{y_\parallel}\sigma_{z_\parallel}}\exp\left(\frac{-(y_\parallel - \mu_{y_\parallel})^2}{2\sigma_{y_\parallel}^2}\right)\right.$$

$$\left.\times\left(\exp\left(\frac{-(z - H_e)^2}{2\sigma_{z_\parallel}^2}\right) + \exp\left(\frac{-(z + H_e)^2}{2\sigma_{z_\parallel}^2}\right)\right)\right]$$

(2.2)

The SOG three-dimensional interpolant uses the spanwise and streamwise coordinates, x' and y' respectively, for the component of the SOG parallel to the mean wind, while the streamwise and spanwise coordinates for the perpendicular component to the mean wind are x' and y' respectively. P is a weighting constant that must be between 0 and 1, which is used to enforce Equation 2.2 as a valid solution to the advection-diffusion equation. The "A" parameters are magnitude adjustments that account for mass removal, $A_\perp = exp(-m_{A_\perp}x')$, $A_\parallel = exp(-m_{A_\parallel}y')$ (Miller et al., 2015). $\sigma_{y_\perp}$ and $\sigma_{y_\parallel}$ are the standard deviations of the plume in the spanwise direction in the perpendicular and parallel directions: $\sigma_{y_\perp}^2 = \sigma_{y_\perp,0}^2 + m_{\sigma_{y_\perp}}^2 x'^2$, $\sigma_{y_\parallel}^2 = \sigma_{y_\parallel,0}^2 + m_{\sigma_{y_\parallel}}^2 y'^2$. $\sigma_{z_\perp}$ and $\sigma_{z_\parallel}$ are standard deviations of the plume in the vertical direction in the perpendicular and parallel directions: $\sigma_{z_\perp}^2 = \sigma_{z_\perp,0}^2 + m_{\sigma_{z_\perp}}^2 x'^2$, $\sigma_{z_\parallel}^2 = \sigma_{z_\parallel,0}^2 + m_{\sigma_{z_\parallel}}^2 y'^2$. $\mu_{y_\perp}$ and $\mu_{y_\parallel}$ are the spanwise offsets of the mean plume centerline in the perpendicular and parallel directions: $\mu_{y_\perp} = m_{\mu_{y_\perp}}x'$, $\mu_{y_\parallel} = m_{\mu_{y_\parallel}}y'$. The "$H_e$" parameter describes the effective plume centerline height: $H_e = H_r - (dH + m_H x')$, $H_e = H_r - (dH + m_H y')$. H_r describes the height of the release, dH is the initial fall distance at the source, and m_H is the rate of fall with downwind distance.

During the TRUC experiment, all of the impaction traps were at one and only height of 1.5 meters. Therefore, the effective plume centerline height is equal to the

vertical coordinate of the instruments, which forces the effective plume centerline height exponential terms in the perpendicular and parallel components of SOG to equal 1. Due to the lack of other vertical coordinates during the campaign, the σ_z components must equal 1. Therefore, a 2D version of the SOG equation was used as an interpolant for the dataset used (Equation 2.3).

$$\Pi(x', y') = P\left[\frac{A_\perp}{2\pi\sigma_{y_\perp}\sigma_{z_\perp}} \exp\left(\frac{-(y_\perp - \mu_{y_\perp})^2}{2\sigma_{y_\perp}^2}\right)\right] + (1-P)\left[\frac{A_\parallel}{2\pi\sigma_{y_\parallel}\sigma_{z_\parallel}} \exp\left(\frac{-(y_\parallel - \mu_{y_\parallel})^2}{2\sigma_{y_\parallel}^2}\right)\right]$$
$$(2.3)$$

The variables in this 2D version of the SOG are the same as previously mentioned.

Chapter 3

Results

Turbulence statistics and urban geometry are crucial components of understanding plume behavior in an urban area (e.g. Oke, 1988; Grimmond and Oke, 2002; Britter and Hanna, 2003). To characterize the plume behavior during the TRUC campaign, it is necessary to first examine plume shape by using the SOG interpolation. The turbulence and urban geometry of the Sunset neighborhood then will be interpreted to possibly explain the plume's shape and spread.

Each day during TRUC had a unique configuration of instruments. For this analysis, the release days will be defined by the source location to further determine causes of plume characteristics. June 19th will be labelled as "Ross Intersection", for the location of the source sits just east of the intersection of E 51st Avenue and Ross Street. The June 22nd source location is in a similar location as June 19th. Due to the impaction traps aligning with the E 51st and Sherbrooke Street intersection, this day will be identified as "Sherbrooke-Ross Intersection". June 27th has its source location to the south of the intersection of E 51st and Sherbrooke, but also is north of an intersection of Sherbrooke and an alleyway. Therefore, June 27th will be named "In-between Sherbrooke". Finally, the source location for June 29th was set on Sherbrooke St., but far south of the closest intersection, so the last day will be labelled as "Along Sherbrooke". The impaction traps were oriented along the streets in north-south and east-west direction during TRUC. The SOG is an interpolant, so a meshgrid was used throughout this analysis to interpolate in between observations of TRUC.

3.1 Mean Flow and Turbulence Statistics

It is also important to characterize how turbulence and mean flow characteristics contribute to plume properties. Evaluating turbulence statistics within the urban canopy layer can possibly explain the shape of the released plume for any of the releases. From TRUC campaign, the 2D and 3D sonic anemometers were used for this specific purpose. Turbulence statistics from the 3D mobile sonic tower for each release are shown in Table 3.1. The mean wind speed, $(\overline{u})$, and mean wind angle, (α), were averaged over the twenty minute releases from the 3D sonic anemometer tower at both heights (16.6 m and 1.5 m). It is important to note that while the mobile tower data was used for the analysis of the turbulence, an ensemble average of the 2D and 3D sonic measurements for mean wind speed, mean wind angle $(\langle\alpha\rangle)$, and standard deviations for $\overline{u}$ and $\langle\alpha\rangle$ were also calculated for each release to assess spatial variability in turbulence statistics (see Appendix Chapter A).

From the u, v, w, T perturbations from the 3D sonic anemometers, several other turbulence variables were calculated. The friction velocity was calculated as: $u_* = \left[\overline{u'w'}^2 + \overline{v'w'}^2\right]^{\frac{1}{4}}$ (Garratt, 1992). The Obukhov length was defined as: $L = -\frac{u_*^3 \overline{T_o}}{\kappa g \overline{w'T_o'}}$ (Obukhov, 1946), where κ is the von Kármán constant (~ 0.4), g is gravitational acceleration, $\overline{T}$ and T' are the mean temperature and temperature perturbation observed at both heights, and $\overline{w'T_o'}$ is the kinematic surface heat flux. The Monin-Obukhov stability parameter (z/L) was also defined to determine the stability of the surface layer.

The mean wind direction varies by 44.2° across all of the releases, providing a similar result to the data from the Sunset Tower that illustrated a predominant wind direction from the southwest (approximately 240°). The mean wind speeds at 1.5 meters were all < 3 m/s, but did vary during the release periods. While these wind speeds only vary by 0.3 m/s, this variation could change the shape of the plume released. Similarly, the range of wind angles can also drastically change the shape

of the plume, based on the source location and urban geometry (e.g. Belcher et al., 2015). The friction velocity for TRUC was 0.6 m/s or lower for each release, varying only by 0.23 m/s at 1.5 meters and 0.35 m/s at 16.6 meters. The Obukhov length, L, and Monin-Obukhov stability parameter, z/L, were negative for all releases and both heights, illustrating unstable conditions during TRUC.

From these turbulence statistics, it is clear that the atmospheric conditions during each day were similar in terms of mean wind, friction velocity, and stability parameter. While the mean wind direction was predominantly from the southwest for the entirety of TRUC, this variation of approximately 40° will prove to be important regarding urban geometry.

3.2   SOG Goodness-of-Fit

Before interpolating over the entire TRUC domain for each release, the SOG was first utilized to calculate concentrations at the TRUC impaction trap locations. An example of this for release 2 on June 19th is shown in Figure 3.1. The TRUC concentration values (Figure 3.1a) agree visually with the SOG concentration values (Figure 3.1b) close to the source. About 5 meters to the east of the source, the TRUC and SOG concentrations are the same color of yellow, denoting the highest concentration. Farther away from the source to the northeast along the E 51st Avenue, the concentrations decrease, which is expected (e.g. Rotach et al., 2004, 2005). Similarly, points to the northwest and southeast along Ross Street have lower concentration values. After visually comparing the SOG and TRUC concentrations, goodness-of-fit statistics were calculated for each release. Only comparison plots between the observed and predicted concentrations will be shown for this analysis.

Statistics were computed to compare the TRUC concentrations to the SOG concentrations, R^2 and NRMSE. R^2 is a statistical measure of how closely the data are to a fitted linear regression line. This variable was used to show how closely the SOG

Table 3.1: Variables for releases at different heights, 16.6 m and 1.5 m, for 3D sonic mobile tower

Releases	u_* ($\frac{m}{s}$)		L (m)		$\frac{z}{L}$		$\overline{u}$ ($\frac{m}{s}$)		α (°)	
	16.6m	1.5m	16.6m	1.5m	16.6m	1.5m	16.6m	1.5m	16.6m	1.5m
2	0.28	0.08	−1.156	−0.054	−14.4	−27.8	2.81	1.78	234.3	232.5
3	0.52	0.31	−4.867	−1.536	−3.41	−0.98	0.93	0.95	245.1	237.3
4A	0.60	0.11	−3.859	−0.040	−4.30	−37.2	2.41	1.57	257.8	262.6
4B	0.63	0.21	−4.562	−0.305	−3.64	−4.90	2.48	1.96	251.8	248.6
5A	0.57	0.19	−3.977	−0.296	−4.17	−5.07	2.45	1.78	255.7	253.1
5B	0.50	0.10	−3.279	−0.047	−5.06	−31.8	2.06	1.62	252.3	246.6
6A	0.43	0.26	−1.997	−0.524	−8.31	−2.86	2.82	1.59	218.4	223.4
6B	0.58	0.27	−3.781	−0.656	−4.39	−2.29	2.83	1.89	236.5	233.7
7A	0.59	0.26	−3.966	−0.551	−4.19	−2.72	2.25	1.77	246.9	244.9
7B	0.52	0.23	−2.691	−0.495	−6.17	−3.03	2.31	1.68	242.4	241.8
8A	0.58	0.05	−4.132	−0.007	−4.02	−203	2.03	1.67	256.8	252.1
8B	0.52	0.11	−2.986	−0.054	−5.56	−27.9	1.84	1.28	248.0	234.7
9A	0.47	0.09	−2.959	−0.032	−5.61	−47.3	1.73	1.37	253.7	245.5
9B	0.57	0.11	−1.156	−0.110	−4.21	−13.6	1.84	1.47	251.2	247.1

concentrations agreed with the TRUC concentrations. If the TRUC and SOG concentrations matched perfectly, the R^2 value for that release would be 1. Conversely, if the TRUC and SOG concentrations did not agree and had no correlation, the R^2 value would be 0. R^2 is defined as

$$R^2 = 1 - \frac{\Sigma(y_i - y_{SOG})^2}{\Sigma(y_i - \overline{y})^2}$$

where y_i represents the TRUC data points, y_{SOG} represents the SOG values, and $\overline{y}$ represents the mean value of the TRUC concentrations. To visualize deviations from the regression line, lines of a factor of 2 and factor of 10 different from the linear fit were added, denoted as FACT 2 and FACT 10 for the plots representing each TRUC release.

The other statistical variable used comes from the root mean square error (RMSE). RMSE is the standard deviation of the predicted errors or a measure of how far the SOG concentrations deviate from the best fit line. RMSE is defined as

$$RMSE = \sqrt{\frac{1}{n}\sum_{i=1}^{n-1}(y_i - y_{SOG})^2}$$

The normalized root mean square error (NRMSE) is then defined by dividing the RMSE by the mean of the TRUC observations. NRMSE is then defined as

$$NRMSE = \frac{RMSE}{\overline{y}}$$

The mean value from the TRUC concentrations was used to normalize by, so that there could be a comparison of the SOG to what the "true" concentrations should be. The focus of this analysis will be on how the NRMSE values compare within the fourteen releases. If the NRMSE values are similar between releases on the same release day, then the errors observed could be attributed to the location of the source and impaction traps. If the NRMSE values differ between releases, the errors could be attributed to the individual release conditions.

For these comparison plots, there is a 10^{-10} threshold for the SOG concentrations. This was determined solely to visualize the data, but there were multiple points that fell below this threshold, up to values of 10^{-100}. If the TRUC impaction traps did not collect any particles, the SOG required a non-zero concentration to complete the nonlinear least-squared-error optimization. Those values were removed from the comparisons as well and are not included in the R^2 or NRMSE calculations.

It is also important to note why several concentration points in TRUC and SOG do not match perfectly. Some impaction traps did not collect any particles. However, the SOG predicted a concentration value for those locations instead of reflecting a "0" concentration. Also, there are some impaction traps that are upwind of the source that are not represented in the SOG concentrations. This is because the Gaussian plume model does not account for concentrations upwind of the source. Any impaction traps that collected particles upwind of the mean wind during TRUC will not be represented by the SOG. The R^2 and NRMSE calculations also do not consider particles in the upwind direction.

3.2.1 June 19th, "Ross Intersection"

3.2.1.1 Releases 2 and 3

Higher concentrations are observed from the TRUC observations than from the SOG concentrations calculated for most points, as seen in Figure 3.2a. Each blue point in the comparison figures represents one of the fifty impaction trap locations during TRUC. While the points should lie on the 'perfect' 1:1 black line, most points fall below it, noting that the SOG underestimates the concentration values compared to the TRUC observations. Concentrations that are closer to the source typically have higher values, where lower concentrations values are further away from the source. For release 2, the closest five points to the source either agree very well between TRUC and SOG or are within a factor of 10 different. As the concentrations decrease
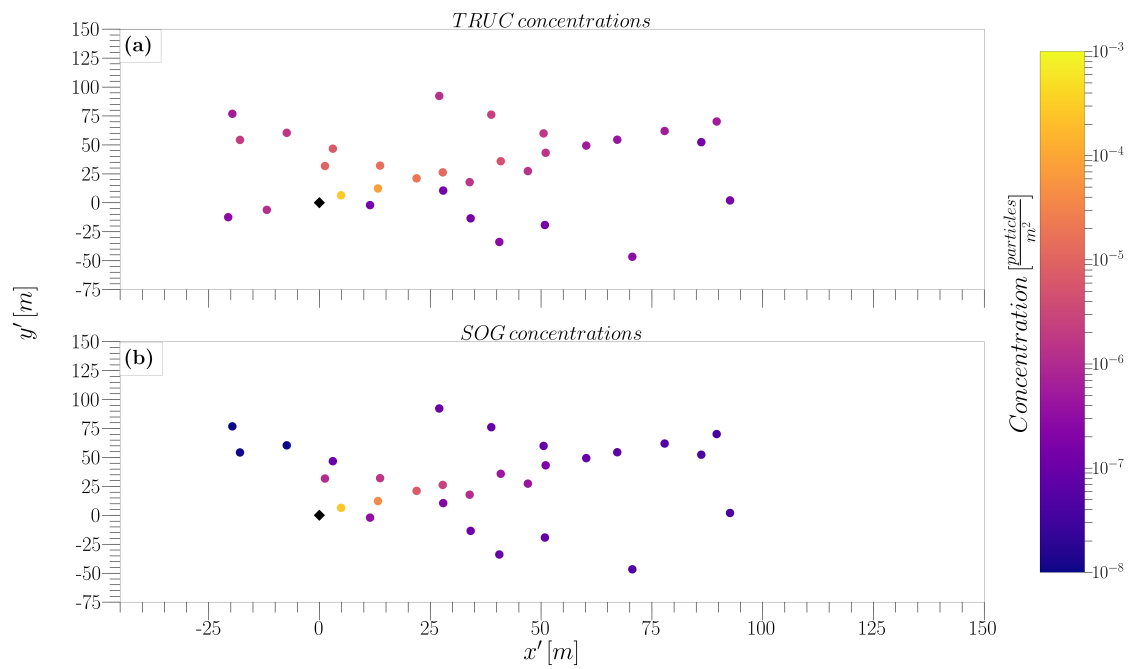
Figure 3.1: Concentration values for release 2 at each impaction trap for (a) actual TRUC concentrations and (b) SOG concentrations. The black diamond represents the source location (0,0), where the x' and y' values are distance from the source.
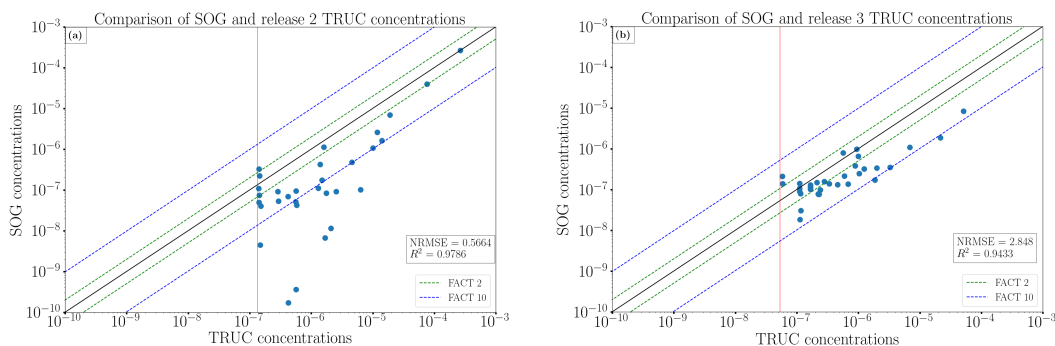
Figure 3.2: Comparison of TRUC concentrations observed to the predicted SOG concentrations for June 19th, releases 2 and 3. The black line represents the 1:1 line for goodness-of-fit. The green line represents a difference of SOG from TRUC by a factor of 2, while the blue line represents a factor of 10. The red line in each figure represents the minimum quantifiable concentration from TRUC (i.e. the concentration if one microsphere was captured between both rods), which varies per release.

in value, the SOG concentrations predicted are much smaller than what was observed with TRUC. The R^2 value for this release does show high agreement between the two concentrations, but many values vary by a factor of 10 or more. The NRMSE is small, meaning that there is very little unexplained error between TRUC and SOG. Visually from Figure 3.2a, this does not agree with the statistics calculated for this release, since there are many points that differ by several factors. This discrepancy will be discussed further in Section 3.2.5.

One hour later on the same day, release 3 began. The source and impaction traps locations did not change from release 2. Similarly, the highest concentrations are observed close to the source, which was also captured by the SOG (Figure 3.2b). Concentrations around 10^{-5} were observed along E 51st (see Figure 2.4), showing again decreasing concentrations as the distance from the source and along the mean wind direction increases. The R^2 value is slightly lower for release 3, comparatively,

but has a much larger NRMSE. This also does not visually agree with Figure 3.2b, but will be discussed and compared to the other releases in Section 3.2.5. The observed concentrations close to the source are also being underpredicted by the SOG by a factor of 10. Observed concentrations farther from the source agree more so, by a factor of 2 instead or some exactly lie on the 1:1 line.

During this release, the concentrations observed during release 3 are lower than the concentrations observed at similar locations during release 2. The plume for release 3 may not have spread along E 51st as much as release 2, but spread closer to the Ross St. intersection and dispersed where observations were not collected (i.e. no impaction traps).

3.2.1.2 Contours for Release 2 and Release 3

After verifying that SOG can produce reasonable concentration values at the TRUC locations, the SOG was then used as an interpolant across the entire TRUC sampler locations for June 19th (Figure 3.3). The SOG contours for Release 2 do capture the decreasing concentration values as the distance increases from the source (Figure 3.3a). The exact concentration value is where the SOG does not succeed. The SOG contours predict much lower concentration values close to the source than what was observed from TRUC. The highest concentration value is in the 10^{-4} range, but the SOG contour is about 10^{-5}. The SOG does not capture the correct magnitude of the concentrations anywhere, but does worse closer to the source. Several impaction traps are not captured by the SOG at all. The SOG captures the impaction traps in the contours that are close to the mean wind direction.

The contours for release 3 look completely different than the contours from release 2, despite the release times only varying by an hour for the same day. The wind angle for release 3 varied by about 5°, but observed slower wind speeds at 1.5 meters. The SOG contours in Figure 3.3b are similar to the contours for release 2 though, as the

release 3 contours underpredict the concentrations observed very close to the source. As the distance from the source increases in the x' direction, the SOG contours are then overpredicting the observed concentrations. The shape of the superimposed Gaussian plumes is evident in the contours for release 3, with an artifical "kinking" between them. This may be due to the SOG attempting to predict channeling of the plume down both streets (E 51st and Ross St., see Figure 2.4), especially since the wind angle during release 3 was more parallel to E 51st than the wind angle during release 2.

The difference between the contours could be explained by the fact that release 3 had more TRUC concentrations captured at the impaction traps. This may be due to channeling during release 3 that did not occur during release 2, due to the mean wind direction shift between the two releases. With a wind shift to the west, the plume from release 3 could channel moreso down Ross St. than the plume from release 2. This could also explain why SOG overestimated several concentrations close to the source. The plume could have spread further down E 51st Avenue and then channeled down the alleyway to the east. This could also possibly explain the large difference between the NRMSE between releases 2 and 3.

3.2.2   June 22nd, "Sherbrooke-Ross Intersection"

3.2.2.1   Releases 4A, 4B, 5A, and 5B

June 22nd must be analyzed separately from June 19th because of the new source location and impaction trap placement throughout the neighborhood. Releases 4A and 5A discharged purple microspheres, while releases 4B and 5B used the yellow/green microspheres. The first release of the day, 4A, also illustrates a similar trend that was observed for the releases on June 19th. The highest concentration observed was the closest impaction trap to the source, which is also predicted by SOG (Figure 3.4a). However, SOG still underestimates most of the concentration

Figure 3.3: SOG contours plotted with TRUC concentration points for each impaction trap for June 19th, releases 2 and 3. The mean wind angle is represented by the black arrow, which is below the mean wind speed ($\overline{u}$).

values, especially close to the source. The highest concentrations are underpredicted by almost a factor of 10, but most SOG concentrations are off by a factor of 2. Differently from June 19th, the SOG concentrations for release 4A agrees much better with the TRUC concentrations, but has a high NRMSE. This NRMSE for release 4A is similar in value to the NRMSE from release 3. The R^2 value is also slightly lower than releases 2 and 3, but visually, the concentrations have high agreement.

Release 4B, having started several minutes after 4A ended, shows similarities to the previous release. The SOG concentration predicted for the closest impaction trap to the source is less than the observed concentration. Higher concentration values were observed almost everywhere for release 4B, compared to release 4A, which is also evident from Figure 3.4b. The R^2 value is slightly higher for release 4B and also has a slightly lower NRMSE, meaning the SOG concentrations agree more with observations for release 4B than for 4A. However, the SOG is still underestimating most of the concentration values observed during TRUC.
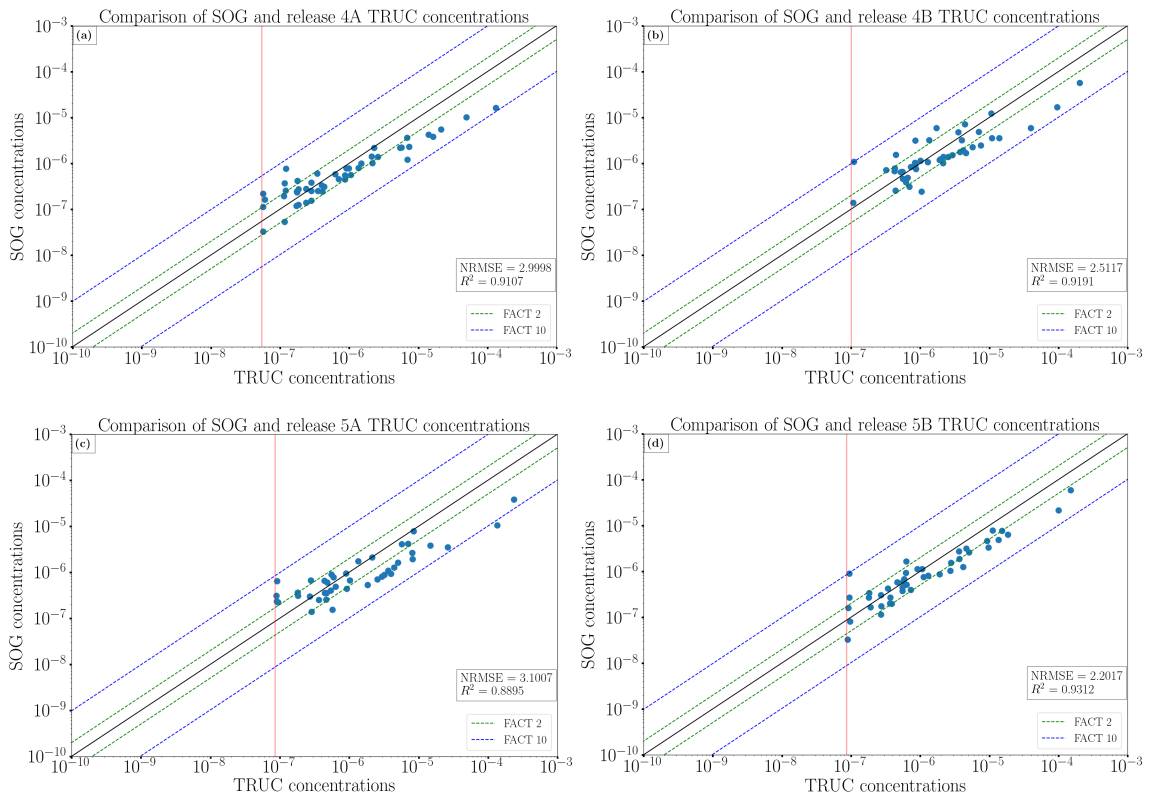
Figure 3.4: Same as Figure 3.2, but for June 22nd, releases 4A, 4B, 5A, and 5B.

Release 5A occurred an hour after release 4B. The TRUC concentration values from 5A are observed to be higher than the SOG concentration values close to the source. The highest concentration value for this release is captured in the SOG, but does not capture the magnitude of this point nor the observed concentrations surrounding it. Farther away from the source, the concentrations again decrease as distance in the x' direction increases. While some of the concentrations further from the source are perfect on the 1:1 line, the R^2 and NRMSE for this release are the worst of all four releases for June 22nd (Figure 3.4c). This NRMSE value does agree with the previous two releases though, which means that the location of the source at the intersection could be a contributing factor to the errors observed. The SOG is again underestimating the observed concentrations by between a factor of 2 and 10.

The last of the releases on June 22nd was Release 5B. The highest concentration observed was correctly calculated by the SOG, but was still underestimated. The comparison of the TRUC and SOG concentrations matches better than release 4A (Figure 3.4d). The blue points are much closer to the 1:1 line of agreement, with a few lining up perfectly. The higher concentration values (closer to the source) agree better than previous releases, which is visible in concentration plots. The SOG concentrations do not vary more than by a factor of 2 for most locations. The higher R^2 emphasizes better agreement of SOG with TRUC, as well as the lower NRMSE. Again, the NRMSE for all four releases on June 22nd shows that the error may be high, but there is consistency for the specific location.

3.2.2.2 Contours for Releases 4A, 4B, 5A, and 5B

The SOG contours for release 4A encompass all of the TRUC impaction trap locations, unlike the other three releases on the 22nd. The points outside of the contours are not captured, due to the upwind concentrations not being included in Gaussian plume model. Concentrations in the upper left corners should be captured by the

SOG, but are not for releases 4B, 5A, and 5B. For all releases, the contours decrease in concentration as the x' distance increases, showing that SOG does well capturing the typical decaying behavior of plume concentrations. Concentration values further from the source sometimes align with the SOG contours perfectly, as seen in 3.5a,b. The SOG contours for release 4A capture all of the TRUC observations, making it the best fit between all four releases on June 22nd.

The SOG contours, like the concentration values in Section 3.2.2.1, sometimes underestimate the far source concentrations, evident in 3.5c,d. Release 5B contours do capture almost all of the TRUC observations, except for the one point in the positive y' direction. This may be because the SOG considers the mean wind direction and does not account for channelling that occurred passed the intersection of E 51st Ave. and Ross St.

Similar to release 3, the SOG contours for releases 4B and 5B show an artifical "kink", which is a result of the SOG using two orthogonally-oriented Gaussian plumes. This may also be because SOG is trying to model channeling along both streets.

3.2.3   June 27th, "In-between Sherbrooke"

3.2.3.1   Releases 6A, 6B, 7A, and 7B

The source location for June 27th was moved to Sherbrooke St., between two intersections. All of the closest impaction traps for these releases observed a "splitting" of the maximum concentration between two impaction traps. The TRUC observations from Release 6A show the highest concentration to the left of the source location, but many observations of elevated concentrations in the -x' direction. The SOG does capture the highest concentration in the +x' direction, but has significantly lower concentrations estimated for close to the source impaction traps in the -x' direction. Some concentrations far from the source are more closely estimated by SOG in the +x' direction. While some concentrations match exactly on the 1:1 line far from
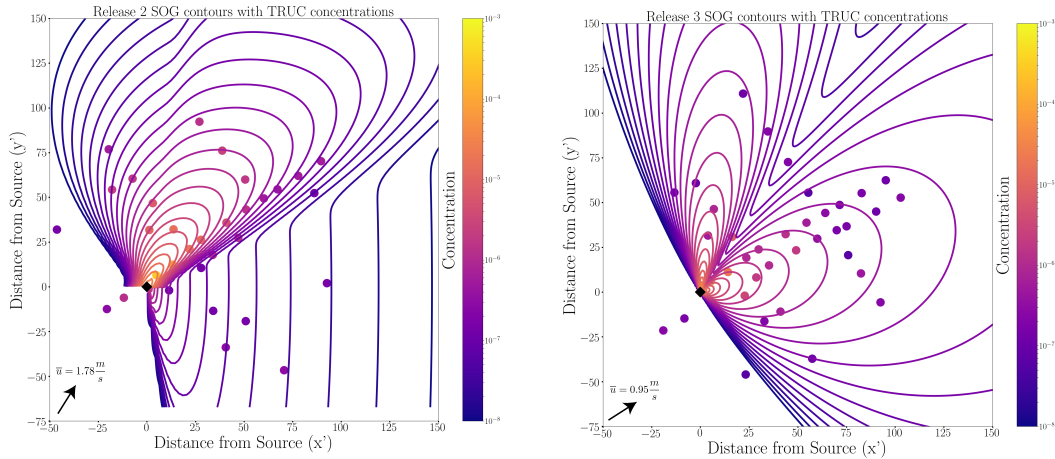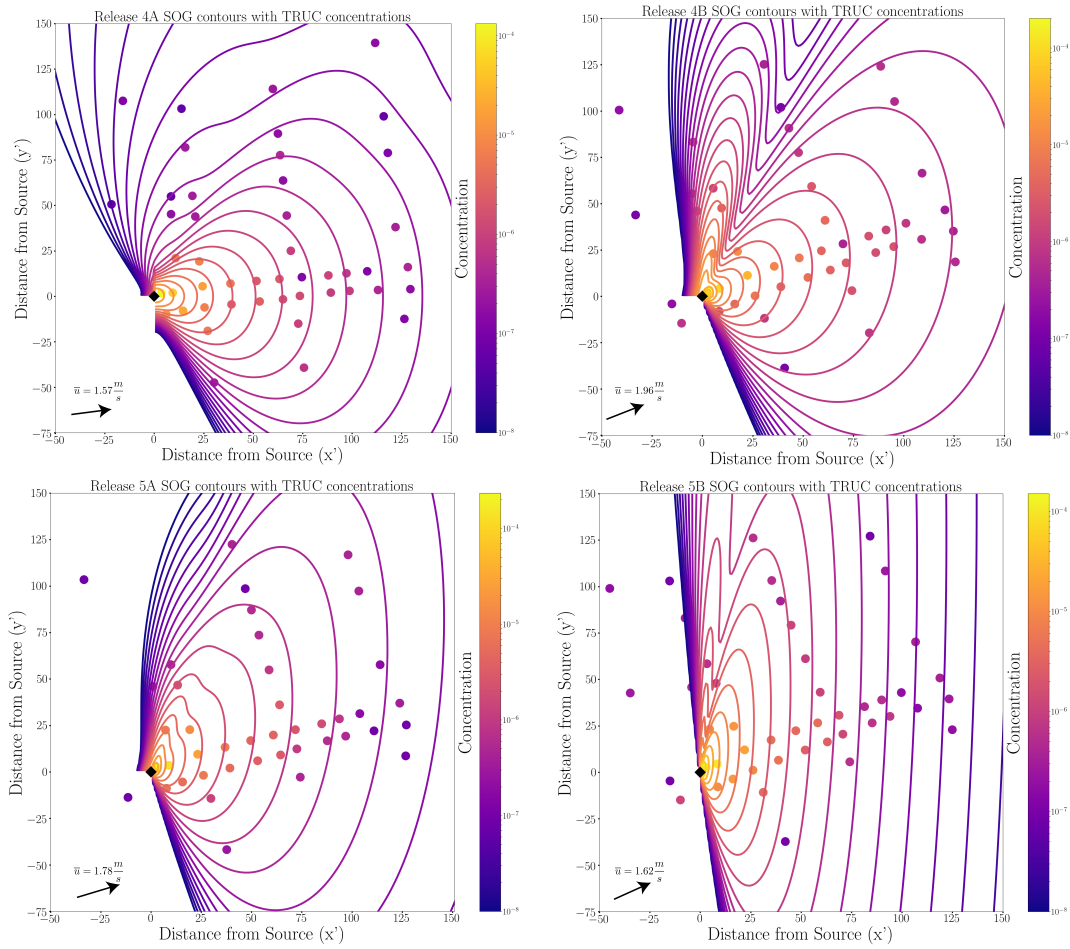
Figure 3.5: SOG contours plotted with TRUC concentration points for each impaction trap for June 22nd, releases 4A, 4B, 5A, and 5B. The mean wind angle is represented by the black arrow, which is below the mean wind speed ($\overline{u}$).
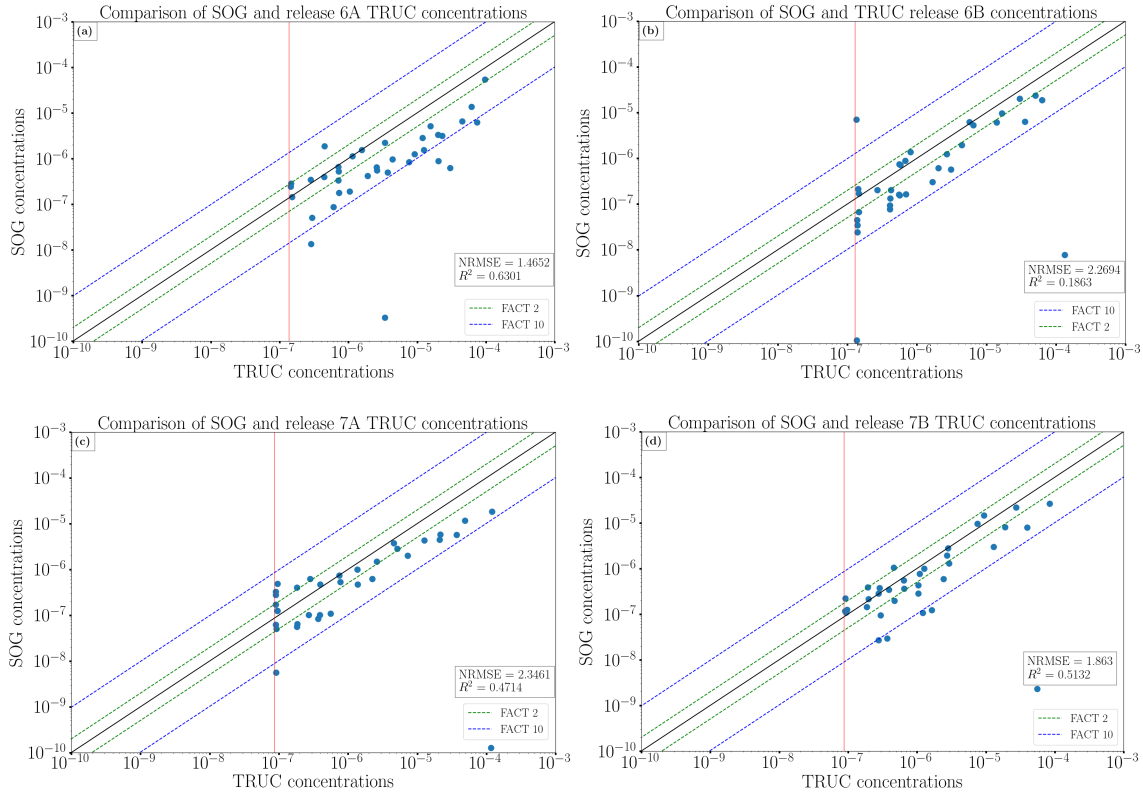
Figure 3.6: Same as Figure 3.2, but for June 27th, releases 6A, 6B, 7A, and 7B.

the source, the R^2 shows the large disagreement that SOG has from TRUC, missing TRUC concentrations by a factor of 10 or more (Figure 3.6a). The NRMSE is lower than the ones observed from June 22nd, but looks similar to spread of release 2 that also had a lower NRMSE.

Several minutes later, release 6B was started and yielded a slightly different plume. While release 6B had similar concentrations close to source like release 6A, the concentrations decreased faster in the +y' direction. The major difference between the SOG and TRUC concentrations is the highest concentration in the -x' direction being missed entirely by the SOG. The SOG does not estimate the plume "splitting" and therefore is off by several orders of magnitude, which is also why the R^2 is so low and NRMSE so high (Figure 3.6b). The NRMSE for release 6B is similar to the

ones observed from June 22nd, but comparison to the other releases for June 27th is important for further analysis.

Another feature that SOG is actually drastically overestimating is the concentration close to the source. An impaction trap in the -x' direction did not collect many particles (resulting in a lower concentration), but the SOG estimated the concentration to be much higher. This does show that while SOG is not capturing the exact locations of higher concentrations close to the source, it is interpolating to the general trend of high concentrations close to the source and lower concentrations farther from the source.

Release 7A and 7B occurred an hour later and also result in a different plume than the previous releases that day. Release 7A had two high concentrations observed to the north and south of the source in a diverging way. The SOG again underestimates the concentrations close to the source, completely missing the location to the south by several orders of magnitude. The underestimation is so low (10^{-10}) that it is almost not seen on Figure 3.6c. While SOG drastically misses the concentration close to the source, it does one point correctly far from the source, lining up exactly on the 1:1 line. The under-prediction of the largest concentration magnitude observed during TRUC explains why the R^2 value for this release is smaller. The other points are heavily underpredicted by SOG by no more than a factor of 10. Farther from the source, concentrations are being overpredicted by SOG. The NRMSE for this release is similar to release 6B, as well as the ones observed from June 22nd.

Release 7B was similar to release 7A with its observations and SOG missing the highest concentration close to the source. Unlike release 7A though, more impaction traps collected particles for observed concentrations about 75 meters from the source in the +y' direction. The alleyway about 100 meters from the source has both observed concentrations and SOG concentrations that are close in magnitude, highlighting that SOG does better far from the source during this release. The R^2 for this

release is higher than release 6B and 7A, due to several more SOG concentrations are within a factor of 2 from the TRUC concentrations (Figure 3.6d). Some far source SOG concentrations lie on the 1:1 line, while others are off by over a factor of 10, which contributes to the R^2 value only being 0.5132. The NRMSE for release 7B is between the values observed from the three previous releases. The similarity of the four NRMSE for June 27th is also an indication that the error observed during this release day could be explained by the instrument configuration.

3.2.3.2 Contours for Releases 6A, 6B, 7A, and 7B

For all four releases on June 27th, each one has a distinct plume shape. SOG contours for release 6A encompass all of the TRUC concentration points, seen in Figure 3.7a. The contours do focus higher concentrations close to the source, with the highest TRUC concentration intersecting with a SOG contour. As the contours go out in the +y' direction, the contours decreased in concentrations, but are underestimating the concentrations. Concentrations in the +x',+y' direction do match the contours, but are again underestimated. One of the closest concentrations to the source is not captured because it is upwind of the source, something that is not accounted for in the Gaussian plume models. There is a central highest concentration contour to the left of the source (in the +x' direction), but there is no observation to verify its accuracy. Since the SOG is an interpolant, the contours will be predicted for other locations, even for locations without observations.

The contours interpolated for release 6B have a completely different shape to the ones for release 6A. The SOG interpolates very low concentrations close to the source in the +x',-y' direction, which incorrectly characterizes the highest concentration observed (Figure 3.7b). Some of the higher observed concentrations close to the source in the -x',+y' directions are correctly contoured by the SOG. The concentrations in the +y' direction in particular are captured well in magnitude close and farther from

the source. The shift in contours near 0 in the y' direction and in the +x' direction is from the SOG trying to capture the points in the +x' direction. The points farther from the source in the +x' direction are even captured well. The largest error for the contours of release 6B is the characterization of the highest observed concentration in the +x',-y' direction. Discussed in Section 3.2.3.1, this error may be due to the SOG struggling to characterize channeling behind the source location.

Releases 7A and 7B have completely different plume shapes from the 6A and 6B SOG contours. The contours for release 7A completely miss the highest concentration in the +x',-y' direction, prematurely cutting all contours off before intersecting it (Figure 3.7c). The higher concentration values that are within the SOG contours are slightly underestimated. In the mid to far field of the source, the contours do well predicting the concentration values for the TRUC impaction trap locations. The contours also miss a few lower concentration observations that should be considered (i.e. not in the upwind quadrant). This plume shape looks like the orthogonal Gaussian plume distributions, unlike the shapes for releases 6A and 6B. The lobing of the contours is an artifact from the SOG as it uses the mean wind speed to interpolate the plume.

The plume shape interpolated by the SOG contours for release 7B also looks different than the other three releases. Similarly to release 7A though, the SOG contours completely miss one of the highest concentrations, with only the lowest contour barely intersecting it (Figure 3.7d). The other higher concentration points are well-contoured by the SOG, with similar colors overlapping to the point where they are not visible close to the source. This predicted plume also captures mid to far field concentrations well. The shape for this release is different than release 7A, possibly due to the wind angle shifting three degrees, which would allow the plume spread more perpendicular to E 51st Ave.

Figure 3.7: SOG contours plotted with TRUC concentration points for each impaction trap for June 27th, releases 6A, 6B, 7A, and 7B. The mean wind angle is represented by the black arrow, which is below the mean wind speed ($\overline{u}$).

3.2.4   June 29th, "Along Sherbrooke"

3.2.4.1   Release 8A, 8B, 9A, and 9B

The first release of June 29th, release 8A, has again moved the source location and all of the impaction traps to align more with Sherbrooke St. The TRUC concentrations have the highest concentration very close to the source and decreases in the +y' direction, along Sherbrooke. The SOG concentrations underpredict the highest observed concentration close to the source. Concentrations along the -x',+y' direction and along the alleyway south of the source are also underpredicted by SOG. This underestimation is also evident in Figure 3.8a, with most blue points below the 1:1 line. The highest concentrations are off by almost a factor of 10, but other concentrations farther from the source are off by a factor of 2. The R^2 for this release was higher than the previous day, meaning that the variance of values observed is close to the variance of the predicted concentrations. The NRMSE is similar to the NRMSE values from releases 3, 6B, 7A, and all of the releases from June 22nd.

Concentrations close to the source for release 8B were lower than the other releases that day, which explains the relatively lower concentrations observed across the whole domain. The SOG concentrations capture a similar trend of highest concentrations close to the source and decaying with distance. The number of impaction traps that have observed concentrations increased from the previous release, showing more of the plume spreading throughout the release. The R^2 value is lower than release 8A, but the NRMSE is also lower. The range of concentration values is better represented by release 8A, but the error between the observed and predicted values is smaller for release 8B. Only a few concentrations close to the source are off by a factor of 2, while most of the concentrations are off by a factor of 10 or more. The comparison in concentrations further from the source for release 8B looks similar to the comparison figure for release 2. Since the NRMSE is also much lower than previous releases, this trend is important to note.
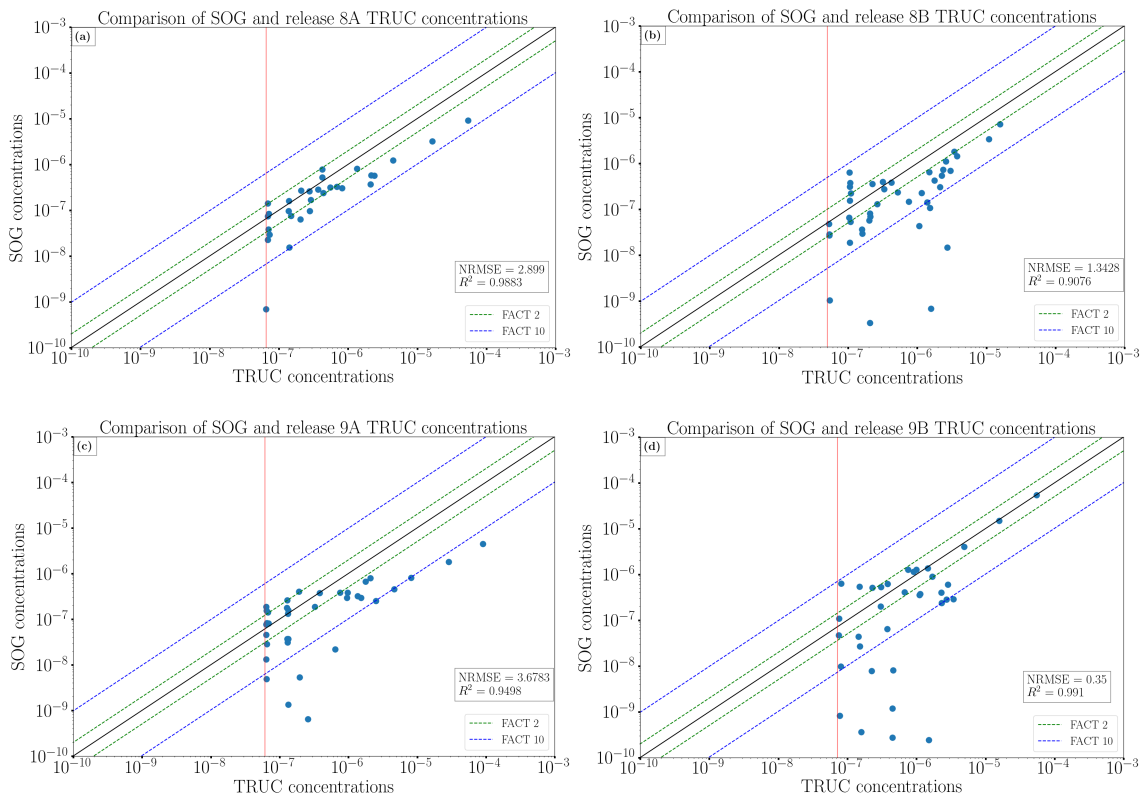
Figure 3.8: Same as Figure 3.2, but for June 29th, releases 8A, 8B, 9A, and 9B.

Release 9A shows another range of concentrations for the "Along Sherbrooke" releases. The TRUC concentrations demonstrate the highest concentration close to the source and decreasing values as the plume travelled along Sherbrooke in the +y' direction. The SOG concentrations greatly under-represent the concentrations for most of the impaction traps. Low concentrations were observed south of the source and along the alleyway in the +x' direction, while SOG does not capture elevated concentrations at the intersection. SOG does predict concentrations along the alleyways east of the source, as well as along Inverness St. While the R^2 value is again high, the NRMSE is also very high (Figure 3.8c). Many concentrations are off by a factor of 10 or greater from the SOG. While the NRMSE is similar to some of the previous releases, the comparison plot is not.

For this last release of June 29th, the TRUC and SOG concentrations for release 9B close to the source are very close or exactly correct. While the highest concentrations are correct, the concentrations start to differ quickly along Sherbrooke, about 50 meters from the source in the +y' direction on the same street. Concentrations from SOG agree with most of the observed concentrations about 50 meters from the source in the +x' direction, but begin to differ at the same +y' direction as Sherbrooke. Far from the source concentrations begin to differ from the TRUC concentrations dramatically, by a factor of 10 or more. From this 1:1 agreement with the highest concentration values, the R^2 is the highest out of every release during TRUC, as well as the lowest NRMSE (Figure 3.8d). This does not agree visually, with many SOG concentrations drastically different than what the TRUC concentrations observed. The statistics and comparison for release 9B are very similar to the ones from release 2.

3.2.4.2 Contours for Releases 8A, 8B, 9A, and 9B

Releases 8A, 8B, 9A, and 9B also all vary in plume shape, despite all occuring during the same afternoon. Release 8A underestimates the highest concentration close to the source, which can be seen behind the contours (Figure 3.9a). The SOG contours miss several points completely that should be included, but purposefully does not include the three that would be upwind of the source. Past 50 meters, the contours interpolate the observations well, correctly capturing the concentration magnitudes.

The contours for release 8B differ from release 8A in several ways. The highest observed concentrations are contoured almost correctly by the SOG close to the source, underestimating some of the points a little Figure 3.9b). The entire contour field underestimates the concentrations observed, except for the observations that are farther along Sherbrooke (and farther from the source). Several points are missed by the contours that should not be, meaning that the SOG plume is too narrow to capture all of the observations. The artifical "kinking" feature is present, with the larger and wider lobe in the direction of the mean wind.

The highest concentration for release 9A is significantly underestimated by the SOG, predicting several orders of magnitude lower than what was observed (Figure 3.9c). Similar to release 8B, the SOG misses several observed concentrations that should be included. The far field is where the contours best characterize the observed concentrations. Concentrations are underestimated everywhere else by the SOG. SOG might be missing these observations because of the channeling that occurred during this release along Sherbrooke St. Since the mean wind direction is not parallel to Sherbrooke, the SOG plume may not have properly predicted.

Release 9B has the worst predicted plume shape for both June 29th and the rest of the TRUC campaign days. However, the SOG plume contours do characterize the
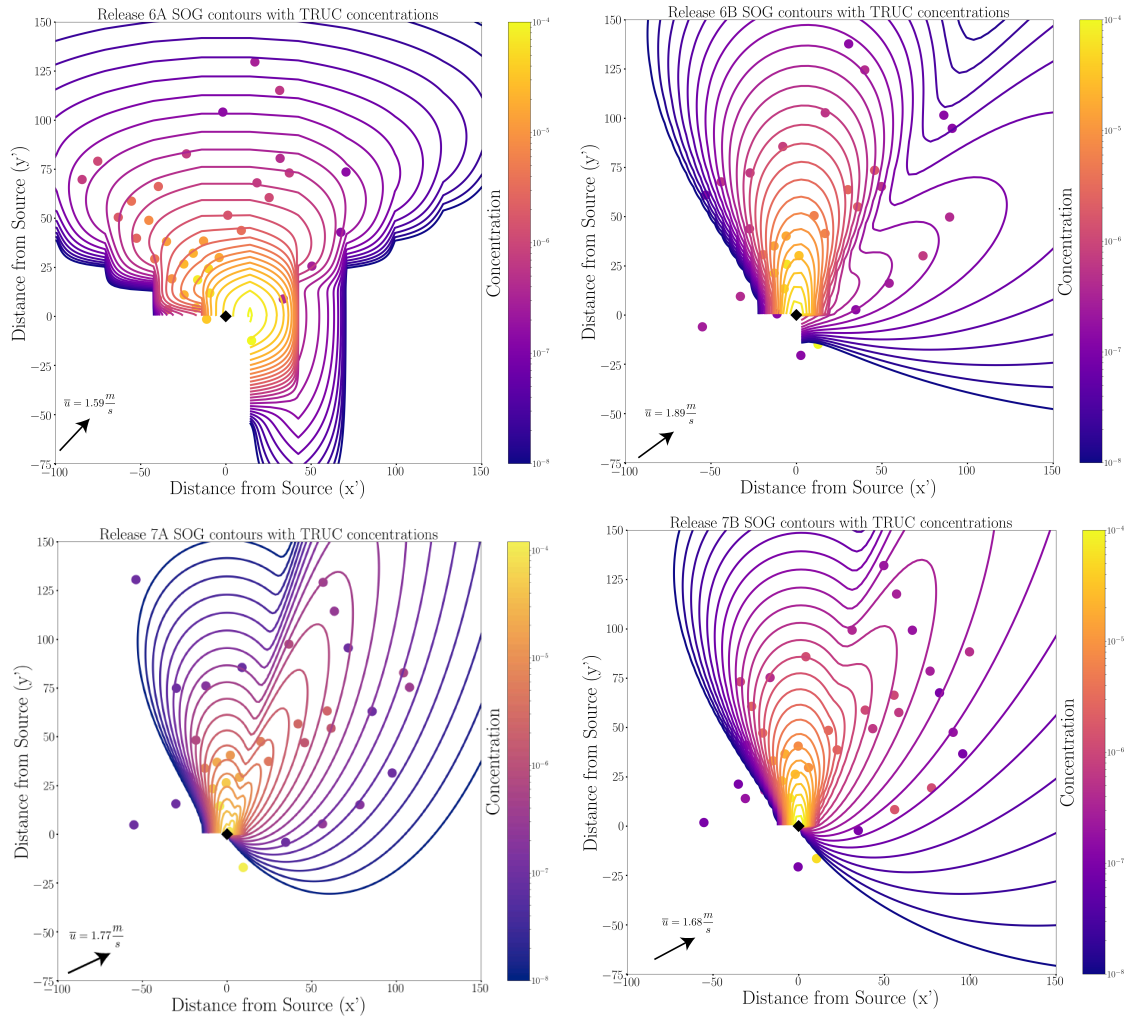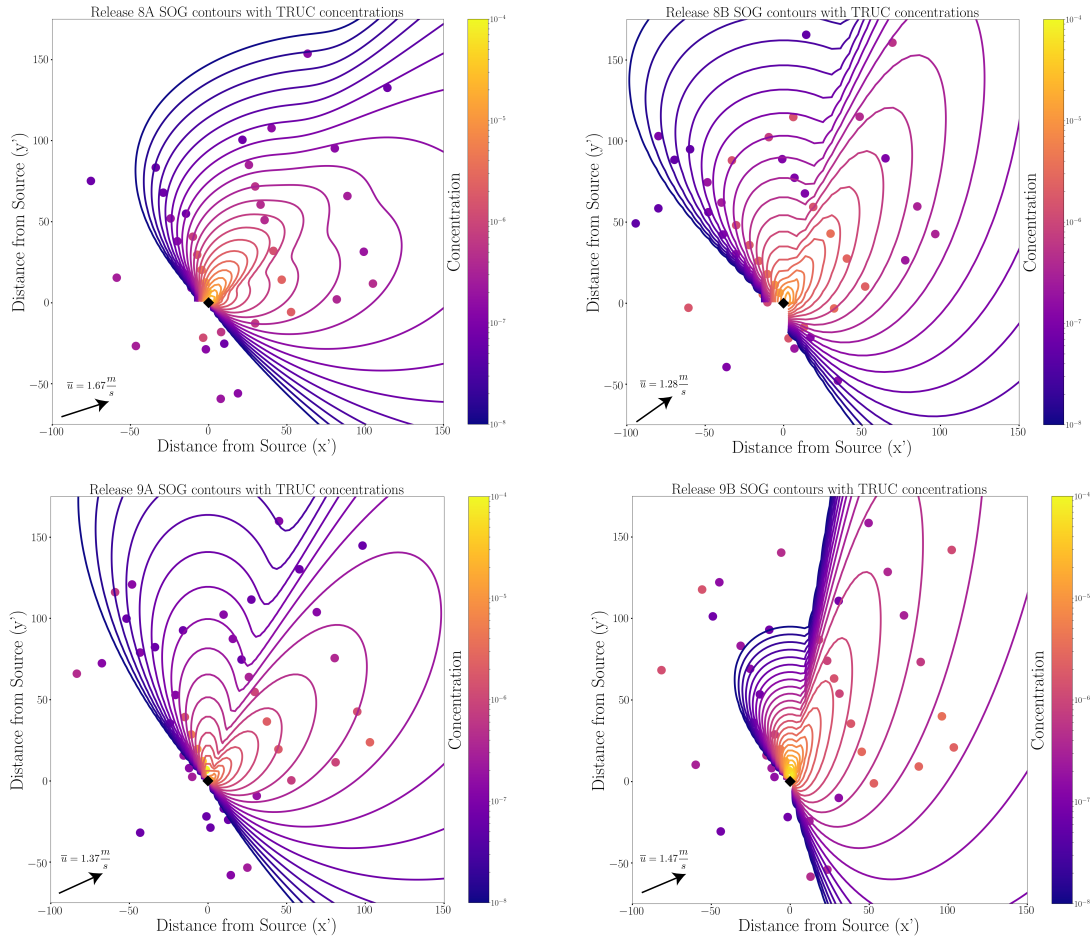
Figure 3.9: SOG contours plotted with TRUC concentration points for each impaction trap for June 29th, releases 8A, 8B, 9A, and 9B. The mean wind angle is represented by the black arrow, which is below the mean wind speed ($\overline{u}$).

highest concentration (close to the source) correctly, seen in Figure 3.9d. The predicted plume does also agree with several observed concentrations along Sherbrooke St. Concentrations also in the far field in the upper right quadrant of the TRUC location agree with the predicted concentration contours. Multiple observed concentrationas are not captured by the SOG contours, resulting in a poor representation of what the plume looked like during release 9B. The lobing feature is in the direction of the mean wind, which may also explain why that part of the plume is much larger and wider than the other lobe.

3.2.5   Discussion

3.2.5.1 R^2 and NRMSE discussion

All of the goodness of fit statistics between TRUC and SOG for each release is summarized in Table 3.2. Between all of the releases, the highest R^2 value with the lowest NRMSE came from comparison of the SOG and TRUC during release 9B. The Release 2 comparison also had a high R^2 between TRUC and SOG with a relatively low NRMSE. These two releases disagree the most between the other twelve releases. The low NRMSE and R^2 values do not visually agree with the comparison points. Release 2 was the first of the releases for TRUC, which could possibly explain why the statistics largely disagree with observations.

Several releases had concentrations that agreed well with the R^2 value, but had very large NRMSE. The lowest R^2 with a very large NRMSE was from the SOG concentration comparison for release 6B. It is important to note that while the R^2 values may be high, the consistently large NRMSE values are indicative that SOG is over- or under-predicting several concentrations of TRUC at specific locations. The agreement between releases for each release day, especially June 22nd and 27th, indicate that the errors are dependent and relative to the location of the source and instruments. June 29th is different, as releases 8A and 9A have similar NRMSE,

while 8B and 9B do not. While the SOG concentrations differ from the TRUC concentrations by many orders of magnitude, the fact that the concentrations are so small (i.e. 10^{-10}) may explain why the NRMSE is lower than the others. This could also explain the NRMSE for release 2.

3.2.5.2 Wind Direction Discussion

Flow in the cross-wind oriented street canyons was commonly channeled in the along-canyon direction with the direction keenly sensitive to small changes in the wind direction (Klein and Clark, 2007). This was evident throughout several releases during TRUC.

Comparatively to the concentrations observed during releases 2 and 3, release 4A shows concentration values observed passed the first and second intersections and in between the second and third intersections. The effect of channeling could be occurring here, especially since the concentrations show a distinct "split" of higher and lower concentration values at the northeast corner of the E 51st and alleyway intersection. The wind angle may explain the drastic change in observed concentration. The mean wind angle for the time frame during release 4A was 262.6°, which is parallel to E 51st Avenue. This differs from the mean wind angle observed during release 4B, which was 246.6°, a 16°difference. This wind shift to the southwest may have influenced the plume's behavior and forced it to flow down both Ross St. and the alleyway.

The SOG for releases 5A and 5B shows localized higher concentrations close to the source and around the E 51st and Ross intersection, as well as a generalized trend of channeling down the alleyway. TRUC observations show slight channeling down the near the E 51st and alleyway intersection, but the concentration values decrease quickly. Higher concentration values are also observed farther down 51st

Ave., approaching the intersection with Sherbrooke St. SOG also does not capture this trend, which may explain why the R^2 and NRMSE are worse.

The change in concentrations observed during TRUC, especially around the intersection of E 51st and Sherbrooke, is due to the change in mean wind direction between release 6A and 6B (see Table 3.1). The difference in wind angle is only 10°, but this more southwesterly wind then interacts with more of the home buildings within the neighborhood (see Figure 2.6). This would also inhibit the channeling effect that occurred during release 6A from occurring during release 6B. Similar channeling is seen down E 51st St., but not further in the -x',+y' directions down Sherbrooke.

During release 7B, both Sherbrooke and E 51st show evidence of channeling in the observations, which SOG predicts at a lesser magnitude. Another alleyway in the +y' direction has concentrations from TRUC, unlike during release 7A. Even channeling in the -x' direction is seen in the observations, but SOG does not capture the same order of magnitude.

Channeling of the plume is most evident down Sherbrooke St., but can also be seen along the alleyway oriented in the +x' direction for releases 8A and 8B. Elevated concentration values are also observed along with alleyway east of the source and along Inverness St. The SOG does estimate concentrations of similar magnitude along the other streets mentioned, but misses the intersection of Sherbrooke and the perpendicular alleyway. This is seen in Figure 3.8b, where a blue dot is observed to be 10^{-6}, but is predicted by SOG to be 10^{-8}.

Channeling during release 9A is also evident, especially along Sherbrooke in the +y' direction. The intersection of Sherbrooke and the southward alleyway did not observed higher concentrations, but further along the +x' direction does. This could be because the plume spread through the obstacles of trees and houses at a higher height than the impaction traps. More observations, especially at more than one height, would be necessary to confirm this possibility.

During release 9B, the mean wind direction was 247.1°. With this angle, the plume can spread down the southward alleyway and down to the north-south oriented alleyway and onto Inverness St. This wind angle also could explain why the west side of Sherbrooke (farther -x' direction) is predicted to have much lower concentrations than what was observed.

Given the complexity of the urban geometry, it is not expected for the SOG to be a perfect fit for the TRUC concentrations. The benefit of SOG is that now plume statistics can be calculated, which otherwise would not be possible from the TRUC observations alone.

Releases	R^2	NRMSE	% within FACT 2	% within FACT 10
2	0.9786	0.5664	19.4	64.5
3	0.9433	2.8480	38.2	94.1
4A	0.9107	2.9998	62.5	100
4B	0.9191	2.5117	54.6	100
5A	0.8895	3.1007	47.6	97.6
5B	0.9312	2.2017	70.5	100
6A	0.6301	1.4652	30.6	86.1
6B	0.1863	2.2694	26.5	91.2
7A	0.4714	2.3461	32.4	94.1
7B	0.5132	1.8630	51.4	85.7
8A	0.9883	2.8990	50.0	96.7
8B	0.9076	1.3428	28.6	85.7
9A	0.9498	3.6783	33.3	77.8
9B	0.9910	0.3500	40.0	77.1

Table 3.2: Summary of all R^2 and NRMSE values for each release, as well as the percentage of impaction traps that are within a factor of 2 and 10 of the 1:1 line

3.3 Observed Plume Behavior

3.3.1 Plume Moments

To better understand the turbulence within the TRUC domain, plume moments were calculated from the SOG meshgrid to further characterize the plumes. The moments were calculated using the same method as Miller et al. (2018). The first order moment is mean plume centerline, defined as $\mu_{y'}(x') = \frac{\int_{-\infty}^{\infty} y'\Pi(x',y')dy'}{\int_{-\infty}^{\infty}\Pi(x',y')dy'}$, describes how the center of the plume changes in the y' direction as a function of x' farther from the source. Plume spread from the centerline is the second order moment, defined as $\sigma_{y'}(x') = \left(\frac{\int_{-\infty}^{\infty} (y'-\mu_{y'})^2\Pi(x',y')dy'}{\int_{-\infty}^{\infty}\Pi(x',y')dy'} \right)^{\frac{1}{2}}$. Plume spread describes how the plume spreads laterally from that centerline in the x' direction.

Skewness, the third order moment, represents how symmetric the plume is, i.e. how does the symmetry change as the plume moves away from the source. Skewness is defined as $Sk_{y'}(x') = \frac{\int_{-\infty}^{\infty} (y'-\mu_{y'})^3\Pi(x',y')dy'}{\sigma_{y'}^3 \int_{-\infty}^{\infty}\Pi(x',y')dy'}$. The skewness of a Gaussian plume distribution is 0, which indicates perfect reflectional symmetry of the plume. The fourth order moment, kurtosis, is an even moment, so it is always positive. Kurotsis is defined as $K_{y'}(x') = \frac{\int_{-\infty}^{\infty} (y'-\mu_{y'})^4\Pi(x',y')dy'}{\sigma_{y'}^4 \int_{-\infty}^{\infty}\Pi(x',y')dy'}$. Kurtosis represents how the plume is weighted at the "tails" of a distribution. A Gaussian plume distrbution has a kurtosis of three. If the kurtosis > 3, the distribution has a large probability of extreme values or a heavier "tail"" distribution. If the kurtosis is < 3, there is a very low probability of "tails" in the distribution, having a narrower shape than the Gaussian distribution.

Each plume moment was examined for each release, broken down by the individual day, and then plotted as a function of the downwind distance in the x' direction.

3.3.1.1 Mean Plume Centerline

The mean plume centerline shows how the centerline varies in the lateral (y') direction downwind of the source (Figure 3.10). In a Gaussian plume model, the

plume centerline starts at the release point, which in this case would be from the source point (0,0). The plume centerline also would not deviate from the x' axis as it moves downstream. In the upper-left figure for June 19th, releases 2 and 3 show slight spreading of the plume centerline as the plume travels in the x' direction. While release 2 shows the plume centerline starting from the source, release 3 has the plume centerline starting at approximately 10 meters, but is asymptotic at 20 meters.

Releases 4A and 4B show a start point for the mean plume centerline at 20 and 75 meters, respectively, while releases 5A and 5B only are slightly off from the source location. Releases 4B and 5A however show a continuous and linear shift in the plume centerline, but releases 4A and 5B behave asymptotically to a constant value of about 100 meters in the x' direction. All of the releases from June 27th have slightly shifted source locations as well for the plume centerline, but releases 6A and 6B behave asymptotically. During releases 7A and 7B, the plume centerline begins to spread about 100 meters downwind. The only plume centerline that is close to the Gaussian plume centerline behavior is release 8B. Releases 8A, 9A, and 9B all show a constant spreading of the plume centerline.

Observations during the Mock Urban Setting Trial (MUST; Biltoft, 2001) in the Great Basin Desert of northwestern Utah noted that the presence of obstacles led to a lateral deflection in the mean plume centerline relative to the mean wind direction (Yee and Biltoft, 2004). Channelling of the mean wind flow within the obstacle arrays also influenced the lateral displacement of the plume. Philips et al. (2013) also suggests that the mean plume centerline can be offset from the source location, due to the local flow close to the source. The local flow details were observed to have a larger impact on the plume centerline trajectory than on the entire domain itself. While more literature is necessary to verify if this effect is valid for urban domains, the observations and LES could explain the mean plume centerline trends calculated by the SOG.
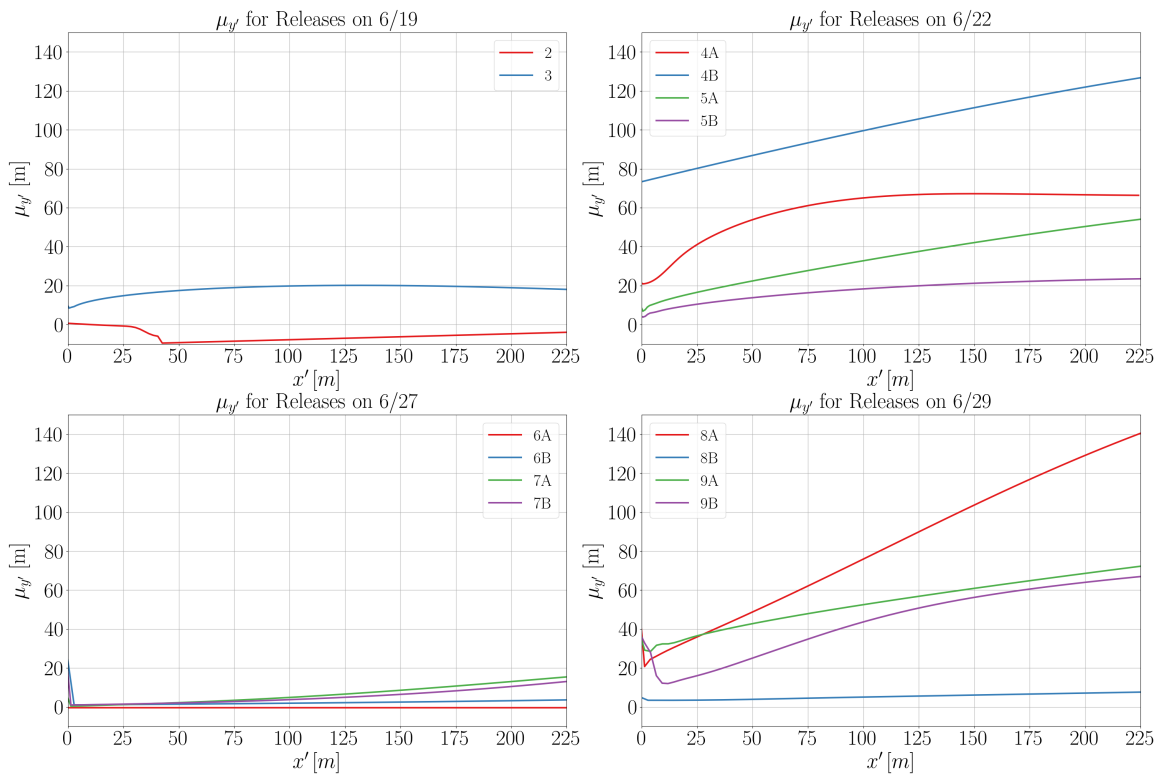
Figure 3.10: First order plume moment, mean plume centerline, for all four release days

3.3.1.2 Plume Spread

For a Gaussian plume distribution, the plume spread should begin at the source origin, like the mean plume centerline, and spread infinitely in space for σ_y and σ_z. For near-source modeling of complex canopies, an effective source size has been used to describe the offset of approximately 40 meters from the source to account for unsteady mixing of the plume at the source (e.g. McElroy and Pooler, 1968; Hanna and Baja, 2009; Franzese and Huq, 2011; Philips et al., 2013). Since the plume for the TRUC can only be evaluated in two dimensions, the plume spread, $\sigma_{y'}$, should be constantly observed to be increasing in the positive x' direction.

Releases 2 and 3 on June 19th show non-Gaussian plume spread behavior, as seen in the upper left panel in Figure 3.11. For release 2, the plume is predicted to narrow in spread at approximately 40 meters from the source and then slowing start to spread again as it moves downwind. The plume in release 3 shows a gradual spreading of the plume, but it starts to behave asymptotically to a constant value of about 100 meters from the source. The releases from June 22nd show similar plume spread behavior as it travels in the +x' direction. In the upper right panel of Figure 3.11, releases 4B, 5A, and 5B show slight spreading (similar to release 3), but then also begin to slowly approach asymptotic behavior. The plume during release 4A spreads in a linear way and has a larger effective source size than the other three releases. The plume spread for all four releases on June 27th spread linearly, with effective sources sizes much smaller than the other releases. On June 29th, the plume offset from urban effects was more prominent than the other TRUC campaign days, with the plume spread offset by 40-60 meters near the source. The plume from release 8B did not spread as much as the other plumes laterally, but does behave similarly and asymptotically further from the source.

Observations from TRUC for all of the releases, except for releases from June 27th, agree with previous literature. Plumes close to the source can be non-Gaussian
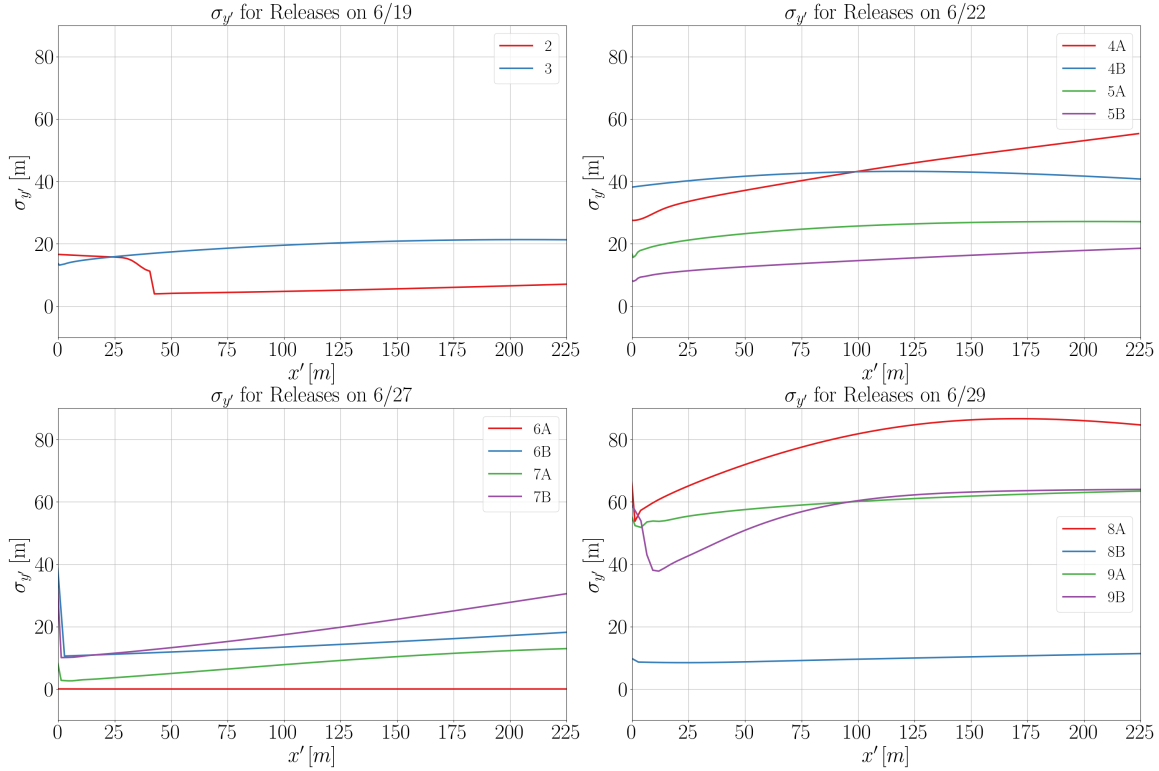
Figure 3.11: Second order plume moment, plume spread, for all four release days

and therefore laterally shifted from the source location, due to the plume shape being dominated by local building effects (Baechlin et al., 1992; Theurer, 1995). MacDonald et al. (1997) also observed increased lateral spread of the plume close to the source in experimental dense building arrays. The agreement of the plume spread from SOG with previous literature is promising for calculating plume moments with observations.

3.3.1.3   Skewness

For a Gaussian distribution, the skewness equals 0. A non-Gaussian (or positive) skewness is expected close to the source (e.g. Drivas and Shair, 1974; Jones, 1983; Yee et al., 1993), especially for urban experiments (e.g. Finn et al., 2010). These values are also consistent with other experiments that were conducted under unstable conditions (e.g. Mole and Jones, 1994). It is important to note that Drivas and

Shair (1974) included time-dependent measurements of skewness, while Yee et al. (1993) included the skewness of instantaneous concentration fluctuation. The other experiments listed, similar to TRUC, were time-averaged.

The skewness for each release during TRUC compared to downwind distance, x', is shown in Figure 3.12. Release 2 has a skewness that is unlike the other releases, with a slightly right-skewed behavior until about 40 meters. After this point, the skewness then slowly decays along the x' direction. Release 3 however has only a slightly right-skewed distribution, also approaching the black dotted line at 0, which is the skewness for a Gaussian distribution.

All of the releases during June 22nd have a nominally right-skewed distribution before decreasing in skewness. Releases 4A and 4B do cross over the "0" line, while the skewness for releases 5A and 5B approach the line, but do not intercept it.

The skewness distributions for June 27th have higher values of skewness close to the source than the other releases, except for release 6A. While the peak close to the source is similar for releases 6B, 7A, and 7B, the decaying behavior varies for each release. Release 7A is the only release that closely approaches the Gaussian skewness of 0. Release 6A has a left-skewed distribution, with a peak at -17 and becoming slightly less negative as the plume travels downstream.

The only explanation for the very negative skewness during release 6A is due to the SOG itself. The meshgrid required to produce the contours in Figure 3.7 is much larger spatially than the other release for June 27th. This different skewness may be due to the changed shape in the contours, which looks to be the combination of the two orthogonal Gaussian plumes. The "lobing" feature mentioned earlier is along the x' direction for 6B. Since this "lobing" is the SOG attempting to predict the channeling down the back alleyway, the resulting contour may be causing the left-skewed skewness.

Figure 3.12: Third order plume moment, skewness, for all four release days. The black dotted line represents the skewness of a Gaussian plume distribution, which equals 0.

The releases from June 29th show similar behavior to the releases from June 22nd. All releases have peaks in skewness close to the source and decay in the x' direction, but release 8B does not become asymptotic close to the 0 line. A distinct feature in the release 9B skewness is a peak at approximately 15 meters downstream, instead of very close to the source.

3.3.1.4 Kurtosis

Gaussian distributions have a kurtosis of 3, indicating an even distribution in the tails. A non-Gaussian kurtosis is also expected close to the source (Jones, 1983; Yee et al., 1993). In unstable conditions, very high kurtosis was observed to be

on the order of 100 (Mole and Jones, 1994). For JU03, the kurtosis was also non-Gaussian and on the order of 10 (Finn et al., 2010). A kurtosis > 3 indicates that the distribution is leptokurtic or "heavy-tailed", meaning there are more extreme values in the distribution. However, a kurtosis that is < 3 is platykurtic or "light-tailed", meaning there are fewer extreme values than a Gaussian distribution. Similar to skewness, some of the concentrations evaluated for other experiments used the distribution of concentration fluctuations (e.g. Finn et al., 2010), while others did not. This is important to consider when comparing kurtosis from TRUC.

For TRUC, several releases showed non-Gaussian behavior and are of similar magnitudes as previous studies (Figure 3.13). Some of the plumes do become platykurtic further downwind in the x' direction. Release 2 shows a dramatic change in kurtosis from values on the order of 10 to suddenly values much greater than 100 at about 50 meters downwind. Conversely, release 3 has kurtosis values similar to those observed in JU03 and decreases away from the source in the x' direction to become playtkurtic at around 30 meters. Kurtosis values for June 22nd also show similar behaviors starting from the source and travelling downsteam. Releases 4A and 4B do approach the Gaussian kurtosis of 3 and become non-Gaussian again at about 75 meters from the source.

Releases conducted on June 27th illustrate different behaviors from the previous two release days. The kurtosis values are very high, but similar to those observed from Mole and Jones (1994). These values though either barely approach Gaussian values or do not at all far from the source. The releases from June 29th have similar kurtosis values and behaviors to the ones from June 22nd. An interesting trend from release 8B shows a curve that does not appear to asymptote in the near or far field, while all three other releases do cross the kurtosis of 3 or come very close to it.

The higher non-Gaussian kurtosis values could indicate channeling of the plume, creating a narrower distribution close to the source and spreading slowly in the y'
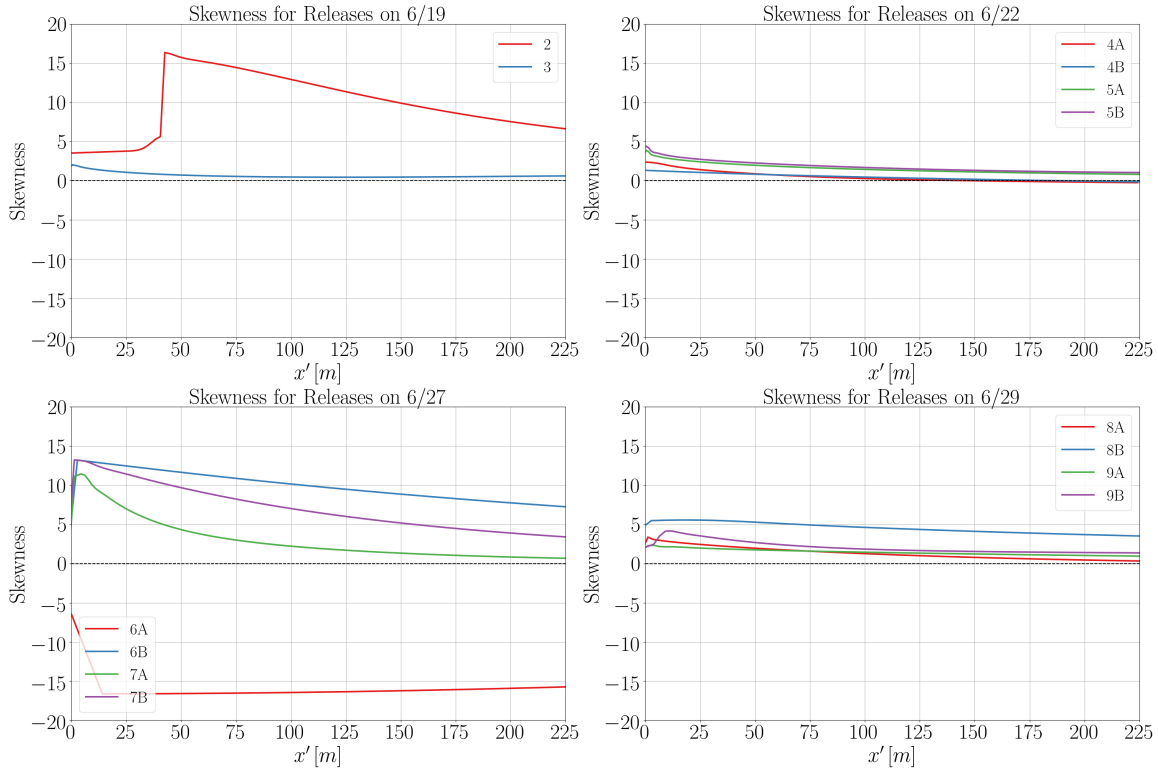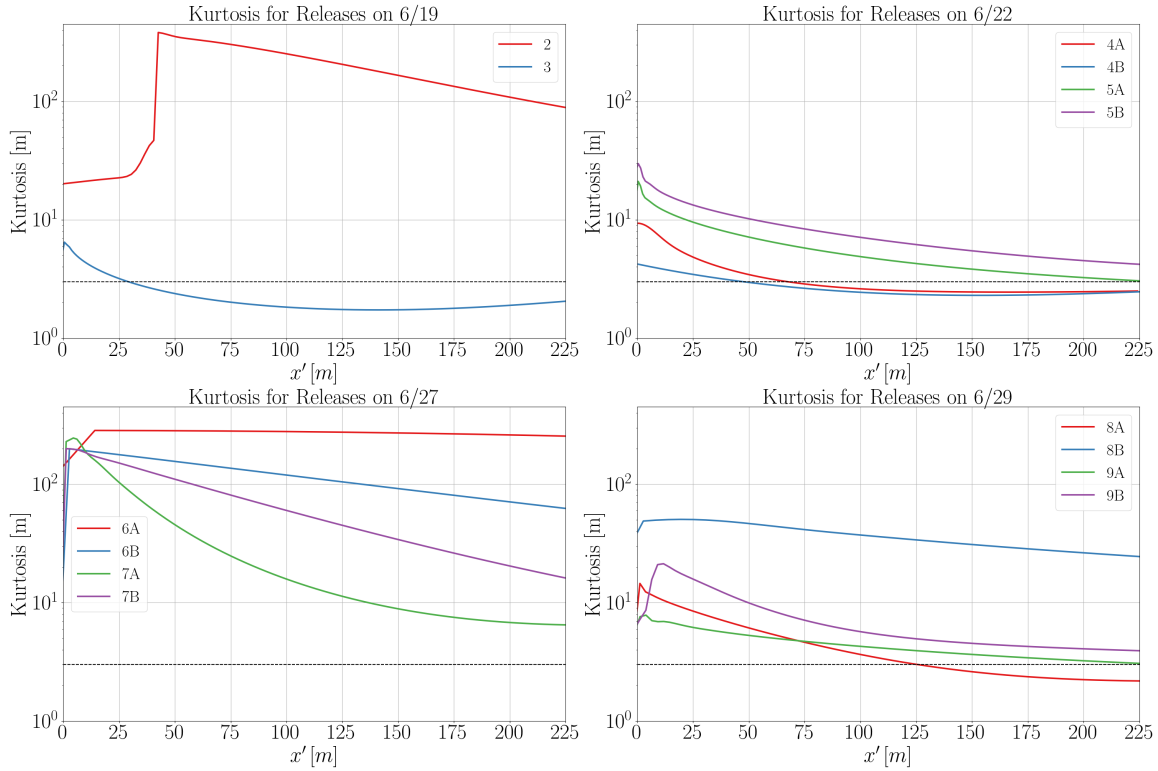
Figure 3.13: Fourth order plume moment, kurtosis, for all four release days. The black dotted line represents the kurtosis of a Gaussian distribution of 3.

direction as the plume travels away from the source in the x' direction. For example, the drastic change in kurtosis for release 2 could be because of the intersection that crosses E 51st Avenue about 50 meters in the +x' direction Figure 3.3. If the plume is channeling down the street and then is channeled down another, this could lead to a narrower plume after that point.

3.4 Influence of mean flow, turbulence, and urban geometry

3.4.1 Mean flow and turbulence effects on plume moments

To possibly determine what may impact the higher-order plume moments, several of the turbulence statistics were compared to the plume moments by examining select downwind x' locations. The turbulence variables examined were from the 3D sonic

mobile tower at 1.5 meters. The variables presented are the mean wind angle, mean wind speed, Monin-Obukhov stability (z/L) parameter, the mean wind variance, σ_u^2, and the horizontal velocity variance, σ_h (defined as $\sigma_h = \left[\sigma_u^2 + \sigma_v^2\right]^{\frac{1}{2}}$). The variance, σ_u^2, comes from the standard deviation of the computed u component of the observed anemometer wind.

The mean wind angle was first compared to the mean plume centerline ($\mu_{y'}$) for each release at several different locations downwind from the source (Figure 3.14). For every downwind distance, the deviation of the mean plume centerline is increasing for almost every release as the wind angle increases. As the wind angle shifts from the cross-wind direction of the street network to the along-wind direction, the mean plume centerline may begin to interact with more of the urban geometry and begin to diverge around them. The explanation for the orange point (release 4A) not increasing with increased wind angle may be because the wind will start to channel down the streets as the wind direction aligns with them.

Figure 3.15 shows the plume spread and mean wind angle behaving similarly to the mean plume centerline and wind angle comparison. As the wind angle starts to increase, the plume begins to spread further from the mean plume centerline downwind. Plume spread close to the source does not indicate this trend clearly, but points downstream at 100 and 200 meters do illustrate a more obvious increasing behavior. The possible interaction with residential homes or vegetation within the neighborhood may be causing the plume to spread.

When the third and fourth order moments were compared to mean wind angle, the relationship between mean wind angle with skewness or kurtosis is not a discernible one. The skewness does not seem to change in sign or behavior as wind angle increases (Figure 3.16). As the skewness becomes more Gaussian with downwind distance, the releases begin to approach the Gaussian skewness of 0, but this is not impacted by the wind angle either. While the kurtosis illustrates a different pattern compared to
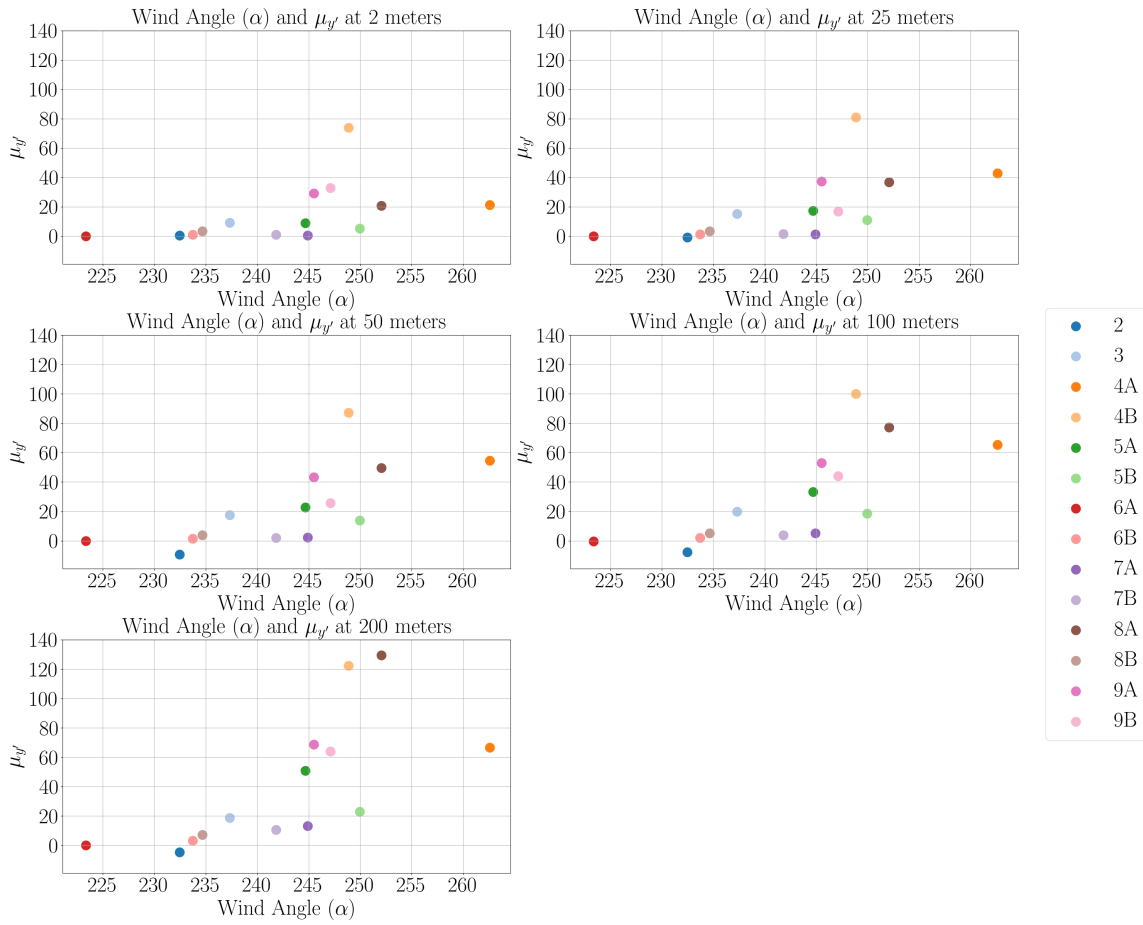
Figure 3.14: Mean wind angle compared to the mean plume centerline for each release at 2m, 25m, 50m, 100m, and 200m downwind of the source
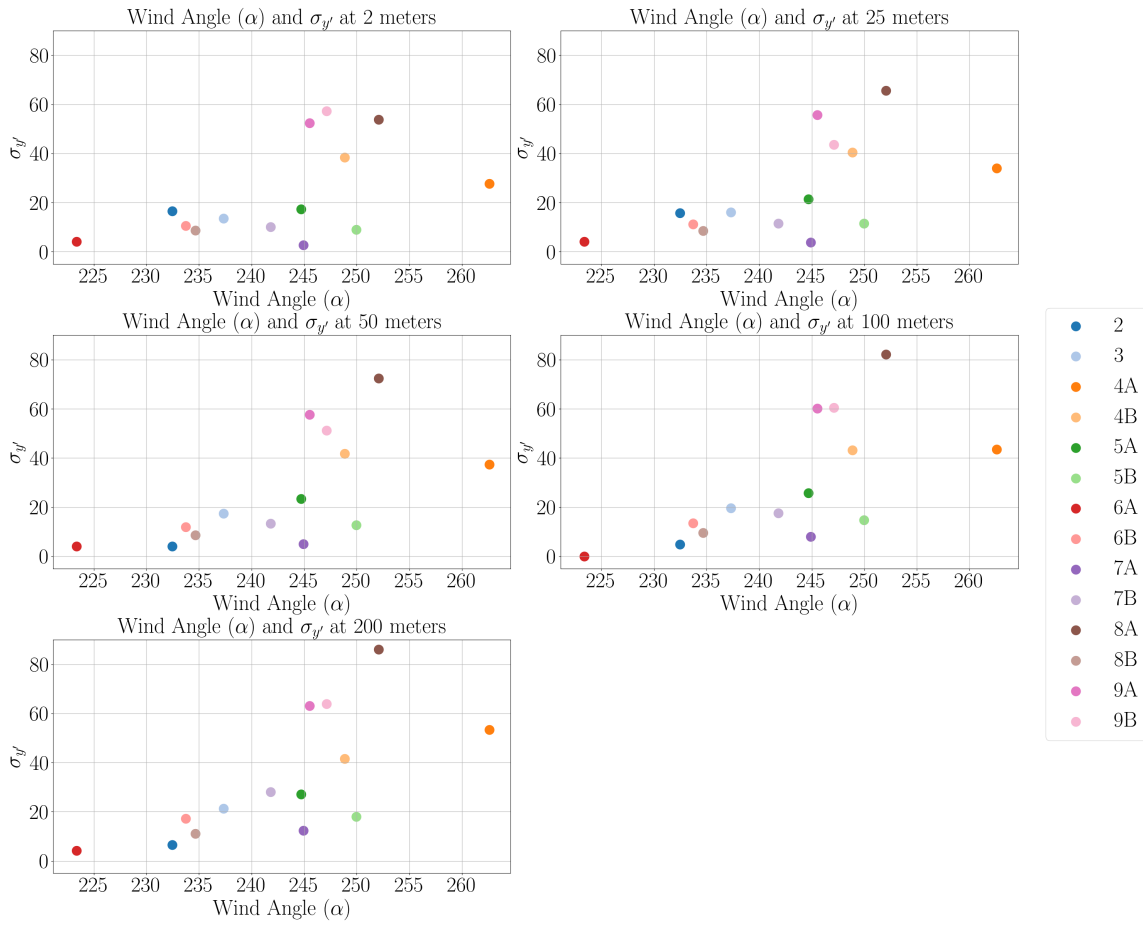
Figure 3.15: Mean wind angle compared to the plume spread for each release at 2m, 25m, 50m, 100m, and 200m downwind of the source
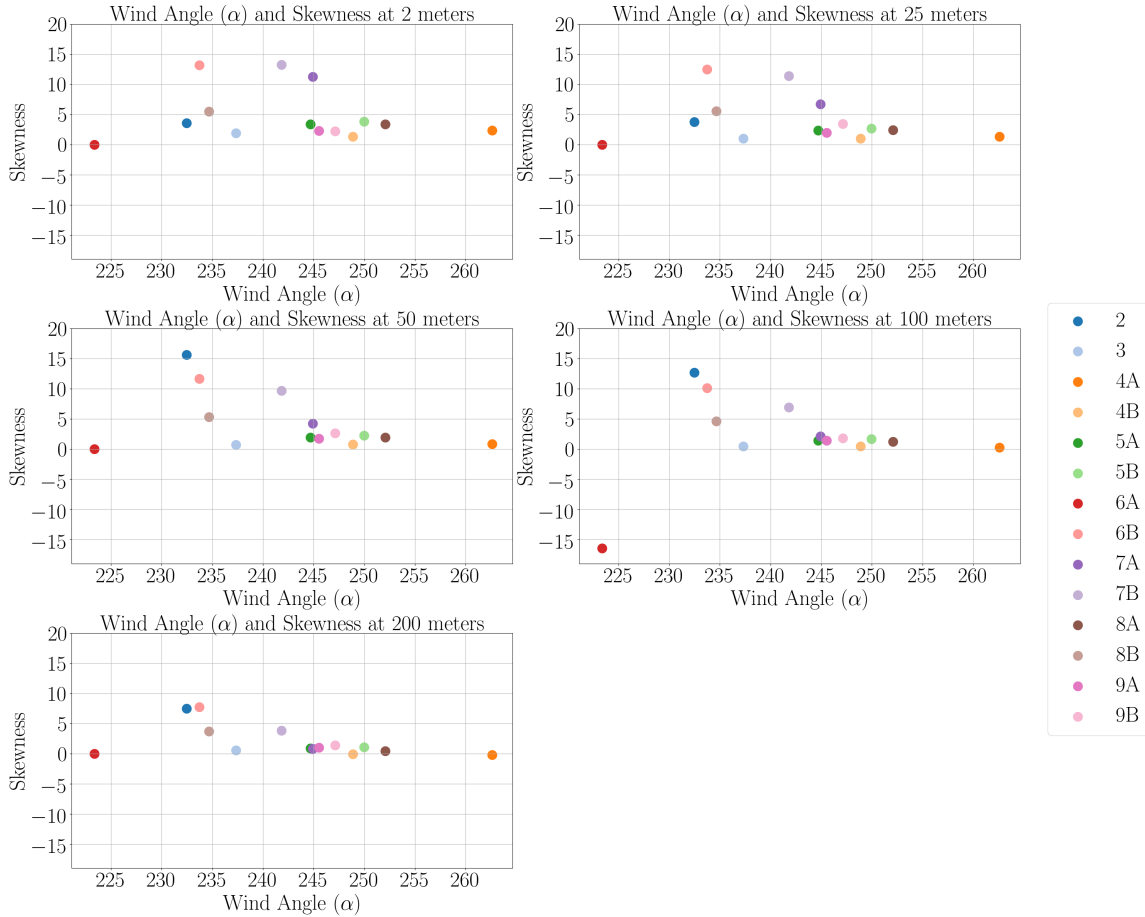
Figure 3.16: Mean wind angle compared to the skewness for each release at 2m, 25m, 50m, 100m, and 200m downwind of the source

wind angle than skewness, there still is not a noticeable relationship between the two (Figure 3.17).

The only other comparison that indicated a possible relationship was the dimensional stability parameter, $\frac{z}{L}$, and the second order moment, plume spread (Figure 3.18). Close to the source, there looks to be a slight increase in plume spread as - $\frac{z}{L}$ increases. As distance increases from the source, this relationship is more noticeable. While there seems to be a relationship between these two variables, an explanation for why this may be is unknown. For weakly unstable conditions, convective updrafts in the ABL have observed horizontal convective rolls (e.g. Atkinson and
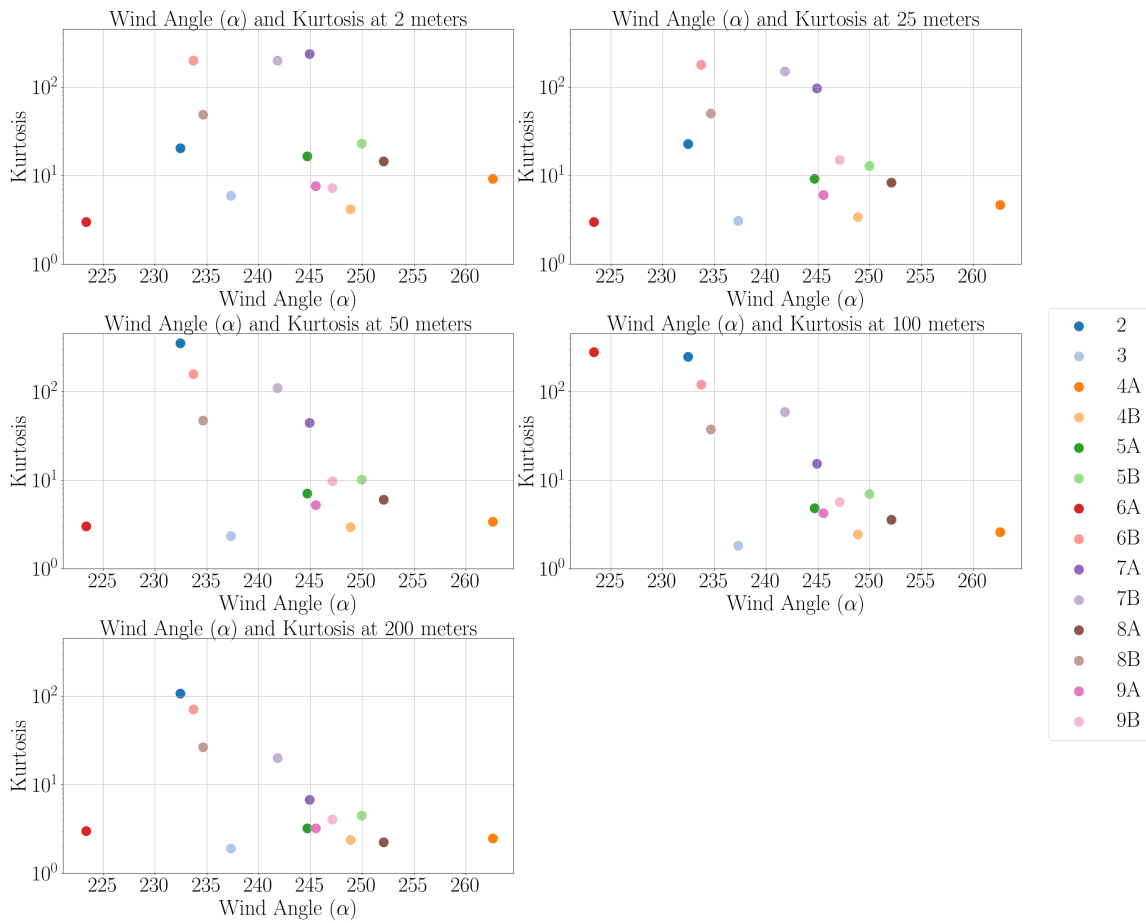
Figure 3.17: Mean wind angle compared to the kurtosis for each release at 2m, 25m, 50m, 100m, and 200m downwind of the source
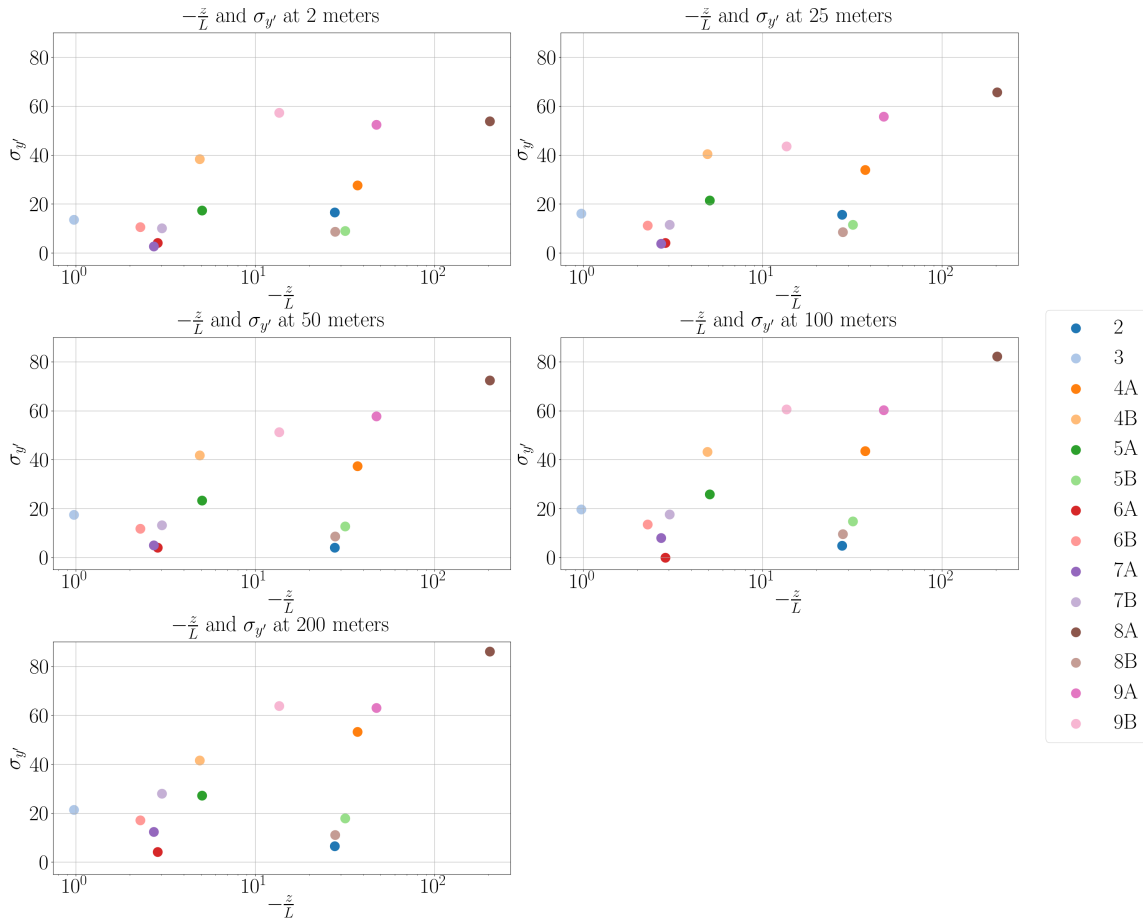
Figure 3.18: Dimensionless stability parameter, plotted as $-\frac{z}{L}$, compared to plume spread for each release at 2m, 25m, 50m, 100m, and 200m downwind of the source

Zhang, 1996; Young et al., 2002). As $-\frac{z}{L}$ increases, these rolls begin to organize into open convective cells (e.g. Agee et al., 1973; Atkinson and Zhang, 1996). There also has been observations of increased horizontal variance as the convective boundary layer becomes more convective (Panofsky et al., 1977), but the TRUC observations did show any correlation between the plume moments and σ_u^2.

From the other turbulence variables examined, these several relationships were the only ones that could possibly explain changes in the plume moments. Other turbulence variables examined did not indicate any relationship. While promising,

these relationships do not show a strong connection between plume characteristics and turbulence statistics.

3.4.2 Characterization of Urban Geometry

Another possible impact on plume behavior is the urban geometry. Giometto et al. (2017) examined the Sunset Tower and surrounding 1 km^2 using topographical LiDAR data and a LES. He broke down the tower domain into four subsets and calculated several building and vegetation statistics and studied their effect on momentum transport in the UCL. Along with calculating maximum and average building heights (h$_b$), Giometto et al. (2017) also calculated the plan area fraction (λ_p^b) and frontal area fractions from the south and west ($\lambda_{f,south}^b$ and $\lambda_{f,west}^b$, respectively). The plan area fraction is determined by the plan area of buildings at ground level (A_p) and total plan area of the region of interest (A_T): $\lambda_p^b = \frac{A_p}{A_T}$ (Burian et al., 2002). The frontal area fraction is determined by the total area of buildings projected into the plane normal to the approaching wind direction ($A_{proj.}$) and the total plan area of the region (A_T): $\lambda_{f,west}^b = \frac{A_{proj.}}{A_T}$ (Burian et al., 2002). The wind directions for west and south were assumed to be 270°and 180°. The plan area fraction of vegetation (λ_p^v) or tree canopy cover, was determined in a similar way to the plan area fraction of buildings: $\lambda_p^b = \frac{A_p^v}{A_T}$ (Giometto et al., 2017). The leaf area index (LAI) was determined indirectly by measuring the leaf area per m^2 through LiDAR returns. These variables are important to understand how dense the urban network is for both buildings and vegetation. If the urban network is more dense, the plume will interact with more obstacles, changing its initial behavior.

The building and vegetation statistics were reproduced for the specific release locations used during TRUC, using defined subsets from the same LiDAR data (Table 3.3). The subsets are shown in Figure 3.19, each colored for the four releases days: S1 is for June 19th, S2 is for June 22nd, S3 is for June 27th, and S4 is for June 29th.

	Unit	S1	S2	S3	S4
Buildings					
mean (h_b)	m	4.62	4.63	4.50	4.36
max (h_b)	m	10.27	9.90	10.63	9.62
h	m	6.78	6.80	6.63	6.43
λ_p^b	-	0.34	0.36	0.35	0.25
$\lambda_{f,west}^b$	-	0.186	0.202	0.213	0.118
$\lambda_{f,south}^b$	-	0.188	0.198	0.193	0.144
Vegetation					
mean (h_v)	m	3.95	4.00	3.60	3.55
max (h_v)	m	21.30	25.18	25.18	15.41
λ_p^v	-	0.102	0.105	0.141	0.106
LAI	-	0.266	0.268	0.367	0.307

Table 3.3: Building and vegetation statistics for urban canopy of subsets 1-4, modeled after Giometto et al. (2017) table. h_b and h_v are the height of the individual building or vegetation element. h = mean (h_b) + σ_{h_b}, where σ_{h_b} is the standard deviation of building height. λ_p^b and λ_p^v are the plan area fraction of buildings and vegetation, respectively. $\lambda_{f,west}^b$ and $\lambda_{f,south}^b$ denote the frontal area fraction of buildings with respect to the west and south approaching wind directions. LAI is the summer leaf area index of the canopy.
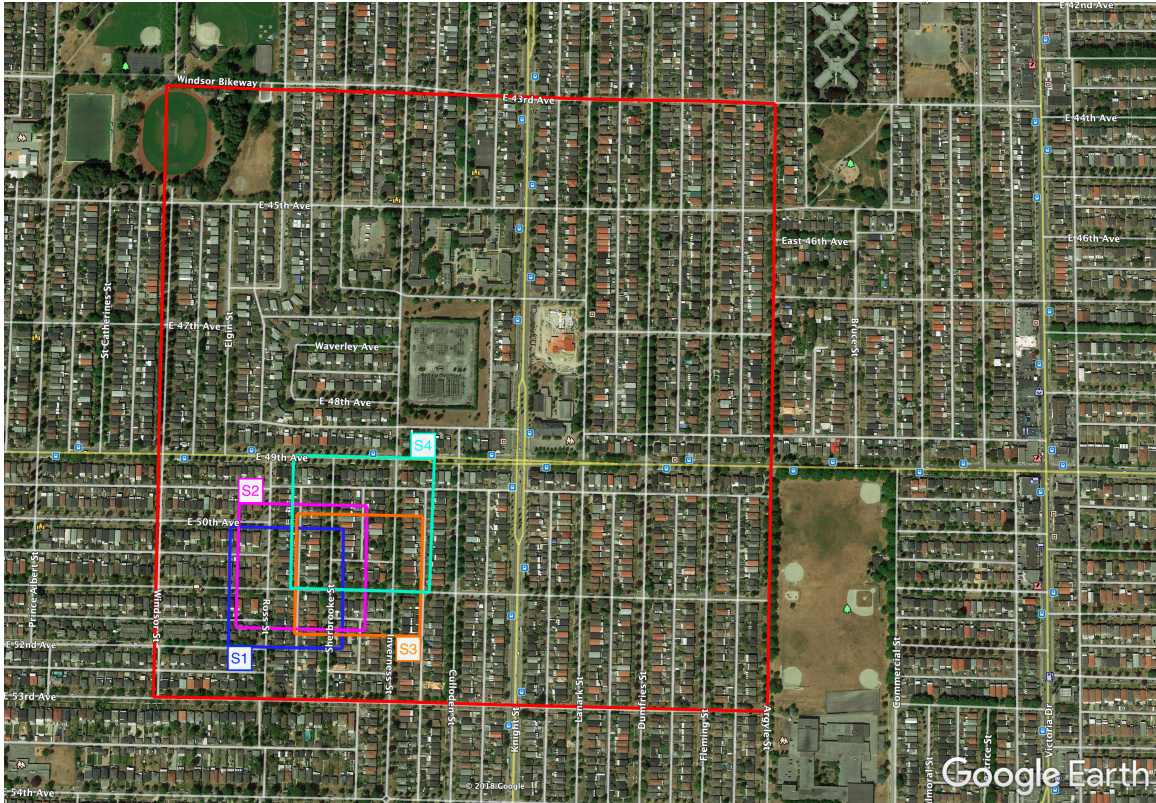
Figure 3.19: Subsets (S1, S2, S3, and S4) that were used to characterize each release day. The red outline is the 1 km^2 domain of the topographical LiDAR data. The image from Google Earth is meant to only represent the domains, not the LiDAR data itself.

From wind tunnel experiments (Hussain and Lee, 1980), there are three types of flow regimes within an idealized urban street canyon: isolated flow, wake interference flow, and skimming flow. The wake interference flow occurs when $0.1 < \lambda_p^b < 0.6$ (Oke, 1988), which is where the TRUC data values are. Voogt and Oke (1997) determined the plan area fraction for downtown Vancouver to be 0.37, which also falls into this regime. The four subsets are relatively similar to one another, except for subset 4. The frontal area fractions for subset 4 vary from the other three by about 20% - 30%, while the plan area fraction also varies by 30%.

The plumes from the four releases on June 29th mischaracterize the most of the TRUC observations. The different frontal area fraction and plan area fraction in subset 4 could possibly explain why plumes from June 29th do not capture more TRUC observations than the other release days. Other than subset 4, the similarities in the building and vegetation for the other three subsets provide little to no further information about possible impacts of these variables with plume behavior.

Chapter 4

Concluding Remarks

The atmospheric boundary layer is an ever-growing environment with complex interactions and developing issues that impact human life. As urban domains are predicted to increase in size and population, the effects of particulate matter and the urban heat island are expected to increase within the urban boundary layer. Recent experiments have been conducted to understand the impacts in downtown building districts, greater urban areas, and into the suburban environments. Releases of passive tracers have been used to replicate possible threats to human and plant life and examined at length. The importance of street-level and near-source observations are becoming a more pronounced problem in need of a solution.

4.1   Conclusions

The Tracer Release in an Urban Canopy (TRUC) provides a unique and necessary dataset to help address many of the remaining questions that this thesis hoped to address. The campaign observed a near-source release from fifty different impaction traps over four different configurations within a suburban neighborhood with 2-D and 3-D sonic anemometers. The location was well-observed by both previous experiments and numerical simulations.

From this particular field experiment, a new method (Miller et al., 2018) was used to interpolate the concentrations between the collection locations to calculate higher-order plume statistics. The Superposition of two Orthogonally-oriented Gaussian plume distributions (SOG) was utilized for all fourteen releases during TRUC and compared to verify its accuracy. While the SOG does well capturing the near-source concentrations, it does sometimes struggle with the far-field concentrations. SOG

does correctly predict the channeling through a suburban street network through the mean wind angle and various plume parameters. Some concentrations are not interpolated by SOG, due to it being Gaussian in nature (not considering upwind concentrations) or the plume shape incorrectly calculates a zero concentration close to the source.

Higher-order plume moments were calculated from the SOG concentrations produced. The mean plume centerline shows non-Gaussian features of large deviations from the mean wind direction, which may be due to the urban geometry. Spreading of the plume also seemed to be affected by the street network, as some plumes appeared to channel down streets through intersections. Gaussian values of skewness and kurtosis were observed (or values close to them) for several releases during TRUC. The non-Gaussian values close to the source agree with previous research that urban geometry can influence plume characteristics.

Turbulence statistics, as well as building and vegetation statistics, were examined to better understand the plume behavior in the urban canopy layer. While the wind angle did show promise of relationships between plume moments and the turbulence, there was not enough evidence to indicate a clear connection for any of the other variables. As the wind angle shifted from the cross-wind direction to the along-wind direction of the street network, the mean plume centerline and plume spread increased, meaning there was more spreading of the plume. Similarly, the building and vegetation statistics for the TRUC domain subsets did not show enough differences to determine possible explanations, except for subset 4. The urban geometry of the street network appeared to have the most influence on the plume behavior during TRUC.

4.2 Future Work

To obtain a complete understanding of particle dispersion in the urban canopy and its relationship with turbulence and urban geometry, more work is necessary. This analysis focused on one field campaign with limited near source observations. Near source urban experiments with a wider breadth and denser observational instrument network, including in the vertical direction, could result in more complete conclusions about the effects of urban areas on plume characteristics. Similarly, more frequent IOPs and longer overall temporal scale could be useful in determining plume behavior changes over time. Since the TRUC concentration observations were averaged over the twenty minute releases, observations of instantaneous concentrations would be especially beneficial for evaluating plume moments.

Regarding the SOG, the interpolant does include several parameters that are user-dependent and manually changed to better fit the two-dimensional (or three-dimensional) plume. This variability in the parameters could be creating an over-determined system, leading to issues in the interpolating process. The use of a third (or higher order) of Gaussian plume distributions could prove to fit better to the frequent non-Gaussian observed plume close to the source.

Comparison of the TRUC observations to large eddy simulations (LES) or obstacle resolving diagnostic dispersion models, specifically the QUIC-PLUME model (Williams and Brown, 2003), could be used to illustrate possible issues that SOG has with the urban domain. If an idealized domain is created for the TRUC dataset, then this could potentially lead to solutions to improve the interpolation process.

Finally, further analysis would be important for examining the urban geometry, with regards to the building and vegetation statistics. The frontal area fractions both assumed one wind direction for the TRUC domain, but each release had a unique mean wind direction for the twenty minute experiment period. If individual wind

directions could be analyzed, a better understanding of the building and vegetation impact on the plume could be evaluated.

Appendices

Appendix A

2D and 3D Sonics for Each Release

Releases	Sonics	$\overline{u}$	σ_u	$\langle\alpha\rangle$	σ_α
2	3D, O, P, Q	1.52	0.31	235.30	8.93
3	3D, O, P, Q	0.87	0.18	227.11	14.94
4A	3D, M, O, P, Q	1.47	0.30	249.20	17.74
4B	3D, M, O, P, Q	1.67	0.30	240.23	11.88
5A	3D, M, O, P, Q	1.46	0.31	234.97	22.46
5B	3D, M, O, P, Q	1.40	0.23	241.62	15.63
6A	3D, M, O, P, Q	1.32	0.23	204.82	10.88
6B	3D, M, O, P, Q	1.42	0.33	220.46	10.12
7A	3D, M, O, P, Q	1.29	0.34	235.31	13.12
7B	3D, M, O, P, Q	1.40	0.23	224.82	10.19
8A	3D, M, O, P, R	1.43	0.24	231.22	28.16
8B	3D, M, O, P, R	1.19	0.28	236.48	36.46
9A	3D, M, O, P, R	1.23	0.17	226.66	32.01
9B	3D, M, O, P, R	1.32	0.25	232.42	32.25

Table A.1: Mean wind speed and wind angles, as well as standard deviation for each respectively, for each release at 1.5 m. There were five 2D sonics, denoted by letters

Bibliography

Agee, E. M., T. S. Chen, and K. E. Dowell, 1973: A review of mesoscale cellular convection. *Bulletin of the American Meteorological Society*, **54 (10)**, 1004–1012, doi:10.1175/1520-0477(1973)054⟨1004:AROMCC⟩2.0.CO;2.

Allwine, K. J., and J. E. Flaherty, 2006a: Joint Urban 2003: Study overview and instrument locations. Tech. Rep. 15967, Pacific Northwest National Laboratory, United States. doi:10.2172/890732.

Allwine, K. J., and J. E. Flaherty, 2006b: Urban dispersion program MSG05 field study: Summary of tracer and meteorological measurements. Tech. Rep. 15969, Pacific Northwest National Laboratory, United States.

Allwine, K. J., J. H. Shinn, G. E. Streit, K. L. Clawson, and M. Brown, 2002: Overview of URBAN 2000. *Bulletin of the American Meteorological Society*, **83 (4)**, 521–536, doi:10.1175/1520-0477(2002)083⟨0521:OOUAMF⟩2.3.CO;2.

American Meteorological Society, 2012: Urban heat island. American Meteorological Society, URL http://glossary.ametsoc.org/wiki/Urban_heat_island.

Amthor, J. S., 1995: Terrestrial higher-plant response to increasing atmospheric co_2 in relation to the global carbon cycle. *Global Change Biology*, **1 (4)**, 243–274, doi:10.1111/j.1365-2486.1995.tb00025.x.

Anandakumar, K., 1999: A study on the partition of net radiation into heat fluxes on a dry asphalt surface. *Atmospheric Environment*, **33 (24)**, 3911 – 3918, doi:https://doi.org/10.1016/S1352-2310(99)00133-8.

Anderson, J. O., J. G. Thundiyil, and A. Stolbach, 2012: Clearing the air: a review of the effects of particulate matter air pollution on human health. *Journal of Medical Toxicology*, **8 (2)**, 166–175, doi:10.1007/s13181-011-0203-1.

Arya, S., 1999: *Air Pollution Meteorology and Dispersion*. Oxford University Press.

Atkinson, B. W., and J. W. Zhang, 1996: Mesoscale shallow convection in the atmosphere. *Reviews of Geophysics*, **34 (4)**, 403–431, doi:10.1029/96RG02623.

Baechlin, W., W. Theurer, and E. Plate, 1992: Dispersion of gases released near the ground in built up areas: Experimental results compared to simple numerical modelling. *Journal of Wind Engineering and Industrial Aerodynamics*, **44 (1)**, 2721 – 2732, doi:https://doi.org/10.1016/0167-6105(92)90066-J.

Baldocchi, D., and Coauthors, 2001: Fluxnet: A new tool to study the temporal and spatial variability of ecosystem-scale carbon dioxide, water vapor, and energy flux densities. *Bulletin of the American Meteorological Society*, **82 (11)**, 2415–2434, doi:10.1175/1520-0477(2001)082⟨2415:FANTTS⟩2.3.CO;2.

Belcher, S. E., O. Coceal, E. V. Goulart, A. C. Rudd, and A. G. Robins, 2015: Processes controlling atmospheric dispersion through city centres. *Journal of Fluid Mechanics*, **763**, doi:10.1017/jfm.2014.661.

Berkowicz, R., 2000: OSPM - a parameterised street pollution model. *Environmental Monitoring and Assessment*, **65**, 323–331, doi:10.1023/A:1006448321977.

Biltoft, C. A., 2001: Customer report for Mock Urban Setting Test. *DPG Document Number 8-CO-160-000-052. Prepared for the Defence Threat Reduction Agency.*

Bosanquet, C. H., and J. L. Pearson, 1936: The spread of smoke and gases from chimneys. *Trans. Faraday Soc.*, **32**, 1249–1263, doi:10.1039/TF9363201249.

Briggs, G. A., 1973: Diffusion estimation for small emissions, preliminary draft. Technical Report 79, Atmospheric Turbulence and Diffusion Laboratory.

Britter, R. E., and S. R. Hanna, 2003: Flow and dispersion in urban areas. *Annual Review of Fluid Mechanics*, **35 (1)**, 469–496, doi:10.1146/annurev.fluid.35.101101.161147.

Brook, R. D., and Coauthors, 2010: Particulate matter air pollution and cardiovascular disease. *Circulation*, **121 (21)**, 2331–2378, doi:10.1161/CIR.0b013e3181dbece1.

Brutsaert, W., 1982: *The Lower Atmosphere*, 37–56. Springer Netherlands, Dordrecht.

Burian, S., S. Velugubantla, and M. Brown, 2002: Morphological analyses using 3d building databases: Phoenix, arizona. Tech. Rep. LA-UR-02-6726, Los Alamos National Laboratory.

Carruthers, D., H. Edmunds, A. Lester, C. McHugh, and R. Singles, 2000: Use and validation of ADMS-urban in contrasting urban and industrial locations. *Int. J. of Environment and Pollution*, **14**, 364–374, doi:10.1504/IJEP.2000.000558.

Chakraborty, T., C. Sarangi, and S. N. Tripathi, 2017: Understanding diurnality and inter-seasonality of a sub-tropical urban heat island. *Boundary-Layer Meteorology*, **163 (2)**, 287–309, doi:10.1007/s10546-016-0223-0.

Changnon, S. A., F. A. Huff, and R. G. Semonin, 1971: METROMEX: an investigation of inadvertent weather modification. *Bulletin of the American Meteorological Society*, **52 (10)**, 958–968, doi:10.1175/1520-0477(1971)052⟨0958:MAIOIW⟩2.0.CO;2.

Chen, L., P. A. Dirmeyer, Z. Guo, and N. M. Schultz, 2018: Pairing FLUXNET sites to validate model representations of land-use/land-cover change. *Hydrology and Earth System Sciences*, **22 (1)**, 111–125, doi:10.5194/hess-22-111-2018.

Christen, A., N. C. Coops, R. Kellett, B. Crawford, E. Heyman, I. Olchovski, T. R. Tooke, and M. T. van der Laan, 2010: A lidar-based urban metabolism approach to neighbourhood scale energy and carbon emissions modelling. Tech. rep., Online, The University of British Colombia. doi:http://dx.doi.org/10.14288/1.0103595.

Christen, A., B. Crawford, K. Liss, and C. Siemens, 2013: Soil properties at the Vancouver EPiCC experimental sites. Tech. Rep. 2, The University of British Colombia. doi:http://dx.doi.org/10.14288/1.0103594.

Christen, A., and Coauthors, 2011: Validation of modeled carbon-dioxide emissions from an urban neighborhood with direct eddy-covariance measurements. *Atmospheric Environment*, **45 (33)**, 6057 – 6069, doi:https://doi.org/10.1016/j. atmosenv.2011.07.040.

Christen, A., and Coauthors, 2017: Urban climate research tower: Vancouver-sunset. The University of British Columbia.

City of Vancouver, 2019: Geography. City of Vancouver, URL https://vancouver.ca/ news-calendar/geo.aspx, Online.

Clawson, K., and Coauthors, 2004: Urban 2000 SF_6 atmospheric tracer field tests. Technical Memorandum ARL - 253, NOAA, Office of Oceanic and Atmospheric Research, Silver Spring, Maryland.

Clawson, K., and Coauthors, 2005: Joint Urban 2003 (JU03) SF_6 atmospheric tracer field tests. Technical Memorandum 254, NOAA, Office of Oceanic and Atmospheric Research, Silver Spring, Maryland.

Cramer, H., 1957: A practical method for estimating the dispersion of atmospheric contaminants. *Proc. 1st Natl. Conf. on Appl. Meteorol. Amer. Meteorol. Soc.*

Crawford, B., A. Christen, and R. Ketler, 2012: Processing and quality control procedures of turbulent flux measurements during the Vancouver EPiCC experiment. Tech. Rep. 1, The University of British Colombia. doi:http://dx.doi.org/10.14288/ 1.0103593.

Davidson, B., 1967: A summary of the new york urban air pollution dynamics research program. *Journal of the Air Pollution Control Association*, **17 (3)**, 154–158, doi: 10.1080/00022470.1967.10468961, pMID: 6038462.

Davidson, M., K. Mylne, C. Jones, J. Phillips, R. Perkins, J. Fung, and J. Hunt, 1995: Plume dispersion through large groups of obstacles—a field investigation. *Atmospheric Environment*, **29 (22)**, 3245 – 3256, doi:https://doi.org/10.1016/ 1352-2310(95)00254-V.

Davidson, M., W. Snyder, R. Lawson, and J. Hunt, 1996: Wind tunnel simulations of plume dispersion through groups of obstacles. *Atmospheric Environment*, **30 (22)**, 3715 – 3731, doi:https://doi.org/10.1016/1352-2310(96)00103-3.

DePaul, F., and C. Sheih, 1986: Measurements of wind velocities in a street canyon. *Atmospheric Environment (1967)*, **20 (3)**, 455 – 459, doi:https://doi.org/10.1016/0004-6981(86)90085-5.

Dirmeyer, P. A., C. A. Schlosser, and K. L. Brubaker, 2009: Precipitation, recycling, and land memory: An integrated analysis. *Journal of Hydrometeorology*, **10 (1)**, 278–288, doi:10.1175/2008JHM1016.1.

Dobre, A., S. Arnold, R. Smalley, J. Boddy, J. Barlow, A. Tomlin, and S. Belcher, 2005: Flow field measurements in the proximity of an urban intersection in london, uk. *Atmospheric Environment*, **39 (26)**, 4647 – 4657, doi:https://doi.org/10.1016/j.atmosenv.2005.04.015.

Doll, D., J. K. S. Ching, and J. Kaneshiro, 1985: Parameterization of subsurface heating for soil and concrete using net radiation data. *Boundary-Layer Meteorology*, **32 (4)**, 351–372, doi:10.1007/BF00122000.

Doran, J. C., and Coauthors, 1998: The IMADA-AVER boundary layer experiment in the Mexico City area. *Bulletin of the American Meteorological Society*, **79 (11)**, 2497–2508, doi:10.1175/1520-0477(1998)079⟨2497:TIABLE⟩2.0.CO;2.

Drivas, P. J., and F. H. Shair, 1974: Dispersion of an instantaneous cross-wind line source of tracer released from an urban highway. *Atmospheric Environment (1967)*, **8 (5)**, 475 – 485, doi:https://doi.org/10.1016/0004-6981(74)90062-6.

Environmental Protection Agency, 2018: Particulate matter. United States federal government, URL https://www.epa.gov/pm-pollution/particulate-matter-pm-basics#PM.

Findell, K. L., and E. A. B. Eltahir, 2003a: Atmospheric controls on soil moisture-boundary layer interactions: Three-dimensional wind effects. *Journal of Geophysical Research: Atmospheres*, **108 (D8)**, doi:10.1029/2001JD001515.

Finn, D., K. L. Clawson, R. G. Carter, J. D. Rich, C. Biltoft, and M. Leach, 2010: Analysis of urban atmosphere plume concentration fluctuations. *Boundary-Layer Meteorology*, **136 (3)**, 431–456, doi:10.1007/s10546-010-9510-3.

Franzese, P., and P. Huq, 2011: Urban dispersion modelling and experiments in the daytime and nighttime atmosphere. *Boundary-Layer Meteorology*, **139 (3)**, 395–409, doi:10.1007/s10546-011-9593-5.

Garratt, J., 1992: *The Atmospheric Boundary Layer*. Cambridge University Press, Cambridge, U.K.

Gifford, F., 1961: Use of routine meteorological observations for estimating atmospheric dispersion. *Nuclear Safety*, **2 (4)**, 47–51.

Giometto, M., A. Christen, P. Egli, M. Schmid, R. Tooke, N. Coops, and M. Parlange, 2017: Effects of trees on mean wind, turbulence and momentum exchange within and above a real urban environment. *Advances in Water Resources*, **106**, doi:10.1016/j.advwatres.2017.06.018.

Givoni, B., 1989: Urban design in different climates. Tech. Rep. 346, World Meteorological Organization, UCLA.

Goh, K. C., and C. H. Chang, 1999: The relationship between height to width ratios and the heat island intensity at 22:00 h for singapore. *International Journal of Climatology*, **19 (9)**, 1011–1023, doi:10.1002/(SICI)1097-0088(199907)19:9⟨1011::AID-JOC411⟩3.0.CO;2-U.

Goldreich, Y., 1992: Urban climate studies in Johannesburg, a sub-tropical city located on a ridge—a review. *Atmospheric Environment. Part B. Urban Atmosphere*, **26 (3)**, 407 – 420, doi:https://doi.org/10.1016/0957-1272(92)90016-L.

Goodwin, N. R., N. C. Coops, T. R. Tooke, A. Christen, and J. A. Voogt, 2009: Characterizing urban surface cover and structure with airborne lidar technology. *Canadian Journal of Remote Sensing*, **35 (3)**, 297–309, doi:10.5589/m09-015.

Grimmond, C. S. B., and T. R. Oke, 1991: An evapotranspiration-interception model for urban areas. *Water Resources Research*, **27 (7)**, 1739–1755, doi:10.1029/91WR00557.

Grimmond, C. S. B., and T. R. Oke, 2002: Turbulent heat fluxes in urban areas: Observations and a local-scale urban meteorological parameterization scheme (LUMPS). *Journal of Applied Meteorology*, **41**, 792–810, doi:10.1175/1520-0450(2002)041⟨0792:THFIUA⟩2.0.CO;2.

Gunawardena, N., E. R. Pardyjak, R. Stoll, and A. Khadka, 2018: Development and evaluation of an open-source, low-cost distributed sensor network for environmental monitoring applications. *Measurement Science and Technology*, **29 (2)**, 024 008, doi:10.1088/1361-6501/aa97fb.

Hanna, S., and E. Baja, 2009: A simple urban dispersion model tested with tracer data from Oklahoma City and Manhattan. *Atmospheric Environment*, **43 (4)**, 778 – 786, doi:https://doi.org/10.1016/j.atmosenv.2008.11.005.

Hanna, S., J. White, and Y. Zhou, 2007: Observed winds, turbulence, and dispersion in built-up downtown areas of Oklahoma City and Manhattan. *Boundary Layer Meteorology*, **125 (3)**, 441–468, doi:10.1007/s10546-007-9197-2.

Hansen, J. E., M. Sato, A. Lacis, R. Ruedy, I. Tegen, and E. Matthews, 1998: Climate forcings in the industrial era. *Proceedings of the National Academy of Sciences of the United States of America*, **95 (22)**, 12 753–12 758, doi:10.1073/pnas.95.22.12753.

Howard, L., 1833: *The Climate of London*, Vol. I - III. London.

Hoydysh, W. G., and W. F. Dabberdt, 1988: Kinematics and dispersion characteristics of flows in asymmetric street canyons. *Atmospheric Environment (1967)*, **22 (12)**, 2677 – 2689, doi:https://doi.org/10.1016/0004-6981(88)90436-2.

Hussain, and Lee, 1980: An investigation of wind forces on three dimensional roughness elements in a simulated atmospheric boundary layer flow. Report BS 56, Univ. Sheffield., Dept. Bldg. Sc.

Ichinose, T., K. Shimodozono, and K. Hanaki, 1999: Impact of anthropogenic heat on urban climate in tokyo. *Atmospheric Environment*, **33 (24)**, 3897 – 3909, doi: https://doi.org/10.1016/S1352-2310(99)00132-6.

Jacobs, C. M. J., and H. A. R. De Bruin, 1992: The sensitivity of regional transpiration to land-surface characteristics: Significance of feedback. *Journal of Climate*, **5 (7)**, 683–698, doi:10.1175/1520-0442(1992)005⟨0683:TSORTT⟩2.0.CO;2.

Järvi, L., C. Grimmond, and A. Christen, 2011: The surface urban energy and water balance scheme (SUEWS): Evaluation in Los Angeles and Vancouver. *Journal of Hydrology*, **411 (3)**, 219 – 237, doi:https://doi.org/10.1016/j.jhydrol.2011.10.001.

Jones, C., 1983: On the structure of instantaneous plumes in the atmosphere. *Journal of Hazardous Materials*, **7 (2)**, 87 – 112, doi:https://doi.org/10.1016/0304-3894(83) 80001-6.

Kastner-Klein, P., R. Berkowicz, and R. Britter, 2004: The influence of street architecture on flow and dispersion in street canyons. *Meteorology and Atmospheric Physics*, **87 (1)**, 121–131, doi:10.1007/s00703-003-0065-4.

Klein, P., and J. V. Clark, 2007: Flow variability in a North American downtown street canyon. *Journal of Applied Meteorology and Climatology*, **46 (6)**, 851–877, doi:10.1175/JAM2494.1.

Liss, K., T. R. Tooke, E. Heyman, N. C. Coops, and A. Christen, 2010: Vegetation characteristics at the Vancouver EPiCC experimental sites. Tech. Rep. 3, The University of British Colombia. doi:http://dx.doi.org/10.14288/1.0103589.

Ma, S., A. Pitman, M. Hart, J. P. Evans, N. Haghdadi, and I. MacGill, 2017: The impact of an urban canopy and anthropogenic heat fluxes on Sydney's climate. *International Journal of Climatology*, **37 (S1)**, 255–270, doi:10.1002/joc.5001.

MacDonald, R., R. Griffiths, and S. Cheah, 1997: Field experiments of dispersion through regular arrays of cubic structures. *Atmospheric Environment*, **31 (6)**, 783 – 795, doi:https://doi.org/10.1016/S1352-2310(96)00263-4.

MacDonald, R., R. Griffiths, and D. Hall, 1998: A comparison of results from scaled field and wind tunnel modelling of dispersion in arrays of obstacles. *Atmospheric Environment*, **32 (22)**, 3845 – 3862, doi:https://doi.org/10.1016/S1352-2310(98) 80006-X.

Martin, D., and Coauthors, 2010a: Urban tracer dispersion experiments during the second DAPPLE field campaign in London 2004. *Atmospheric Environment*, **44 (25)**, 3043 – 3052, doi:https://doi.org/10.1016/j.atmosenv.2010.05.007.

Martin, D., and Coauthors, 2010b: Urban tracer dispersion experiment in London (DAPPLE) 2003: field study and comparison with empirical prediction. *Atmospheric Science Letters*, **11 (4)**, 241–248, doi:10.1002/asl.282.

McElroy, J., and F. Pooler, 1968: The St. Louis Dispersion Study. *National Air Pollution Control Admin.*, **2 (No. AP-53)**, 50.

Menut, L., and Coauthors, 2000: Measurements and modelling of atmospheric pollution over the paris area: an overview of the ESQUIF project. *Annales Geophysicae*, **18 (11)**, 1467–1481, doi:10.1007/s00585-000-1467-y.

Miller, N. E., R. Stoll, W. F. Mahaffee, and T. M. Neill, 2018: Heavy particle transport in a trellised agricultural canopy during non-row-aligned winds. *Agricultural and Forest Meteorology*, **256-257**, 125–136, doi:https://doi.org/10.1016/j.agrformet.2018.02.032.

Miller, N. E., R. Stoll, W. F. Mahaffee, T. M. Neill, and E. R. Pardyjak, 2015: An experimental study of momentum and heavy particle transport in a trellised agricultural canopy. *Agricultural and Forest Meteorology*, **211-212**, 100 – 114, doi: https://doi.org/10.1016/j.agrformet.2015.06.003.

Mole, N., and C. D. Jones, 1994: Concentration fluctuation data from dispersion experiments carried out in stable and unstable conditions. *Boundary-Layer Meteorology*, **67 (1)**, 41–74, doi:10.1007/BF00705507.

Monin, A. S., 1970: The atmospheric boundary layer. *Annual Review of Fluid Mechanics*, **2 (1)**, 225–250, doi:10.1146/annurev.fl.02.010170.001301.

Nunez, M., and T. R. Oke, 1977: The energy balance of an urban canyon. *Journal of Applied Meteorology*, **16 (1)**, 11–19, doi:10.1175/1520-0450(1977)016⟨0011:TEBOAU⟩2.0.CO;2.

Obukhov, A. M., 1946: 'turbulentnost' v temperaturnoj – neodnorodnoj atmosfere (Turbulence in an atmosphere with a non-uniform temperature)'. *Trudy Inst. Theor. Geofiz.*, 95–115.

Oke, T. R., 1974: Review of urban climatology, 1968-1973. WMO No. 383 134, World Meteorological Organization, Geneva, Switzerland.

Oke, T. R., 1976: The distinction between canopy and boundary-layer urban heat islands. *Atmosphere*, **14 (4)**, 268–277, doi:10.1080/00046973.1976.9648422.

Oke, T. R., 1979a: Advectively-assisted evapotranspiration from irrigated urban vegetation. *Boundary-Layer Meteorology*, **17 (2)**, 167–173, doi:10.1007/BF00117976.

Oke, T. R., 1979b: Review of urban climatology, 1973-1976. WMO No. 510 169, World Meteorological Organization, Geneva, Switzerland.

Oke, T. R., 1982: The energetic basis of the urban heat island. *Quarterly Journal of the Royal Meteorological Society*, **108 (455)**, 1–24, doi:10.1002/qj.49710845502.

Oke, T. R., 1988: Street design and urban canopy layer climate. *Energy and Buildings*, **11 (1)**, 103 – 113, doi:https://doi.org/10.1016/0378-7788(88)90026-6.

Oke, T. R., and J. H. McCaughey, 1983: Suburban-rural energy balance comparisons for Vancouver, B.C.: An extreme case? *Boundary-Layer Meteorology*, **26 (4)**, 337–354, doi:10.1007/BF00119532.

Panofsky, H. A., H. Tennekes, D. H. Lenschow, and J. C. Wyngaard, 1977: The characteristics of turbulent velocity components in the surface layer under convective conditions. *Boundary-Layer Meteorology*, **11 (3)**, 355–361, doi:10.1007/BF02186086.

Pardyjak, E., and M. Brown, 200: Evaluatino of a fast-response urban wind model - comparison to single-building wind-tunnel data. Technical Report LA-UR-01-4028, Los Alamos National Laboratory.

Pasquill, F., 1961: The estimation of the dispersion of windborne material. *Meteorological Management*, **90 (1)**, 33–49.

Peng, S., and Coauthors, 2011: Surface urban heat island across 419 global big cities. *Environmental Science & Technology*, **46 (2)**, 696–703, doi:10.1021/es2030438.

Philips, D., R. Rossi, and G. Iaccarino, 2013: Large-eddy simulation of passive scalar dispersion in an urban-like canopy. *Journal of Fluid Mechanics*, **723**, 404–428, doi:10.1017/jfm.2013.135.

Pigeon, G., D. Legain, P. Durand, and V. Masson, 2007: Anthropogenic heat release in an old European agglomeration (Toulouse, France). *International Journal of Climatology*, **27 (14)**, 1969–1981, doi:10.1002/joc.1530.

Prandtl, L., 1904: Über flüssigkeitsbewegung bei sehr kleiner reibung. *Verhandlungen des dritten internationalen Mathematiker-Kongresses in Heidelberg 1904*, A. Krazer, Ed.

Rabin, R. M., S. Stadler, P. J. Wetzel, D. J. Stensrud, and M. Gregory, 1990: Observed effects of landscape variability on convective clouds. *Bulletin of the American Meteorological Society*, **71 (3)**, 272–280, doi:10.1175/1520-0477(1990)071⟨0272:OEOLVO⟩2.0.CO;2.

Rotach, M., S.-E. Gryning, and C. Tassone, 1996: A two-dimensional lagrangian stochastic dispersion model for daytime conditions. *Q.J.R. Meteorol. Soc.*, **122**, 367–389.

Rotach, M., and Coauthors, 2005: BUBBLE - an urban boundary layer meteorology project. *Theor. Appl. Climatol.*, **81**, 231–261, doi:https://doi.org/10.1007/s00704-004-0117-9.

Rotach, M. W., S.-E. Gryning, E. Batchvarova, A. Christen, and R. Vogt, 2004: Pollutant dispersion close to an urban surface – the BUBBLE tracer experiment. *Meteorology and Atmospheric Physics*, **87 (1)**, 39–56, doi:10.1007/s00703-003-0060-9.

Runnalls, K. E., and T. R. Oke, 2000: Dynamics and controls of the near-surface heat island of Vancouver, British Columbia. *Physical Geography*, **21 (4)**, 283–304, doi:10.1080/02723646.2000.10642711.

Santanello, J. A., C. D. Peters-Lidard, S. V. Kumar, C. Alonge, and W.-K. Tao, 2009: A modeling and observational framework for diagnosing local land–atmosphere coupling on diurnal time scales. *Journal of Hydrometeorology*, **10 (3)**, 577–599, doi:10.1175/2009JHM1066.1.

Schiermeir, F., 1978: Air monitoring milestones, RAP's field measurements are in. *Environmental Science & Technology*, **12 (6)**, 644–651, doi:10.1021/es60142a608.

Seinfeld, J. H., and S. N. Pandis, 2006: *Atmospheric Chemistry and Physics: From Air Pollution to Climate Change.* 2nd ed., John Wiley and Sons, Inc.

Socolofsky, S. A., and G. H. Jirka, 2004: Environmental fluid mechanics I, doi:https://ceprofs.civil.tamu.edu/ssocolofsky/OCENx89/Downloads/Book/Ch2.pdf, textbook-style manuscript.

Steemers, K., N. Baker, D. Crowther, J. Dubiel, and M. Nikolopoulou, 1998: Radiation absorption and urban texture. *Building Research & Information*, **26**, 103–112, doi:10.1080/096132198370029.

Steinecke, K., 1999: Urban climatological studies in the Reykjavík subarctic environment, Iceland. *Atmospheric Environment*, **33 (24)**, 4157 – 4162, doi:https://doi.org/10.1016/S1352-2310(99)00158-2.

Stockie, J., 2011: The mathematics of atmospheric dispersion modeling. *SIAM Review*, **53 (2)**, 349–372, doi:10.1137/10080991X.

Stull, R. B., 1988: *An introduction to boundary layer meteorology.* Atmospheric sciences library, Kluwer Academic Publishers, Dordrecht ; Boston.

Stull, R. B., 2006: The atmospheric boundary layer. *Atmospheric Science, An Introductory Survey*, Elsevier Inc.

Sutton, O. G., 1947a: The problem of diffusion in the lower atmosphere. *Quarterly Journal of the Royal Meteorological Society*, **73 (317-318)**, 257–281, doi:10.1002/qj.49707331704.

Sutton, O. G., 1947b: The theoretical distribution of airborne pollution from factory chimneys. *Quarterly Journal of the Royal Meteorological Society*, **73 (317-318)**, 426–436, doi:10.1002/qj.49707331715.

Sutton, O. G., and G. C. Simpson, 1932: A theory of eddy diffusion in the atmosphere. *Proceedings of the Royal Society of London. Series A, Containing Papers of a Mathematical and Physical Character*, **135 (826)**, 143–165, doi:10.1098/rspa.1932.0025.

Tennekes, H., 1973: The logarithmic wind profile. *Journal of the Atmospheric Sciences*, **30 (2)**, 234–238, doi:10.1175/1520-0469(1973)030⟨0234:TLWP⟩2.0.CO;2.

Tereshchenko, I., and A. Filonov, 2001: Air temperature fluctuations in Guadalajara, Mexico, from 1926 to 1994 in relation to urban growth. *International Journal of Climatology*, **21 (4)**, 483–494, doi:10.1002/joc.602.

Theurer, W., 1995: *Wind Climate in Cities*, chap. Point Sources in Urban Areas: Modelling of Neutral Gas Clouds with Semi-empirical Models, 485–502. Kluwer Academic Publishers, doi:10.1007/978-94-017-3686-2_22.

Thiessen, L. D., J. A. Keune, T. M. Neill, W. W. Turechek, G. G. Grove, and W. F. Mahaffee, 2016: Development of a grower-conducted inoculum detection assay for management of grape powdery mildew. *Plant Pathology*, **65 (2)**, 238–249, doi:10.1111/ppa.12421.

Tso, C., 1996: A survey of urban heat island studies in two tropical cities. *Atmospheric Environment*, **30 (3)**, 507 – 519, doi:https://doi.org/10.1016/1352-2310(95)00083-6, conference on the Urban Thermal Environment Studies in Tohwa.

Turner, D., 1969: Workbook of atmospheric dispersion estimates. Public Health Service Publication 999-AP-26, U.S. Environmental Protection Agency.

UNDESA, 2018: 2018 revision of world urbanization prospects. Tech. rep., Population Division of the United Nations Department of Economic and Social Affairs (UN DESA).

van der Laan, M., R. Tooke, A. Christen, N. Coops, E. Heyman, and I. Olchovski, 2012: Statistics on the built infrastructure at the Vancouver EPiCC experimental sites. Tech. Rep. 4, The University of British Colombia.

Velazquez-Lozada, A., J. E. Gonzalez, and A. Winter, 2006: Urban heat island effect analysis for San Juan, Puerto Rico. *Atmospheric Environment*, **40 (9)**, 1731 – 1741, doi:https://doi.org/10.1016/j.atmosenv.2005.09.074.

Voogt, J. A., and T. R. Oke, 1997: Complete urban surface temperatures. *Journal of Applied Meteorology*, **36 (9)**, 1117–1132, doi:10.1175/1520-0450(1997)036⟨1117:CUST⟩2.0.CO;2.

Williams, M. D., and M. J. Brown, 2003: Description of the QWIC-PLUME model. Technical Report LA-UR-03-1426, Los Alamos National Laboratory.

Wood, C. R., and Coauthors, 2009: Dispersion experiments in central london: The 2007 DAPPLE project. *Bulletin of the American Meteorological Society*, **90 (7)**, 955–970, doi:10.1175/2009BAMS2638.1.

World Health Organization, 2016: Ambient air pollution: A global assessment of exposure and burden of disease. Tech. rep., World Health Organization.

Yee, E., and C. A. Biltoft, 2004: Concentration fluctuation measurements in a plume dispersing through a regular array of obstacles. *Boundary-Layer Meteorology*, **111 (3)**, 363–415, doi:10.1023/B:BOUN.0000016496.83909.ee.

Yee, E., P. R. Kosteniuk, G. M. Chandler, C. A. Biltoft, and J. F. Bowers, 1993: Statistical characteristics of concentration fluctuations in dispersing plumes in the atmospheric surface layer. *Boundary-Layer Meteorology*, **65 (1)**, 69–109, doi:10.1007/BF00708819.

Young, G., D. Kristovich, M. Hjelmfelt, and R. Foster, 2002: Rolls, streets, waves, and more: a review of quasi-two-dimensional structures in the atmospheric boundary layer. *Bulletin of the American Meteorological Society*, **83 (7)**, 997–1001.

Zhao, L., X. Lee, R. B. Smith, and K. Oleson, 2014: Strong contributions of local background climate to urban heat islands. *Nature*, **511**, 216–219, doi:10.1038/nature13462.